Modeling of wall shear stress in large arteries

Document Version:
Publisher's PDF, also known as Version of Record (includes final page, issue and volume numbers)

Please check the document version of this publication:

• A submitted manuscript is the version of the article upon submission and before peer-review. There can be important differences between the submitted version and the official published version of record. People interested in the research are advised to contact the author for the final version of the publication, or visit the DOI to the publisher's website.
• The final author version and the galley proof are versions of the publication after peer review.
• The final published version features the final layout of the paper including the volume, issue and page numbers.

Link to publication

MODELING OF
WALL SHEAR STRESS
IN LARGE ARTERIES

FRANK GIJSEN

Modeling of wall shear stress in large arteries

Modeling of wall shear stress in large arteries

Dit proefschrift is goedgekeurd door de promotoren:

prof.dr.ir. J.D. Janssen
prof.dr. R.S. Reneman

en de copromotor:

dr.ir. F.N. van de Vosse

... and they all pretend they're orphans,
and their memory is like a train
you can see it getting smaller as it pulls away
and the things you can't remember
tell the things you can't forget that
history puts a saint in every dream

Tom Waits

Ter nagedachtenis aan mijn ouders

Contents

x   *Contents*

Summary

Disturbance of wall shear stress distribution in large arteries is believed to be one the key factors in the development of atherosclerosis and the failure of vascular grafts. Modeling of the blood flow induced wall shear stress in large and medium sized arteries therefore qualifies as an important research area and is the main topic of this thesis.

In modeling wall shear stress, the choice of an appropriate constitutive equation for blood is crucial. Determination of an appropriate constitutive model for blood is not trivial: it is a concentrated suspension of blood cells in plasma and exhibits a range of non-Newtonian properties. These properties are mainly governed by the deformation and aggregation of red blood cells. Apart from the fluid properties, flow conditions in large arteries are an important factor in determining an appropriate constitutive equation for blood. In the literature on blood flow in large arteries, blood is generally modeled as a Newtonian fluid with the high shear rate limit viscosity of blood ($\eta = \eta_\infty$).

In the first part of this thesis, a macroscopic constitutive equation for blood is proposed. A concentrated KSCN solution with 250 ppm Xanthan gum served as a macroscopic blood analog fluid. The viscometric properties of this fluid are almost identical to the viscometric properties of blood. The Xanthan gum solution was modeled by the inelastic shear-thinning Carreau-Yasuda model. Laser Doppler anemometry and FEM analyses were applied to obtain detailed quantitative information on the velocity distribution in a model of the carotid bifurcation under steady flow conditions and in a 90° degree curved tube under unsteady flow conditions. The results for the non-Newtonian Xanthan gum solution were compared to a Newtonian fluid model with a viscosity equal to the high shear viscosity of the blood analog fluid.

The experimental results showed significant differences between the velocity distribution of the Newtonian and non-Newtonian fluid, implying that the non-Newtonian properties of the blood analog fluid cannot be ignored. The non-Newtonian flow in the two models was predicted quite well by the numerical simulations, using the inelastic fluid model. This indicates that shear thinning is the dominant non-Newtonian property of the blood analog fluid and that viscoelasticity can be ignored for the prediction of the velocity distribution.

The shear thinning properties of the non-Newtonian fluid can be approximated by a Newtonian fluid with a viscosity evaluated at a characteristic shear rate of the flow. The characteristic shear was based on an average shear rate, rather than on wall shear

rate. The results of the Newtonian flow field, using a *characteristic* viscosity, compared well to the non-Newtonian flow field. The value of *Re* for the non-Newtonian fluid was based on the characteristic viscosity and is about three times lower than *Re* for the Newtonian fluid with $\eta = \eta_\infty$.

The ability of this macroscopic model to predict flow of a red blood cell suspension is verified by analyses of velocity profiles downstream a backward-facing step under steady flow conditions. The velocity distribution was measured by means of ultrasound velocimetry. The comparison between numerical and experimental results indicates that flow of the red blood cell suspension can be described using the inelastic Carreau-Yasuda model. Both viscoelasticity and particulate nature of the red blood cell suspension do not significantly influence the flow features under steady flow conditions. The velocity measurements were used to validate a clinical procedure to determine wall shear rates *in-vivo*. The clinical procedure gives a good approximation in the central part of the channel, but procedure underestimates wall shear rates by approximately 25% in fully developed flow.

Whether the Carreau-Yasuda model can also be used to predict wall shear stresses accurately, requires a new experimental technique. A method to determine wall shear stress was developed for flow in a rectangular duct, and evaluated for a Newtonian and a non-Newtonian fluid. Wall shear stress was inferred from the deformation of an elastic gel layer inside the flow model. The deformation of the gel layer was measured accurately by means of speckle pattern interferometry and through the properties of the gel layer, wall shear stress was computed. The measured wall shear stress showed good agreement with the computed wall shear stress for both the Newtonian and the non-Newtonian fluid. With the proposed method, wall shear stress can be determined without prior knowledge of the properties of the fluid.

The method to determine wall shear stress distribution was applied downstream a backward-facing step, using a red blood cell suspension as a measuring fluid. The wall shear stress distribution was determined under steady flow conditions. The good agreement between experimental and numerical wall shear stress distribution is indicative for the inelastic behavior of the red blood cell suspension. Furthermore, the particulate nature of the red blood cell suspension does not seem to influence flow behavior and wall shear stress distribution.

On the basis of the results presented in this thesis, it can be concluded that velocity and wall shear stress distributions in large arteries can be modeled with an inelastic Carreau-Yasuda model, thus providing valuable information for studies on the development of atherosclerosis and failure of vascular grafts.

Chapter 1

General introduction

Atherosclerosis is a disease that may cause progressive occlusion of the lumen of arteries. It is one of the main causes of death in the western society. The development of this disease, atherogenesis, is therefore an important research topic. In the advanced stage of atherosclerosis, the occluded part of the artery is often by-passed or replaced by a vascular prosthesis. These prostheses often fail due to hyperplasia, causing an occlusion of the artery at the anastomoses. There are strong indications that development of atherosclerosis and failure of vascular prostheses can be correlated to local hemodynamics, and a key role is attributed to wall shear stress (section 1.1). Although the exact mechanisms of the above mentioned pathological processes are not yet known, it is well established that the endothelial mono-layer, separating blood from the vessel wall, forms a highly active and wall shear stress sensitive interface. The response of the endothelial cells to blood flow is discussed in section 1.2. To link atherogenesis to response of the endothelium to the loading conditions in the arterial system, modeling of blood flow in large arteries is important and it involves a range of topics, including hemorheology, hemodynamics and determination of wall shear stress. The study of these topics form the main objective of this thesis (section 1.3). An outline of the thesis is given in section 1.4.

1.1 Blood flow, atherogenesis and hyperplasia

1.1.1 Blood flow and atherogenesis

From clinical practice it is known that particular sites in the arterial tree are specifically sensitive to atherogenesis. Local hemodynamics apparently play an important role in the development of this disease (for a review, see Nerem, 1993).
Normal arteries consist of three distinct layers: the intima, the media and the adventitia. The intima consists of connective tissue and is covered by endothelium. The endothelium is a mono-layer of cells and forms the interface between blood and the vessel wall. The media, the middle layer, consist mainly of smooth muscle cells, while the outer layer, the adventitia, is composed of smooth muscle cells, collagen

and fibroblasts. Three types of atherosclerotic lesions can be recognized: the fatty streak, the fibrous plaque and the complex lesions (Ross and Glomset, 1976; Glagov *et al.*, 1995). The fatty streak consist of localized smooth muscle cells, surrounded by deposits of lipids. The fibrous plaque, commonly associated with atherosclerosis, consists of lipid-laden smooth muscle cells in the intima, and the lesions protrude into the artery. The fibrous plaque covers a deeper accumulation of free lipids and cell debris. The development of the fibrous plaque is often preceded by proliferation of smooth muscle cells in the intima. Once the fibrous plaque calcificates and is altered by thrombosis, the complex lesion is formed. Local hemodynamics can be linked to atherogenesis: low and alternating positive and negative (oscillating) blood flow induced wall shear stresses and enhanced diffusion of molecules through the endothelium correlate with the sites, prone to the development of atherosclerotic lesions.

The wall shear stress in the arterial system has a pulsatile nature but remains unidirectional in the larger part of the arteries. Except for the lesion-prone sites: the wall shear stresses are predominantly low and can have alternating positive and negative values. At these sites, rounded cells can be found, while the endothelial cell in less lesion-prone regions is elongated and orientated in the direction of the wall shear stress. Nerem (1992) argues that the endothelial cells are influenced by the local hemodynamics. The properties of endothelial cells in regions with low or oscillating wall shear stress might be changed in a way that favors the process of atherogenesis. The correlation between low or oscillating wall shear stresses and atherogenesis is confirmed by other studies (Friedman *et al.*, 1981; Nerem, 1993).

It has been shown that in large arteries, the transport of various molecules from the blood to the sub-endothelium is restricted, except for the sites prone to the development of atherosclerotic lesions (Nerem, 1992). Enhanced permeability of the endothelium to low density lipoproteins (LDL), and subsequent modification of LDL by the endothelial cells, might be important for the development of fatty streaks. The presence of NO determines the oxidative environment of the endothelium, an important factor in the development of atherosclerosis. The amount of NO, released by the endothelium, is influenced by wall shear stress, and the near wall blood velocity determines the convection of NO. From these observations, particle residence time could be regarded as a key factor in atherogenesis. Caro *et al.* (1971) developed a theory based on shear rate depended mass transfer mechanisms for small particles (e.g. cholesterol) suspended in the blood. The local shear rate governs the concentration distribution of these particles and thus the diffusion of these particles to the vessel wall. Combined with a model for biochemical interaction of the particles in the wall, they were able to link regions with low wall shear rates to the preferred sites for atherogenesis.

In order to further study the process of atherogenesis, modeling of blood flow induced mechanical load of the endothelial cells and the near-wall rheology of blood in large and medium sized arteries is of great interest.

1.1.2   Hyperplasia in vascular grafts

The failure of smaller vascular grafts is due to the development of hemodynamically significant stenoses at the anastomotic sites (Ku and Allen, 1995). The development of stenoses starts with a process called neointimal hyperplasia. In the initial stage of neointimal hyperplasia, the anastomosis is covered with a cloth, containing platelets, fibrin and red blood cells. Subsequently, the cloth is covered with endothelial cells, and the cloth is replaced. At a final stage, intimal hyperplasia might occur. This process is characterized by sub-endothelial cell proliferation of random structure, and it might lead to significant stenoses. The later stage is believed to be related to wall shear stress. A compliance mismatch between prosthetic graft and vessel wall induces shear stress gradients, followed by a response of the endothelial cells. Experiments on the development of intimal hyperplasia in tapered vascular grafts in dogs have confirmed this hypothesis: in the grafts, the intimal thickening did correlate with low shear stresses (Salam *et al.*, 1996). In the study of Hofstra (1995), intimal thickening at the proximal anastomotic sites correlated with high shear rates.

The importance of blood flow modeling is evident: in combination with an appropriate model for the vessel, the wall shear stress and shear rates in a new arterial graft could be predicted and the mechanical properties and geometry of the graft could be optimized to obtain a smooth wall shear stress transition at anastomotic sites.

1.2   Blood flow and the endothelium

The local nature of atherogenesis and failure of vascular prostheses may be correlated to wall shear stress distribution and particle residence time of various molecules. These observations are mere correlations and do not explain the origin of the diseases. A key-role in the development of atherosclerosis is attributed to the endothelium. It is involved in various processes: regulation of the diameter of the artery, prevention of coagulation of blood and control of the vascular permeability. The endothelium is subjected to mechanical loads: blood flow induced pressure and wall shear stress and strains from the deforming vessel wall (figure 1.2). Zhao *et al.* (1995) showed that the endothelium responds strongly to both cyclic variation of strains of the vessel wall *and* to flow induced wall shear stress. This study focuses on latter of the two loading conditions of the endothelium: pressure induced strain distribution in large arteries is described by Rutten (1998).

Endothelial cells are highly responsive to flow induced wall shear stress. The mechanical loads are converted to biochemical messengers, and these messengers change the mechanical and functional properties of the endothelial cells. Since the loading conditions in the arterial system vary, the properties of the endothelium have a local character (Sato and Oshima, 1994). The locally altered properties of the endothelium can be associated with the pathological processes, described previously.

The endothelial cells show a myriad of responses when subjected to mechanical load *in-vitro* (Davies and Tripathi, 1993; Davies, 1995; Nerem, 1993). The properties of a cell can be altered at cellular, molecular and genetic level, and at various time scales. The fastest response can be seen at a molecular level: alteration of ionic conduc-
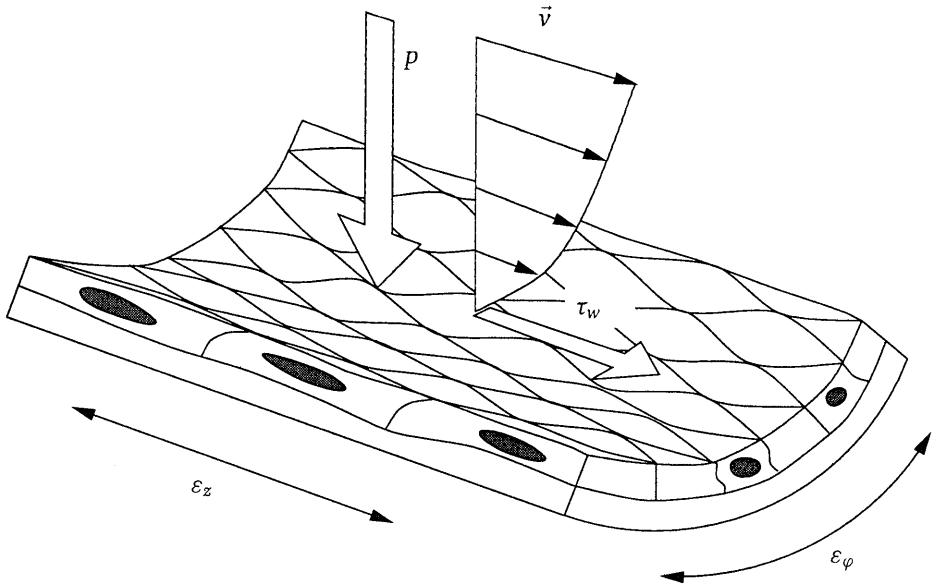
Figure 1.1: *The mechanical loads on the endothelium.*

tance of the membrane, activity of the membrane enzyme adenylate cyclase, inositol triphosphate generation and an altered intercellular Ca^{2+} concentration occur within seconds. At a longer time scale, the gene expression changes. Eventually, under sustained load, the endothelial cells exhibit structural changes, and the cytoskeleton reorganizes, leading to orientation of the endothelial cells.

1.3   Aim of the study

From the above cited literature on cultured endothelium, it is clear that the loading conditions of the endothelium play a key role in the various pathological processes. The extent to which wall shear stress and near-wall blood rheology are responsible for the pathological processes, described in section 1.1, requires more insight into blood flow induced wall shear stress and wall shear rate distribution. The blood flow induced wall shear stress and wall shear rate depend on the properties of blood, the geometry of the arteries, and on the flow conditions. The aim of this study is to obtain an experimentally validated model to predict blood flow induced wall shear stress and wall shear rate in large arteries. The influence of deformability of the vessel wall on wall shear rate and wall shear stress is not included in this study.
The blood flow induced wall shear stress and wall shear rate can be obtained through the solution of the equations of motion. To solve these equations, a constitutive model for blood is required. Since this study focuses on the blood flow in large arteries, a continuum model for blood will be used. The parameters in these models can

be determined by measuring the properties of blood in viscometric flow. Using a macroscopic continuum model for blood, velocities distribution and wall shear stress can be studied in physiologically relevant flows. Validation of this macroscopic model for blood is required to investigate whether or not the particulate nature of blood can be ignored. Part of this study deals with a new method to measure blood flow induced wall shear stress *in-vitro*. The developed method can be used to validate the model's ability to predict blood flow induced wall shear stress.

The result of this study will be an evaluation of an appropriate model for the constitutive behavior of blood, and its application in relevant geometries under physiological flow conditions. The constitutive model for blood can then be used to predict wall shear stress *in-vivo* and in optimization of vascular graft design.

1.4   Scope of the thesis

Blood exhibits a range of non-linear responses to mechanical loading. The concentration of the constituents of blood and their morphology take account for this complex behavior. The choice of an appropriate constitutive model, required to solve the equations of motion, is therefore not a trivial matter. The motivation to adopt a macroscopic constitutive model for blood is based on the assumption that concentration distribution of red blood cells in large arteries is homogeneous. The properties of blood and a discussion of the concentration distribution of red blood cells in large arteries form the first part of chapter 2. A review of the available macroscopic models for blood, combined with the flow conditions in the arterial system, lead to a choice of a constitutive model for blood. This constitutive model is applied to study velocity fields in physiologically relevant geometries, both experimentally and numerically (chapter 3 and 4). The influence of the macroscopic non-Newtonian behavior of blood on flow phenomena under physiological flow conditions is investigated. The results of this study indicate that the non-linear properties of the macroscopic fluid model, even under the assumption that the particulate nature of blood can be neglected, have a significant effect on the velocity field. Ultrasound velocimetry is applied to assess the ability of the macroscopic model to predict velocity distributions in a red blood cell suspension in backward-facing step flow (chapter 5). Whether the macroscopic model for blood can also be applied to predict wall shear stress is studied in the second part of this thesis. To investigate this topic, a new method is developed to measure the wall shear stress (chapter 6). This method is applied in backward-facing step flow, using a red blood cell suspension as a measuring fluid. The ability of the macroscopic model for blood to predict wall shear stress is assessed in chapter 7. The thesis is concluded with a general discussion (chapter 8).

Chapter 2

Blood and blood flow

The properties of blood depend mainly on the concentration and properties of the red blood cells (section 2.1). Since it has a major impact on the choice of the constitutive model for blood, the homogeneity of the red blood cells in large arteries is discussed in section 2.2. From this discussion, it is hypothesized that the red blood cell concentration in large arteries is homogeneous, and that blood flow in large arteries can be modeled with a macroscopic constitutive equation for blood. A selection of macroscopic constitutive models is discussed in section 2.3. The choice of an appropriate macroscopic constitutive model depends on the flow conditions in and the geometry of the arteries. Through a discussion on dimensionless parameters in blood flow in large arteries, an indication of the influence of various properties of blood can be obtained (section 2.4). The section on the constitutive equations, combined with the discussion on the scaling aspects in blood flow, gives a guideline for the modeling of the blood flow in large arteries (section 2.5).

2.1 Morphology and viscometric properties

Blood is a concentrated suspension of blood cells in plasma. The white blood cells, or leucocytes, are roughly spherical in shape with a diameter between 7 and 9 μm. The platelets are much smaller than the leucocytes; they are oval shaped with a diameter ranging from 1 to 3 μm. Together, the leucocytes and the platelets occupy less than one percent of the volume of blood. The red blood cells, or red blood cells, are biconcave discs and occupy 45 % of the blood volume. They dominate the rheological behavior of blood. Further discussion of the blood cells will therefore be confined to the red blood cells.

2.1.1 Morphology and properties of plasma and red blood cells

This review on the composition and properties of the constituents of blood is limited to plasma, being the suspending phase, and red blood cells. The information for

this section is taken from Merrill (1969), Cokelet (1972) and Caro *et al.* (1978) and Alberts *et al.* (1994).

Plasma

Plasma is an aqueous saline solution containing proteins and inorganic molecules. The outline of the composition of the plasma is given in table 2.1. The density of plasma is 1030 $kg.m^{-3}$. If denaturation of the plasma proteins is avoided, plasma behaves like a Newtonian fluid with a dynamic viscosity of $\eta = 1.2$ $mPa.s$. The inor-

material	concentration $g.100\ ml^{-1}$	molecular weight $*10^{-3}$	dimension nm
water	90-92		
proteins			
albumin	3.3-4.0	69	15x4
globulins	1.88-1.97	44-1300	
fibrinogen	0.34-0.43	400	50-60x3-8
inorganic constituents			
cations			
sodium	0.31-0.34		
other (Na^+, Ca^{2+}, Mg^{2+})	0.027-0.035		
anions			
chloride	0.36-0.39		
other	0.20-0.24		

Table 2.1: *Composition of plasma [from Caro* et al. *(1978)]*

ganic constituents of the plasma are a governing factor in various transport processes and generate an osmotic pressure of about $8 \cdot 10^5$ Pa (equivalent to a 0.9% sodium chlorine solution by weight).
The proteins have various functions and can be divided into three groups:

- fibrinogen: a large, asymmetric molecule that is intimately involved in the co-agulation of blood. Although the concentration of fibrinogen is low, it attributes significantly to the elevated viscosity of plasma due to its asymmetry.

- albumin: a small molecule that is important for the osmotic pressure, induced by the proteins.

- globulins: relatively symmetric molecules that are involved in transport of lipids and antibody reactions.

Apart from the buffering function of all the proteins, both fibrinogen and the globulins are involved in the aggregation of red blood cells.

Red blood cells

Red blood cells form the dominant particulate matter of blood. The volume concentration of the red blood cells, called hematocrite (Ht), is about 45 %. The density of the red blood cells is 1080 $kg.m^{-3}$. The red blood cell is a biconcave discoid and the main dimensions are given in figure 2.1. The origin of the biconcave shape of the red blood cell is a subject of dispute. For a review of possible explanations, one is referred to Fung (1993). An important consequence of the biconcave shape is the ability of the red blood cell to change shape without changing the surface area. The
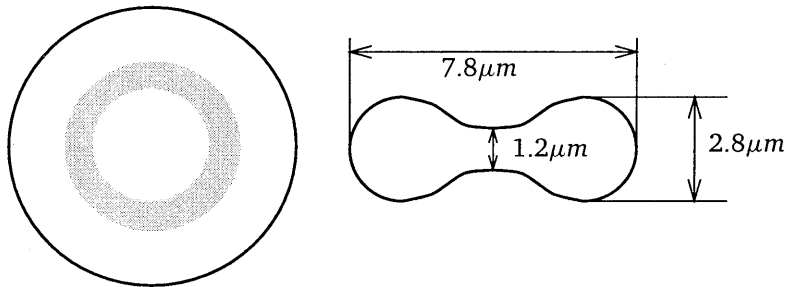
Figure 2.1: *Size and dimension of the red blood cell*

membrane of the red blood cell has a thickness of 80 *nm* and consists of a phospholipid bilayer. This bilayer is covered with albumin on the outside and with another protein layer, spectrin, on the inside. The spectrin layer is a skeletal protein and supports the lipid bilayer. The liquid interior of the red blood cell is a saturated solution of haemoglobin (32 % by weight), behaving as a Newtonian fluid with a dynamic viscosity of $\eta = 6$ *mPa.s* (Cokelet and Meiselman, 1968).

The haemoglobin ($MW = 68.000$) is a protein complex, consisting of a Fe^{2+} complex, the haem group, surrounded by amino-acid molecules. The haem group is essential for transport processes for it can bind oxygen and carbon-dioxide and it gives blood its red color.

The biconcave shape, combined with the low bending stiffness of the membrane and the liquid interior, enhance the ability of the red blood cell to deform readily. This enables red blood cell to pass through capillaries with a diameter smaller than 8 μm. Another phenomenon, closely linked to the deformability of the red blood cell, is the rotation of the membrane around the liquid interior in a shear flow (tank-threading movement, Schmid-Schönbein *et al.* (1971)).

Red blood cells aggregate face to face if they are brought in contact with each other at low shear rates (see figure 2.2). These aggregates are known as rouleaux and are formed under the influence of bridging macromolecules, especially fibrinogen. At near zero shear rates, secondary aggregation of the rouleaux occurs, leading to formation of a rouleaux network.

2.1.2   Viscometric properties of blood

The properties of blood are governed by the concentration and the properties of the red blood cells. The discussion on the properties of blood in this section is limited to physiological values of Ht, but it should be noted that the properties of blood are dependent on the concentration of red blood cells. The deformability, orientation and aggregation of the red blood cells induce the specific behavior of blood in simple shear flow, the prevailing flow condition at near-wall sites in the vascular tree. Shear flow can be generated in a viscometer and is often used to characterize fluids. A uniform velocity field is generated and by measuring the flow induced torque, the viscometric properties of a fluid can be determined.

shear thinning   At low shear rates ($\dot{\gamma} < 10\ s^{-1}$), the red blood cells tend to aggregate and form rouleaux. Under no flow conditions, the time scale for the formation of rouleaux is 60 s. At a shear rate of $\dot{\gamma} = 10\ s^{-1}$, the collision frequency of the red blood cells increases and the time scale for rouleaux formation decreases to 10 s (McMillan *et al.*, 1987). These rouleaux increase the viscosity of the blood. If shear rate is decreased even further ($\dot{\gamma} < 1\ s^{-1}$), the rouleaux form three dimensional structures, inducing an additional increase of the viscosity. The time required for building a network is even longer than for rouleaux formation. If shear rate is increased, the rouleaux break up and the red blood cells align with flow. Eventually, shear rates are high enough to deform red blood cells, thus decreasing viscosity. Deformability, orientation and aggregation of red blood cells result in shear thinning behavior of blood (figure 2.2).

viscoelasticity   The deformability and orientation of rouleaux and individual red blood cells lead to the viscoelastic behavior of blood. They provide means of storing energy during flow. Thurston (1973) investigated viscoelastic properties of blood in the linear viscoelastic regime and measured a significant elastic component in oscillatory blood flow (figure 2.3). He also measured the shear rate dependence of the viscoelastic properties of blood at a given frequency (Thurston, 1979). From these measurements, the non-linear viscoelastic properties of blood are evident.

thixotropy   Thixotropy is a property of structured fluids, subjected to a transient load. Alteration of the mechanical load changes the structure of the fluid (e.g. break down of rouleaux, orientation of red blood cells), and some time is required before a new equilibrium is established. McMillan *et al.* (1987) investigated the transient properties of blood in viscometric flow. They measured shear stress generated by blood, subjected to a number of sequential steps in shear rate (figure 2.4). The overshoot in shear stress was attributed to orientation of red blood cells. The delayed relaxation of shear stress can be related to the viscoelastic properties of blood and a rapid loss of orientation of the red blood cells. The same authors could not detect any measurable first normal stress differences in blood.
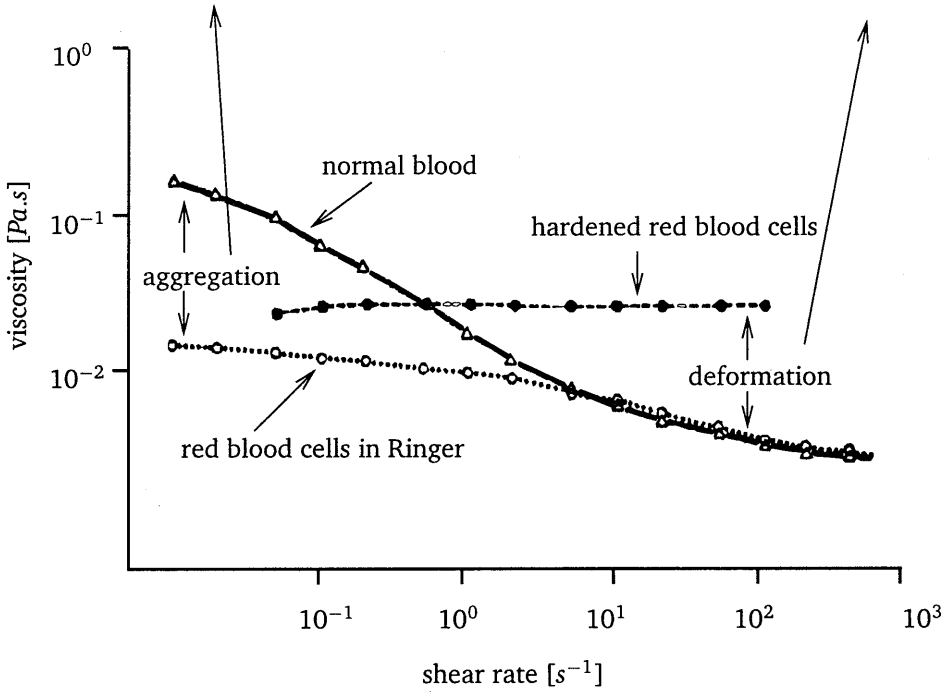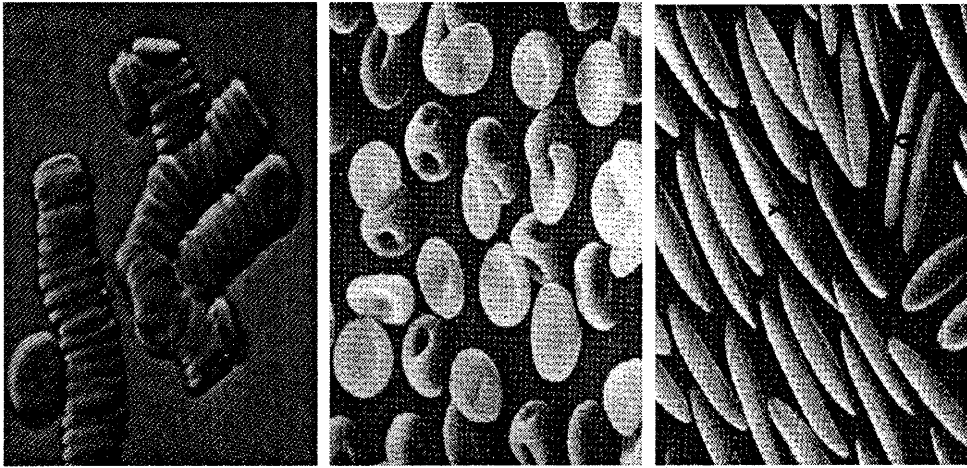
Figure 2.2: *Viscosity in steady shear of normal blood, blood with hardened red blood cells (no deformation) and blood in a Ringer solution (no aggregation) [from Chien et al. (1970) and Caro et al. (1978)]*
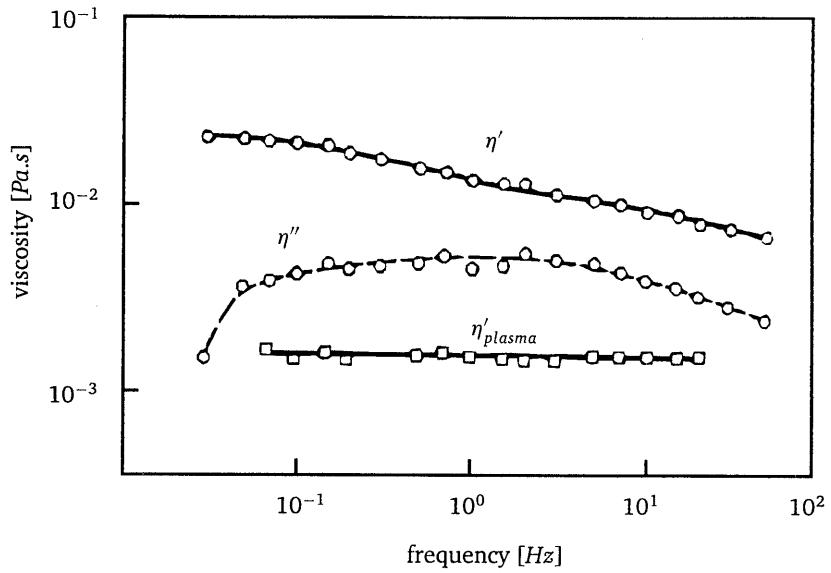
Figure 2.3: *The elastic (η'') and the viscous (η') component of the complex viscosity of blood as a function of frequency in oscillatory shear [from Thurston (1973)]*
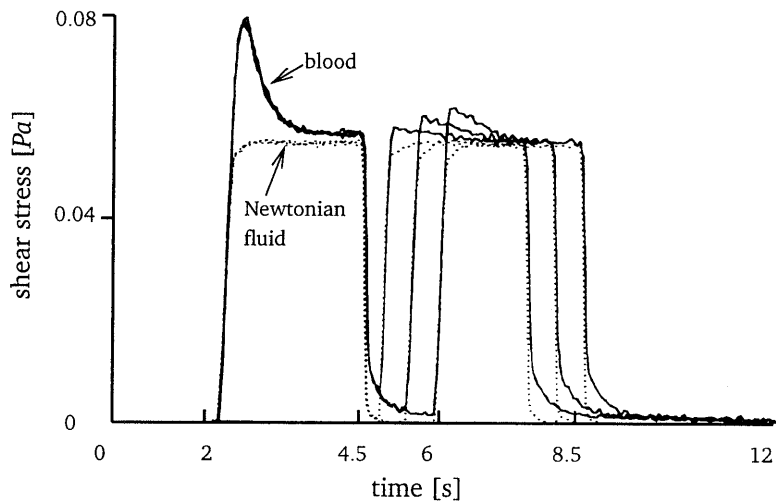
Figure 2.4: *Transient behavior of blood: measured shear stress after repeated steps in shear rate [from McMillan et al. (1987)]*

Cokelet (1972) presented an extended review on the problems arising in determining the properties of blood through viscometry. The measured torque at low shear rates is a function of time, indicating migration of red blood cells and subsequent formation of a plasma rich layer near the wall. Reduction of the measured torque to shear stress and rotational speed of the viscometer to shear rate is not valid due to inhomogeneity of the fluid. Karnis *et al.* (1966) measured velocity and concentration distributions in concentrated suspensions in a Couette device. They showed that the concentration distribution was not uniform and the velocity gradient was not constant. From these studies, it can be concluded that determination of the viscometric properties of blood is complicated and that results from the literature should be interpreted with caution.

2.2   Concentration distribution of red blood cells

The concentration distribution of red blood cells in large arteries is an important factor in the choice of an constitutive model for blood. If homogeneity of the concentration distribution of red blood cells can be assumed, a macroscopic continuum model can be used to describe blood flow in large arteries. Several mechanisms are responsible for migration of *isolated* particles across streamlines. Fluid inertia and the presence of the wall induce lateral displacements of particles in tube flow (for a review, see Goldsmith, 1993). In a concentrated suspension like blood, particle-particle interactions and the crowding effect are dominant over the mechanisms of migration of isolated particles (Goldsmith and Marlow, 1979). Two mechanisms can be responsible for an inhomogeneous concentration distribution in a concentrated suspension: the wall exclusion effect and shear induced migration.

2.2.1   Wall exclusion effect

The wall exclusion effect states that particles with radius a cannot be closer to the wall than a. The consequence of this effect is that the particle concentration close to the wall is lower than the bulk concentration of the fluid. A cell-depleted or cell-free region with a lower viscosity is formed at the wall, serving as a lubricating layer.
The effect of the cell-depleted layer on blood flow was studied extensively for capillary flow. For tubes with a radius (a) smaller than 100 μm, the inhomogeneous concentration distribution of the red blood cells leads the the well-known Fåhræus-Linquist effect (Fårhæus and Lindquist, 1931); the pressure drop along a tube decreases with decreasing diameter of the tube. This effect can be attributed for by modeling blood as a two-phase fluid: a core region with high erythrocyte concentration and a cell-depleted layer with the plasma viscosity (e.g. Uijttewaal, 1993). The velocity distribution in capillaries was studied by e.g Bugliarello and Sevilla (1970). Using a comparable two-phase model for blood flow, they were able to obtain a good agreement between experimental and analytical velocity distributions in 40 and 70 μm tubes. The study of Goldsmith and Marlow (1979) showed that the cell-depleted layer for concentrated red blood cell suspensions was approximately 4 μm. For small capillaries ($a = 50$ μm), this cell-depleted layer attributed to a blunted axial velocity

profile with a core region of particles with constant axial velocity. The size of the core region decreased with increasing diameter of the tube. The lower concentration of the red blood cells at near wall sites is also associated with an increased platelet concentration *in-vivo* (Tangelder *et al.*, 1986).

Detailed information about the cell-depleted layer in *large* arteries is relatively scarce. Phibbs (1968) studied the thickness of the cell-depleted peripheral layer. By quick-freezing a femoral artery of a rabbit, they were able to investigate the concentration distribution of the red blood cells. They found a decreased red blood cell concentration in a peripheral layer with a thickness of about one particle diameter, which is too small to significantly influence blood flow in large arteries.

2.2.2   Shear induced migration

Shear induced migration in a suspension is caused by the hydrodynamic interactions of the particles. The migration process can be modeled by a convection diffusion equation. Philips *et al.* (1992) proposed a transport equation that accounts for shear induced migration of rigid particles in a concentrated suspension. The particle fluxes can be attributed to two effects: spatially varying interaction frequency and spatially varying viscosity. Due to spatially varying interaction frequency, particles will move from high shear rate to low shear rate regions and from regions with high particle concentration to regions with low particle concentration. The spatially varying viscosity will cause doublets of particles to move towards regions with lower viscosity. The transport equation predicts shear-induced migration in a tube flow depending on particle radius b, tube length L and the ratio of particle-tube radius $H = b/a$. In fully developed flow, the model predicts an inhomogeneous concentration distribution with higher particle concentrations in the central part of the tube. Experiments by Koh *et al.* (1994) showed that the the model for shear induced migration can be used to predict concentration and velocity distribution in concentrated suspensions of rigid spheres in tube flow. They found a blunted axial velocity profile and a concentration distribution with a marked peak in the center of the tube.

Phan-Thien and Fang (1996), based on the work of Nott and Brady (1994), determined the entrance length L_{ss} to reach steady state for shear induced migration in tube flow:

$$L_{ss} = 0.5 \frac{a^3}{b^2} \tag{2.1}$$

In table 2.2, equation (2.1) is applied to blood flow in the human circulation. The estimated inlet length for the concentration distribution in large arteries in human circulation are too long to reach steady state due to the size of the red blood cells. For smaller tubes ($H = 0.1$), shear induced migration can give rise to an inhomogeneous concentration distribution and a flattened velocity profile. It has to be remarked that Koh *et al.* (1994) concluded from their experiments that inlet lengths for shear induced migration might be considerably shorter than predicted by Nott and Brady (1994). The mechanisms for shear induced migration are valid for rigid spheres: the theory was not applied to asymmetric, deformable particles yet.

Vessel	a [m]	H [−]	L_{ss} [m]
Aorta	$1.2 \cdot 10^{-2}$	$3 \cdot 10^{-4}$	$5 \cdot 10^{4}$
Carotid	$4 \cdot 10^{-3}$	$1 \cdot 10^{-3}$	$2 \cdot 10^{3}$
Arteriole	$4 \cdot 10^{-5}$	$1 \cdot 10^{-1}$	$2 \cdot 10^{-3}$

Table 2.2: *Estimation of inlet length for concentration distribution in the human circulation, using the results of Phan-Thien and Fang (1996).*

From the above observations, it can be assumed that the cell-depleted layer and shear induced migration do not significantly influence blood flow in large arteries. The red blood cell concentration can be regarded as homogeneous. From that it follows that flow large arteries can be modeled with a macroscopic constitutive equation for blood.

2.3   Constitutive models

Determination of the blood flow induced wall shear stress and wall shear rate requires the solution of the Navier-Stokes equations. In a general form, these equations read:

$$
\begin{cases}
\rho \dot{\mathbf{v}} + \rho (\mathbf{v} \cdot \nabla)\mathbf{v} - \nabla \cdot \sigma = \mathbf{f} \\[2mm]
\nabla \cdot \mathbf{v} = 0
\end{cases}
\tag{2.2}
$$

where $\mathbf{v}$ is the velocity vector, σ the Cauchy stress tensor, $\mathbf{f}$ the body force per unit mass, ∇ the gradient operator, and $\dot{\mathbf{v}}$ is the time derivative $\frac{\partial \mathbf{v}}{\partial t}$. A constitutive equation is required to couple the Cauchy stress to the rate of deformation and/or the deformation of the fluid. For a Newtonian fluid with a constant dynamic viscosity η, the Cauchy stress tensor can be written as:

$$
\sigma = -p\mathbf{I} + 2\eta \mathbf{D} \tag{2.3}
$$

$$
\mathbf{D} = \frac{1}{2}[\nabla \mathbf{v} + (\nabla \mathbf{v})^{T}] \tag{2.4}
$$

where p is the hydrostatic pressure, and $\mathbf{D}$ the rate of deformation tensor. The constitutive equation for blood should preferably incorporate the non-linear and time dependent properties, discussed in section 2.1.2. In this section, a review will be given on the constitutive models that can be used to characterize blood. Constitutive equations can be subdivided into generalized Newtonian (section 2.3.1) and viscoelastic (section 2.3.2) models.

2.3.1   Generalized Newtonian fluid models

The generalized Newtonian fluid models are time independent constitutive models. They can be used to model the viscous properties of blood. Viscoelasticity and thixotropy cannot be described with these models.

Newtonian model

Many fluids obey Newton's law, stating that stress in the fluid is proportional to rate of deformation. In simple shear, Newton's law reduces to:

$$\tau = \eta|\dot{\gamma}| \tag{2.5}$$

where η is the dynamic viscosity of the fluid, and τ shear stress and $|\dot{\gamma}|$ the absolute value of the shear rate. The materials that follow Newton's law are gases and small molecule liquids like water and oil. In Newtonian fluids, there are no normal stress differences in steady shear, nor can shear thinning behavior be modeled.

Generalized Newtonian models

The Newtonian model can only predict the behavior of a limited class of fluids. A logical extension of the Newtonian model is a dependence of viscosity on shear rate. In this way, shear thinning can be modeled. For generalized Newtonian models, the Cauchy stress tensor depends on the second invariant of the rate of deformation tensor (II_D):

$$\sigma = -p\mathbf{I} + 2\eta(II_D)\mathbf{D} \tag{2.6}$$

In simple shear, II_D reduces to $\dot{\gamma}$. A range of shear rate dependent viscosity models is used to model shear thinning behavior of blood. The power-law model is a generalized Newtonian model that is widely used to model the behavior of blood. In simple shear, it states that:

$$\tau = m|\dot{\gamma}|^n \quad \text{or} \quad \eta = m|\dot{\gamma}|^{n-1} \tag{2.7}$$

The two parameters in this model, n and m, characterize the fluid behavior. The main advantage of this model is its simplicity: analytical solutions for simple flow problems are available. The power law model cannot predict the viscosity of the fluid at high ($\eta \rightarrow 0$) or at low shear rates ($\eta \rightarrow \infty$). Furthermore, the constants in the model cannot be associated with the physical properties of the fluid. The constitutive equation for a Casson model is given by:

$$\tau^{\frac{1}{2}} = \tau_y^{\frac{1}{2}} + (\eta_c|\dot{\gamma}|)^{\frac{1}{2}} \tag{2.8}$$

The Casson model is appropriate for shear thinning fluids with a yield stress (τ_y). The evidence for yield stresses in blood are circumstantial and there is no consensus about the yield stress value. Other models, like the Carreau-Yasuda model, predict the shear thinning behavior of blood more accurately:

$$\frac{\eta - \eta_\infty}{\eta_0 - \eta_\infty} = \left[1 + (\lambda_{cy}|\dot{\gamma}|)^a\right]^{\frac{n-1}{a}} \tag{2.9}$$

At high shear rates, the fluid behaves like a Newtonian fluid with a viscosity η_∞, describing the viscosity of blood with deformed and aligned red blood cells. At low shear rates, another Newtonian plateau can be observed with a viscosity of η_0. At the

intermediate shear rates, the fluid will exhibit non-Newtonian behavior. The transition from the low shear rate Newtonian plateau to the high shear rate limit is a fluid property. Based on the work of Krieger and Dougherty (1959), Quemada (1978) proposed a viscosity model combining concentration and shear rate dependence:

$$\eta = \eta(\phi, \dot{\gamma}) = \eta_s \left[1 - \frac{\phi}{2} \left(k_\infty + \frac{k_0 - k_\infty}{1 + \left(\frac{|\dot{\gamma}|}{\dot{\gamma}_c} \right)^q} \right) \right]^{-2} \tag{2.10}$$

where k_∞, k_0, q and $\dot{\gamma}_c$ are material parameters and ϕ the concentration of red blood cells.

2.3.2   Viscoelastic fluid models

Whenever materials exhibit a time dependent response to mechanical loading, they are categorized as viscoelastic materials. Subjected to small strains, the viscoelastic properties of the fluid are independent of strain. The properties in the small strain region can be modeled with linear viscoelastic constitutive equations. The linear viscoelastic properties of fluids are often used for characterization purposes. In all practical applications fluids are subjected to large strains and strain rates. Non-linear viscoelastic models have to be applied to model this behavior.

Linear viscoelastic models

The linear viscoelastic behavior of a fluid can be modeled with an equation proposed by Maxwell:

$$\tau + \lambda_k \frac{d\tau}{dt} = \eta_k 2\mathbf{D} \tag{2.11}$$

where λ is the relaxation time, and τ the deviatoric part of the Cauchy stress tensor. For $k = 1$, equation (2.11) reduces to a single mode Maxwell model. The single mode Maxwell model can be understood intuitively: at high deformation rates, the time derivative in equation (2.11) dominates and the fluid exhibits solid-like behavior, while at low deformation rates the time derivative disappears and a viscous response of the fluid is expected. For $k = 1...n$, a generalized Maxwell model is obtained. A generalized Maxwell model incorporates a series of relaxation times (λ_k) and viscosities (η_k) and can be used to model the linear viscoelastic properties of blood.
It has to be kept in mind that the Maxwell constitutive equation is only valid for small strains and therefore can only be used to model linear viscoelastic behavior of a fluid. It does not predict important non-linear effects: shear thinning, thixotropy and non-linear viscoelasticity are not modeled. The linear Maxwell model can be used to determine characteristic time constants for a fluid.

Non-linear viscoelastic models

The time dependent behavior of viscoelastic fluids subjected to large strains cannot be described with the generalized Maxwell model. In non-linear viscoelastic models, the

local time derivative in equation (2.11) is substituted by a convective time derivative. This substitution enables modeling of the constitutive properties of viscoelastic fluids subjected to large strains. In this section, the non-linear viscoelastic models will be discussed briefly.

The non-linear and time dependent properties of a fluid can be incorporated in the Maxwell model (2.11):

$$\tau + \lambda_k \overset{\triangledown}{\tau} = \eta_k 2\mathbf{D} \tag{2.12}$$

By substituting the local time derivative in equation (2.11) by the upper-convected time derivative, the upper-convected Maxwell (UCM) model is obtained. The upper-convected time derivative contains products of velocity gradient and stress:

$$\overset{\triangledown}{\tau} \equiv \frac{\partial \tau}{\partial t} + v \cdot \vec{\nabla} \tau - (\vec{\nabla}v)^T \cdot \tau - \tau \cdot \vec{\nabla}v \tag{2.13}$$

For small strains, the UCM model reduces to the linear Maxwell model and for steady flow *and* small strains, the UCM predicts Newtonian behavior.

The UCM model can be generalized by including several terms that enable a better fit of viscometric data:

$$\overset{\triangledown}{\tau} + \tau + \lambda_k \mathbf{f}_c(\tau, \mathbf{D}) + \lambda_k \mathbf{f}_d(\mathbf{D}) = \eta_k 2\mathbf{D} \tag{2.14}$$

The terms $\mathbf{f}_c$ and $\mathbf{f}_d$ are measures of the stress build-up and stress decay, respectively. Several forms for these additional terms have been introduced in literature, each having their specific advantages and drawbacks.

Williams *et al.* (1993) proposed a special form of the Maxwell model to relate the micro-structure of blood to its macroscopic properties. Both λ and η depend on a structure factor P. This structure factor is a measure of the number of rouleaux in blood. The kinetics of P are given by:

$$\frac{dP}{dt} = k(1 - P) - \alpha|\dot{\gamma}|P \tag{2.15}$$

where k and $\alpha|\dot{\gamma}|$ describe the mechanisms for the formation and the break up of the rouleaux structures. Equation (2.15) can be used to predict the viscometric properties of blood at low shear rates.

Quemada followed a similar approach in a series of studies (Quemada and Droz, 1983; Quemada, 1984, 1993). A non-linear Maxwell equation was adopted to model the viscometric behavior of blood. The viscous and elastic properties depended on a structure parameter λ. With this model, the transient data from McMillan *et al.* (1987) were predicted quite accurately (see also figure 2.4).

The parameters in the above mentioned non-linear viscoelastic models require more data than currently available for blood. No reliable information on normal stress differences or elongational viscosity of blood are available. For further reading on non-linear viscoelastic models and constitutive models in general, one is referred to Bird *et al.* (1987) and Macosko (1994).

2.4   Dimensionless parameters in blood flow

The constitutive equations that can be used to describe the properties of blood are discussed in the previous section. The choice of the appropriate constitutive equation does not only depend on the properties of blood but also on the flow conditions and the geometry of the arteries.

The dimensionless form of equation (2.2) for Newtonian fluids yields two important dimensionless parameters:

$$Sr \frac{\partial \mathbf{v}}{\partial t} + (\mathbf{v} \cdot \nabla)\mathbf{v} = -\nabla p + \frac{1}{Re} \nabla \cdot \tau \qquad (2.16)$$

$$Sr = \frac{L}{VT} \quad : \quad \text{Strouhal number} \qquad (2.17)$$

$$Re = \frac{\rho L V}{\eta} \quad : \quad \text{Reynolds number} \qquad (2.18)$$

In equations (2.17) and (2.18), L, V, T, ρ and η are measures for characteristic length, velocity, time, density and viscosity respectively. Sr gives the ratio of the instationary to the convective forces while Re gives the ratio of the convective to the viscous forces. The dimensionless parameters for non-Newtonian flow, consisting of a fluid parameter and a flow parameter, can be used to estimate the combined effect of fluid properties and flow conditions. After adopting a constitutive model, three dimensionless parameters can be formulated to estimate the influence of various aspects of the macroscopic non-Newtonian behavior of blood on blood flow in large arteries.

2.4.1   Can blood be modeled as a Newtonian fluid?

The steady shear properties of blood clearly indicate its shear thinning behavior. Two Newtonian plateaus are present: one at low shear rates (η_0), and one at high shear rates (η_∞). To model the shear thinning properties of blood, the Carreau-Yasuda model is adopted (equation 2.19). The dimensionless viscosity (η^*) can be written as:

$$\eta^* = \frac{\eta - \eta_\infty}{\eta_0 - \eta_\infty} = [1 + (\lambda_{cy}\dot{\gamma})^a]^{\frac{n-1}{a}} \qquad (2.19)$$

where η is viscosity, $\dot{\gamma}$ shear rate and $\eta_0, \eta_\infty, n, a$ and λ_{cy} are fluid parameters. The dimensionless viscosity depends on the shear rate, and a definition of a characteristic shear rate can be used to estimate the importance of the shear thinning properties of blood for the flow in large arteries. For that purpose, a shear rate number ($N_{\dot{\gamma}}$) is defined:

$$N_{\dot{\gamma}} = \lambda_{st} \dot{\gamma}_c \qquad (2.20)$$

where λ_{st} is a characteristic time constant of the fluid and $\dot{\gamma}_c$ a characteristic shear rate of the flow. For high values of the shear rate number $N_{\dot{\gamma}}$, the fluid will behave

as a Newtonian fluid with $\eta = \eta_\infty$, while at low values of $N_{\dot\gamma}$ a Newtonian model with $\eta = \eta_0$ can be used. At intermediate values, the shear thinning behavior must be taken into account. For λ_{st}, the time constant in the Carreau-Yasuda model (λ_{cy}) can be used, and its value follows from viscometric data ($\lambda_{cy} \approx 0.1\ s$, see chapter 4). An estimation of the characteristic shear rate for blood flow in large arteries can be derived from Newtonian flow in a straight tube. From the momentum equation for steady, axisymmetric flow in a straight tube, the velocity distribution can be obtained. The velocity distribution is used to determine shear rate:

$$\dot\gamma = \frac{4V}{a^2} r \tag{2.21}$$

where r is the radial coordinates, a is the radius of the tube and V the mean velocity. A characteristic shear rate in this flow could be defined as:

$$\dot\gamma_c = \frac{2V}{a} \tag{2.22}$$

The characteristic shear rate in large arteries can be defined in various ways: some authors use wall shear rate (which is in fact often the highest shear rate occurring in blood flow), while others use a shear rate based on an average value (table 2.4.1). The definition of the characteristic shear rate (equation 2.22) resembles the defini-

study	definition of $\dot\gamma_c$
Baaijens *et al.* (1993)	$\frac{\pi V}{a}$
Ballyk *et al.* (1994)	$\frac{V}{a}$
Cho and Kensey (1991)	$\frac{3n+1}{4n}\frac{4V}{a}$
Mann and Tarbell (1990)	$\frac{3n+1}{4n}^{\frac{n}{1-n}}\frac{4V}{a}$
Thurston (1973)	$\frac{8V}{3a}$
Takami *et al.* (1990)	$\frac{V}{2a}$

Table 2.3: *Definitions of the characteristic shear rate in other studies. n is the power law index from the generalized Newtonian power law model.*

tions used by Baaijens *et al.* (1993) and Thurston (1973). Using *in-vivo* data from blood flow in the common carotid artery (Hoeks *et al.*, 1995) and $\lambda_{cy} = 0.1\ s$, equation (2.20) yields a shear rate number between 4 and 7. This means that the characteristic shear rate in this artery is in the shear thinning region of the viscosity of blood. Following these arguments, the shear thinning properties of blood for flow in the carotid artery should be taken into account.

In many investigations on blood flow in large arteries, blood is modeled as a Newtonian fluid. The viscoelasticity of blood is ignored, and using the argument that shear rate in larger arteries is predominantly high, the viscosity of blood is taken equal to the high shear rate limit viscosity of blood (η_∞).

Whether or not these assumptions are admissible is under dispute. Several numerical studies indicate that the influence of the shear thinning properties of blood is not significant for the flow in large arteries. Perktold *et al.* (1991) computed instationary flow in a three dimensional model of the carotid bifurcation, comparing a Newtonian model fluid ($\eta = 3.5 \ mPa.s$) to a Casson model fluid (equation (2.8), $\eta_c = 3.2 \ mPa.s$). They used identical flow conditions for the two fluids. At end diastole, they observed slightly flattened velocity profiles in the common carotid artery. In the carotid sinus, the secondary velocities were somewhat lower and the region of flow reversal slightly smaller for the Casson fluid. Despite these small differences, no significant influence of shear thinning properties on large scale flow phenomena in the internal carotid artery was found. Some numerical studies (e.g. Cho and Kensey, 1991) support their results, while other studies contradict them (e.g. Rodkiewicz *et al.*, 1990), or apply scaling procedures while comparing Newtonian and shear thinning model fluids (e.g. Baaijens *et al.*, 1993; Ballyk *et al.*, 1994).

From the above cited literature, it is obvious that there is no consensus as far as the influence of the non-Newtonian properties of the fluid is concerned. No detailed comparison between numerical and experimental results in complex flow is available, thus hampering evaluation of the influence of non-Newtonian fluid properties. In this thesis, the non-Newtonian flow in the carotid bifurcation (chapter 3) and in a $90°$ curved tube (chapter 4) will be studied both numerically and experimentally to investigate this topic.

2.4.2   Is viscoelasticity important?

Two dimensionless parameters are available to determine the importance of the viscoelasticity of a fluid: the Weissenberg number and the Deborah number. The definition of these two dimensionless parameters can be derived from the dimensionless form of the upper-convected Maxwell model:

$$De\frac{\partial \tau}{\partial t} + We(\mathbf{v} \cdot \nabla \tau - (\nabla \mathbf{v})^c \cdot \tau - \tau \cdot \nabla \mathbf{v}) + \tau = 2\mathbf{D} \qquad (2.23)$$

where τ is the dimensionless extra stress tensor, and $\mathbf{D}$ the dimensionless rate of deformation tensor. The stress tensor is made dimensionless with $\frac{L}{V\eta}$ and the rate of deformation tensor with $\frac{L}{V}$. The Weissenberg number (*We*) gives the ratio of the characteristic time of the fluid to a characteristic convective time-scale of the flow, while the Deborah number (*De*) relates the characteristic time of the fluid to the characteristic time of the flow:

$$We = \lambda_{ve}\dot{\gamma}_c \quad ; \quad De = \frac{\lambda_{ve}}{T} \qquad (2.24)$$

where λ_{ve} is the appropriate characteristic time constant of the fluid, and T a characteristic time of the flow. For $De \to 0$ and $We \to 0$, the elastic properties can be ignored and the fluid behaves in a purely viscous fashion. Above some critical value of De and We, the elastic properties of the fluid have to be taken into account. The values of De_{crit} and We_{crit}, usually in the order of one, have to be determined experimentally. There are three relevant time constants: the time constant associated with

the formation of the rouleaux, the time required to break down these structures, and finally the relaxation time of the deformed red blood cells. For the viscoelastic time constant of blood, the relaxation time of the red blood cells (0.06 *s*) seems to be the most appropriate choice (Cokelet, 1972; Sharp *et al.*, 1996). The Weissenberg number, depending on the characteristic shear rate, will be in the order of 1, while the Deborah number is one order of magnitude smaller. Based on the value of the Weissenberg number, the convective viscoelastic properties cannot be neglected in blood flow in large arteries. The influence of viscoelasticity on the velocity distribution and wall shear stress in blood flow in large arteries has not been investigated extensively, and will be addressed in chapter 3 and 4.

2.5 Conclusions

The choice of the appropriate constitutive model for blood depends on the properties of blood, the concentration distribution of red blood cells, and on the flow conditions in and the geometry of large arteries. The effect of the inhomogeneous concentration distribution is probably not significant for large scale flow phenomena: the cell-depleted layer is very small compared to the size of the artery and the arteries are too short to allow the development of shear induced migration. To predict the velocity distribution in large arteries, the shear thinning behavior and the viscoelastic properties of blood cannot be neglected on fore-hand. The characteristic shear rates in the large arteries are in the non-Newtonian regime of the shear rate dependent viscosity and the two dimensionless parameters characterizing the influence of viscoelasticity, *We* and *De*, are not small enough. From these observations, it follows that, for the prediction of the velocity field, blood should be modeled as a homogeneous, shear thinning and viscoelastic fluid. Using an appropriate blood analog fluid, this hypothesis must be investigated experimentally in a relevant geometry under physiological flow conditions. For the numerical modeling, a generalized Newtonian fluid model is used. In chapter 3, the steady flow of a non-Newtonian macroscopic blood analog fluid is investigated and the unsteady flow features are studied in a 90° curved tube (chapter 4). In these chapters, the influence of the non-Newtonian properties of the blood analog fluid on the velocity distribution are studied in detail. The ability of the blood analog fluid to mimic the behavior of blood is evaluated in backward-facing step flow (chapter 5). The experimental velocity distribution in a red blood cell suspension under steady flow conditions is compared to numerical results.

Wall shear stresses in the large arteries might be influenced by the particulate nature of blood. An independent measurement of the wall shear stress has to indicate whether a macroscopic blood analog fluid can be used to model wall shear stresses. For that purpose, a new method to determine the wall shear stress distribution is presented in chapter 6. The results for the developed model fluid will be confronted with a red blood cell suspension to evaluate its ability to mimic the blood flow in large arteries and to predict blood flow induced wall shear stress (chapter 7).

<div align="right">

Chapter 3

</div>

Steady non-Newtonian flow in a carotid bifurcation model [1]

3.1 Introduction

From clinical practice it is known that specific sites in the arterial tree are sensitive to the development of atherosclerotic lesions. Local hemodynamics are believed to play an important role in the development of these lesions. In view of the predilection of atherosclerosis for the non-divider wall in the sinus of the carotid bifurcation, atherogenesis (figure 3.1) was related to low or oscillating shear rate or shear stress (Caro *et al.*, 1971; Friedman *et al.*, 1981; Zarins *et al.*, 1983; Nerem, 1992). Local hemodynamics are not only governed by the pressure pulse, the geometry of the bifurcation and the properties of the arterial wall, but also by the rheological properties of the fluid. In this study, the influence of the non-Newtonian properties of blood on the velocity distribution in a rigid model of the carotid bifurcation under steady flow conditions is described.

Previous research has clearly demonstrated the non-Newtonian behavior of blood (Chien *et al.*, 1970; Thurston, 1973, 1979). In steady shear experiments, blood exhibits shear thinning behavior. At low shear rates, rouleaux of red blood cells are formed, effectively increasing the viscosity of blood. These structures break down at higher shear rates. The red blood cells orientate and deform and the viscosity of blood decreases, reaching a constant viscosity at high shear rates ($\eta_\infty = 3.5 \ mPa.s$). The viscoelastic properties of blood can be determined in oscillating shear flow. In

---

The literature review on the influence of the non-Newtonian properties of blood on flow in large arteries in the introduction is identical to the corresponding part of section 2.4.1.
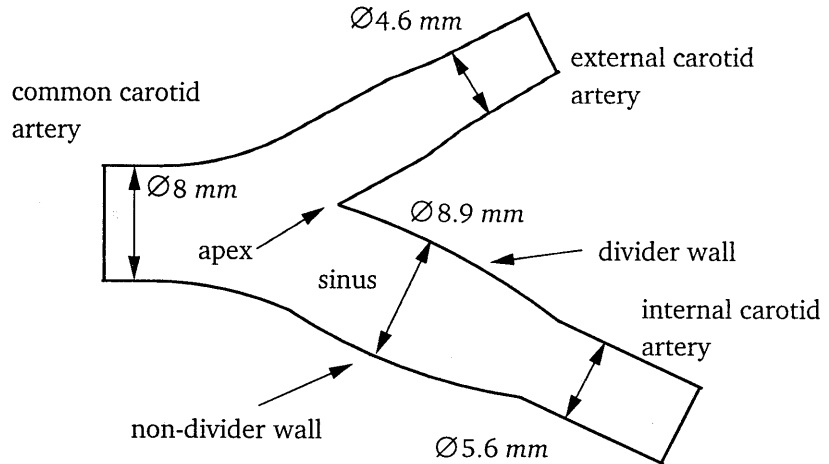
Figure 3.1: *Schematic representation of the carotid bifurcation.*

the linear viscoelastic regime, the complex viscosity of blood clearly shows the presence of an elastic component. The elastic component of the complex viscosity can be associated with the energy storing capacity of the deformable red blood cells and aggregates.

The flow in a carotid bifurcation model was studied experimentally by Bharadvaj *et al.* (1982a,b). They investigated the velocity distribution under steady flow conditions and found a complex flow field in the internal carotid artery in which secondary flows played an important role. They determined a region with low velocities near the non-divider wall that extended with increasing Reynolds number. At the divider wall of the carotid sinus a high shear region with high axial velocities was found, separated from the low shear region by a shear layer. The numerical work of Rindt *et al.* (1990) confirmed these results. The unsteady flow in the carotid bifurcation was studied by Perktold and Hilbert (1986); Ku and Giddens (1987); Rindt and van Steenhoven (1996) and Palmen *et al.* (1997). These studies showed that similar flow characteristics prevail, altered by the inertia effects induced by the pulsatility of the flow. The *in-vivo* study of Reneman *et al.* (1985) confirms these findings.

In the studies mentioned above, and many other investigations on blood flow in large arteries, blood was modeled as a Newtonian fluid. The viscoelasticity of blood was ignored, and using the argument that the shear rate in large arteries is predominantly high, the viscosity of blood was taken equal to the high shear rate limit viscosity of blood (η_∞). Whether or not these assumptions are admissible is under dispute. Several numerical studies indicate that the influence of the non-Newtonian properties of blood are not significant for the flow in large arteries. Perktold *et al.* (1991) computed instationary flow in a three dimensional model of the carotid bifurcation, accounting for the shear thinning properties of blood. They compared a Newtonian model fluid ($\eta = 3.5\ mPa.s$) to a Casson model fluid ($\eta_\infty = 3.2\ mPa.s$), using identical flow conditions for the two fluids. They observed slightly flattened velocity profiles

in the common carotid artery for the Casson fluid. In the carotid sinus, the secondary velocities were somewhat lower and the region of flow reversal slightly smaller for the Casson fluid. Despite these small differences, no significant influence of the shear thinning properties on the large scale flow phenomena in the internal carotid artery was found. Some numerical studies (e.g. Cho and Kensey, 1991)) support the results of Perktold *et al.* (1991) , while other studies contradict them (e.g. Rodkiewicz *et al.*, 1990), or apply scaling procedures while comparing Newtonian and shear thinning model fluids (e.g. Baaijens *et al.*, 1993; Ballyk *et al.*, 1994). None of the above studies incorporated the viscoelastic behavior of blood.

Experimental studies on non-Newtonian flow in larger arteries are relatively sparse, but the ones available indicate a significant influence of the viscoelasticity of the blood analog fluids on the flow phenomena. Liepsch and Moravec (1984) investigated the flow in a rigid 90° bifurcation under steady flow conditions. They found a striking influence of the non-Newtonian properties of a polyacrylamide solution on the axial velocity distribution. Especially the size and the location of the region of flow reversal were affected by the non-Newtonian properties of the fluid. Ku and Liepsch (1986) studied the axial velocity distribution in a 90° bifurcation under pulsatile flow conditions, also using a polyacrylamide solution. They found a reduction of the size of the region with flow reversal for the non-Newtonian fluid in a rigid model. It has to be remarked though, that polyacrylamide solution is much more elastic than blood.

In the present study, a blood analog fluid will be presented that can be used for laser Doppler anemometry (LDA) measurements in a Plexiglas model of the carotid bifurcation. The measured axial velocity distribution will be compared to finite element simulations. The viscoelastic properties of the blood analog fluid are not taken into account tin the numerical simulations. It will be shown that the non-Newtonian properties of the blood analog fluid significantly influence the axial velocity distribution. The measured velocity compares well to the numerical results, indicating that shear thinning is the dominant non-Newtonian property of the blood analog fluid.

3.2 Experimental methods

3.2.1 Blood analog fluid

The shear thinning and viscoelasticity of blood are closely related to its microscopic structure. The red blood cells determine the rheological behavior of blood; both shear thinning and viscoelasticity are related to aggregation, deformation and alignment of the red blood cells. A suitable blood analog fluid should include these non-Newtonian properties. Application of the blood analog fluid for LDA measurements in a three dimensional Plexiglas model imposes two additional requirements: transparency and a matched refraction index. A concentrated solution of potassium thiocyanate in water (KSCN, 71 % by weight) meets the latter two demands and was used as the Newtonian control fluid ($\eta = 2.9$ *mPa.s*, $\rho = 1410$ *kg.m^{-3}*) while addition of 250 *ppm* Xanthan gum (*95465 Fluka*) resulted in shear thinning and viscoelastic behavior. Aqueous Xanthan gum solutions have proven to be one of the more successful blood analog
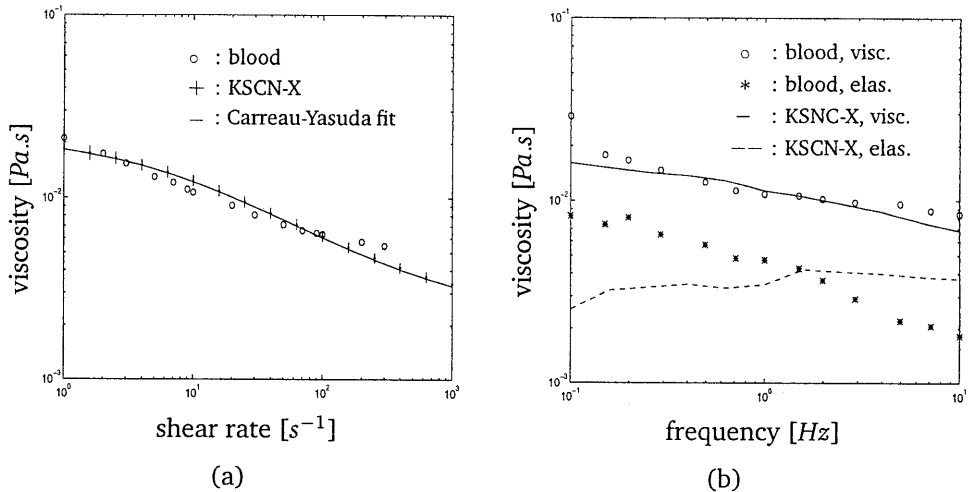
Figure 3.2: *Steady (a) and oscillatory (b) shear properties of the KSCN-X solution, compared to the properties of blood. The blood measurements were taken from Thurston (1979). The steady shear data of the KSCN-X solution are presented with vertical error-bars.*

fluids (Brookshier and Tarbell, 1993). The viscometric experiments, using a cone-plate viscometer (*RFSII, Rheometrics*), showed that the KSCN-Xanthan gum solution (KSCN-X) mimics the shear thinning properties of blood quite well (figure 3.2a). In oscillatory shear, the viscous components (η') and the elastic (η'') component of the complex viscosity of the KSCN-X solution were measured in the linear viscoelastic regime. Comparison with the linear viscoelastic properties of blood showed a good agreement for viscous component, but some differences regarding the elastic component (figure 3.2b). The microscopic mechanism responsible for the viscoelastic properties of the blood analog fluid will generally differ from those described for blood, and thus a complete match of all the rheological properties of blood is unlikely to be found. The properties of the KSCN-X solution were measured before and after the experiments. No differences were seen, indicating that the KSCN-X solution was not damaged by the pump.

3.2.2   Test rig

The geometry of the three dimensional model of the carotid bifurcation (figure 3.1) was derived from Bharadvaj *et al.* (1982a). The 1:1 model was machined out of PMMA (Plexiglas) with a refraction index of 1.491, and was identical to one used in the study of Rindt *et al.* (1990).
A schematic presentation of the fluid circuit is given in figure 3.3. The reservoir containing the measuring fluid was immersed in a container filled with water that was kept at a constant temperature (36°C). A positive displacement pump (*Moyno, Rob-*
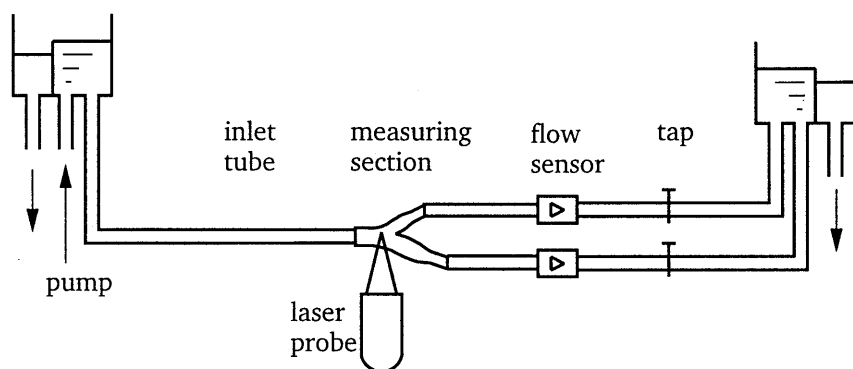
Figure 3.3: *The test rig.*

bins & Myers inc.) was used to pump the fluid to a constant head tank. This tank was successfully employed to eliminate disturbances of the stationary flow caused by the pump. Before entering the model of the carotid bifurcation, the fluid passed through an inlet tube of a length of $300a$, where a represents the radius of the common carotid artery. This inlet tube was necessary to guarantee a stable and fully developed flow as the fluid entered the measuring section. Return tubes with a tabs and flow sensors (sƗTransflow 601, Skalar Instruments) transported the fluid back to the reservoir. Titanium oxide flakes (*Iriodine 111, Merck*) were added to the fluid in a concentration of about 20 $g.m^{-3}$ to serve as seeding for the LDA measurements. The velocity measurements were performed by means of a two-component fiber optics LDA system in backscatter mode in combination with a Flow Velocity Analyzer (*FVA, 58N20, Dantec*). A 300 mW Argon-ion laser (*5500A, Ion Laser Technology*) generated a green laser beam ($\lambda = 514.5$ *nm*) and a blue laser beam ($\lambda = 488.0$ *nm*). Glass fibers transmitted the laser light to the measuring probe. A front lens with a focal length of 80 *mm* focused the laser beams to form a measuring volume (50 × 50 × 120 μm).

3.2.3   Experimental procedure

The velocity measurements were performed under steady flow conditions. The dimensionless parameters describing the flow, *Re* (Reynolds number) and γ (flow division ratio), were defined as follows:

$$Re = \frac{2\rho a V}{\eta}, \qquad \qquad \gamma = \frac{Q_E}{Q_C}, \qquad \qquad (3.1)$$

where V represented the cross sectional mean velocity in the common carotid artery, a the radius of the common carotid artery, η and ρ the dynamic viscosity and the density of fluid. Q_E and Q_C represent the flow through the external and common carotid artery, respectively. The experiments with the Newtonian fluid were performed for $Re = 270$ and $\gamma = 0.45$. Application of equation (3.1) to determine the *Re* number for the non-Newtonian is ambiguous, since η depends on shear rate. In this study,

the non-Newtonian fluid was subjected to the same flow conditions as the Newtonian fluid: the mean axial velocity and the flow division ratio were identical for the two fluids. The velocity distribution was measured at one site in the common carotid artery and at five sites in the internal carotid artery (figure 3.4). The axial velocity
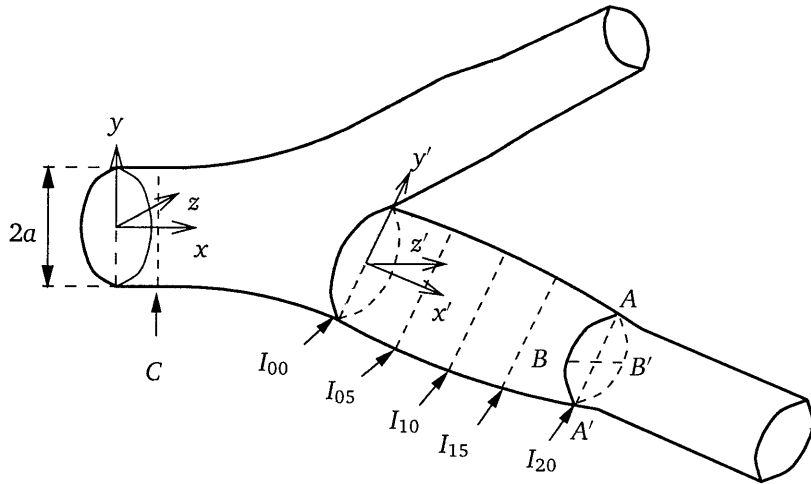
Figure 3.4: *The location of measurement sites.*

in the common carotid artery was measured $6a$ upstream of the apex, along the y-axis. In the internal carotid artery, the velocity distribution was mapped at I_{00}, I_{05}, I_{10}, I_{15} and I_{20}, each plane separated by a distance a along the x' axis. In the internal carotid artery, the velocity in the x and y direction was measured and subsequently transformed to the velocity in the x' direction. The velocity signals were computed as the mean of 100 measurements. Only half of the planes in the internal carotid artery were mapped because of symmetry. To check the validity of the symmetry assumption, I_{00} for the Newtonian fluid and I_{20} for the non-Newtonian fluid were measured completely.

3.3   Numerical methods

3.3.1   Newtonian fluid

The numerical modeling of steady, incompressible and isothermal flow of a (generalized) Newtonian fluid requires the solution of the impulse or Navier-Stokes equations and the continuity equation:

$$\begin{cases} \rho(\mathbf{v} \cdot \nabla)\mathbf{v} - \nabla \cdot \sigma = \mathbf{f} \\ \\ \nabla \cdot \mathbf{v} = 0 \end{cases} \qquad (3.2)$$

where $\mathbf{v}$ is the velocity vector, σ the Cauchy stress tensor, $\mathbf{f}$ the body force per unit mass, and ∇ the gradient operator. A constitutive equation is required to couple the Cauchy stress to the rate of deformation and/or the deformation of the fluid. For a Newtonian fluid with a constant dynamic viscosity η, the Cauchy stress tensor can be written as:

$$\sigma = -p\mathbf{I} + 2\eta\mathbf{D} \tag{3.3}$$

$$\mathbf{D} = \frac{1}{2}[\nabla\mathbf{v} + (\nabla\mathbf{v})^T] \tag{3.4}$$

where p is the pressure and $\mathbf{D}$ the rate of deformation tensor. Substitution of equations (3.3) and (3.4) in the Navier-Stokes equations, followed by a discretization, using Galerkin's finite element method (e.g. Cuvelier *et al.*, 1986), leads to the following set of non-linear differential equations:

$$\begin{cases} [\mathbf{S} + \mathbf{N}(\tilde{\mathbf{v}})]\tilde{\mathbf{v}} + \mathbf{L}^T\tilde{\mathbf{p}} = \tilde{\mathbf{f}} \\ \\ \mathbf{L}\tilde{\mathbf{v}} = 0 \end{cases} \tag{3.5}$$

where $\tilde{\mathbf{v}}$ and $\tilde{\mathbf{p}}$ are columns containing the unknown velocity components and pressure values in the discrete points, $\mathbf{S}$ the diffusion matrix, $\mathbf{N}(\tilde{\mathbf{v}})$ the non-linear convection matrix, $\mathbf{L}$ the divergence matrix, and $\tilde{\mathbf{f}}$ are columns containing the body and boundary forces. The convective term was linearized using the Newton-Raphson method. In the resulting system of linear equations (3.5), the boundary conditions are included. A parabolic velocity profile was prescribed as the axial inlet velocity in the common carotid artery. No-slip conditions served as the boundary conditions at the wall. Symmetry was prescribed for the symmetry plane and stress-free outflow was used for the internal and external carotid artery (see also figure 3.5). The length of the external carotid artery was used to control the flow division ratio γ. Equation (3.5) can be written in a compact form as:

$$\begin{bmatrix} \mathbf{S} + \mathbf{N}(\tilde{\mathbf{v}}) & \mathbf{L}^T \\ \mathbf{L} & 0 \end{bmatrix} \begin{bmatrix} \tilde{\mathbf{v}} \\ \tilde{\mathbf{p}} \end{bmatrix} = \begin{bmatrix} \mathbf{f} \\ 0 \end{bmatrix} \tag{3.6}$$

The set of linear differential equations was solved on the mesh depicted in figure 3.5. The Crouzeix-Raviart type elements contain 27 nodes, with a quadratic approximation for the three velocity components in each node. Both the pressure and the pressure gradient are defined at the centroïd of each element. The mesh consisted of 1084 elements and contained 10353 nodal points. The package SEPRAN (Segal, 1984) was employed to generate the mesh and to build and solve the system of equations. The equations (3.6) were solved using the integrated method (e.g. Cuvelier *et al.*, 1986). Renumbering of the unknown quantities $\tilde{\mathbf{v}}$ and $\tilde{\mathbf{p}}$ (Segal and Vuik, 1995) was performed to avoid zero diagonal elements in the assembled matrix in equation (3.6). The preconditoning of the assembled matrix according to a incomplete LU decomposition limited the required CPU time. A BiCGstab iterative solver was applied and the iteration process was stopped using the following criterion:

$$\frac{res^k}{res^0} \le \epsilon \quad ; \quad \epsilon = 10^{-5} \tag{3.7}$$
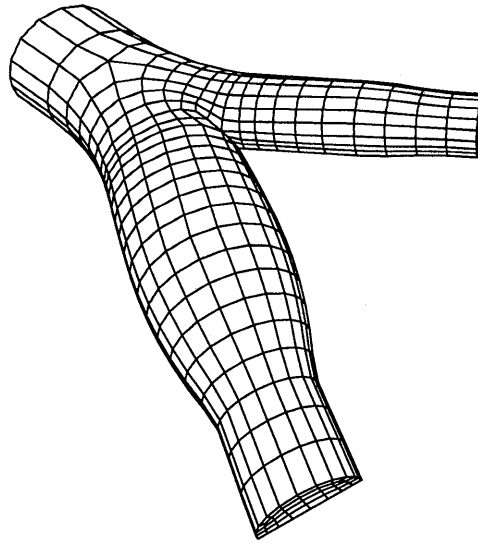
Figure 3.5: *The finite element mesh.*

with k the iteration number, and res^k and res^0 the residual at iteration k and 0 respectively. After each iteration process, the resulting velocity field (v^{l+1}) was compared to the velocity field from the previous iteration process (v^l) to test for convergence:

$$\|\mathbf{v}^{l+1} - \mathbf{v}^l\| \leq \epsilon \quad ; \quad \epsilon = 10^{-5} \tag{3.8}$$

with l the iteration step, and $\|...\|$ the maximum norm.

3.3.2   non-Newtonian fluid

In this study, only the shear thinning properties of the KSCN-X solution were taken into account. Since viscoelasticity was not included, the comparison of the numerical and experimental results should indicate whether viscoelasticity significantly alters the velocity distribution in carotid artery flow.

The shear thinning was accounted for by employing the Carreau-Yasuda model (e.g. Bird *et al.*, 1987):

$$\frac{\eta - \eta_\infty}{\eta_0 - \eta_\infty} = [1 + (\lambda\dot{\gamma})^a]^{\frac{n-1}{a}} \tag{3.9}$$

For $\dot{\gamma}$, a scalar measure of the rate of deformation tensor was used (Macosko, 1994).

$$II_{\mathbf{D}} = tr(\mathbf{D}^2) \tag{3.10}$$

$$\dot{\gamma} = \sqrt{2II_{\mathbf{D}}} \tag{3.11}$$

The Carreau-Yasuda model was fitted to the experimental data (solid line in figure 3.2a), resulting in the following set of parameters:

$$\eta_0 = 22 \; mPa.s \; ; \; \eta_\infty = 2.2 \; mPa.s \; ; \; a = 0.644 \; ; \; n = 0.392 \; ; \; \lambda = 0.110 \; s \tag{3.12}$$

The shear rate dependent viscosity slightly altered the computational method. The Cauchy stress tensor read:

$$\sigma = -p\mathbf{I} + 2\eta(\dot\gamma)\mathbf{D} \tag{3.13}$$

In the subsequent discretization, the diffusion tensor was non-linear:

$$\begin{cases} [\mathbf{S}(\tilde{\mathbf{v}}) + \mathbf{N}(\tilde{\mathbf{v}})]\tilde{\mathbf{v}} + \mathbf{L}^T\tilde{\mathbf{p}} = \tilde{\mathbf{f}} \\ \\ \mathbf{L}\tilde{\mathbf{v}} = \mathbf{0} \end{cases} \tag{3.14}$$

The non-linear diffusion matrix was linearized by application of the Picard method. The subsequent solution of the equations (3.14) was identical to the procedure followed for the Newtonian fluid.

3.4   Results

In figure 3.6 the axial velocity profile in the common carotid artery is given for the Newtonian and the non-Newtonian fluid. As the flow is fully developed, the axial velocity profile for the Newtonian fluid is parabolic. The velocity profile of the non-Newtonian fluid is flattened as expected for a shear thinning fluid (figure 3.6). The flattened velocity profile is predicted well by the numerical method. The errors in
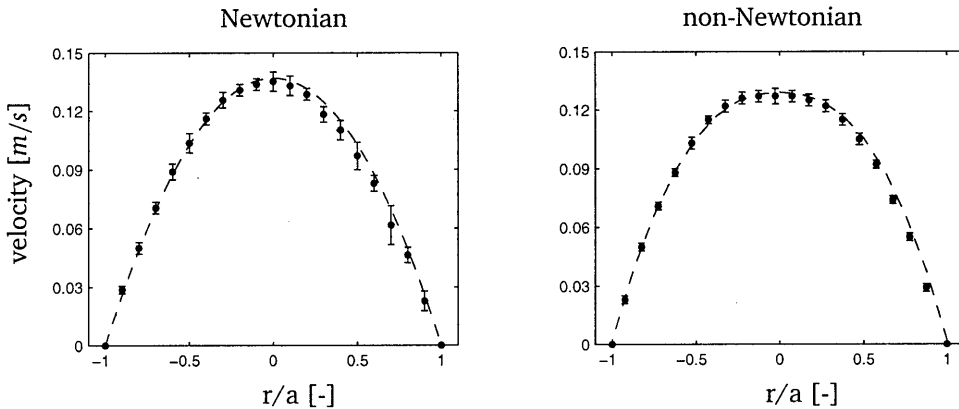
Figure 3.6: *The experimental (o) and numerical (− −) results of the axial velocity profile in the common carotid artery for the Newtonian fluid (KSCN) and the non-Newtonian fluid (KSCN-X).*

the velocity signal from the FVA can be attributed to the noise on the velocity signal and the presence of velocity gradients in the measuring volume. In the central part of the tube, the error in the velocity signal is less than 2 %, while at near wall sites, the presence of steep velocity gradients causes an increase of the maximum error to

8 %. The influence of alignment and positioning errors and fluctuations of the flow is estimated to be less than 3 % (see also Rindt *et al.*, 1991).

In figures 3.7 and 3.8, the experimental and numerical results in the internal carotid artery are given for the Newtonian and the non-Newtonian fluid respectively. The axial velocity in the plane of symmetry and perpendicular to this plane are presented ($A - A'$ and $B - B'$ in figure 3.4) The isovelocity lines for the complete cross section are given at plane I_{00}, I_{10} and I_{20}. The isovelocity line for $v = 0$ is presented by a dashed line. The numerical results for the Newtonian and the non-Newtonian fluid are compared in figure 3.9.

Newtonian (exp) vs. Newtonian (num)

The axial velocity distribution gives an indication of the complex flow phenomena in the internal carotid artery. As the fluid enters the bifurcation, it is split by the apex. As a result, high velocity gradients are expected at the divider wall (plane I_{00}). Another important geometrical factor is the curvature effect, originating from the transition from the common carotid artery and the internal carotid artery. The faster moving fluid in the central part of the tube is swept towards the divider wall and is replaced by slower moving fluid particles near the non-divider wall. The fluid near the divider wall is transported circumferentially towards the non-divider wall. This secondary flow pattern (Dean vortex) results in C-shaped axial isovelocity lines at all locations. The internal carotid artery itself has a prominent feature that influences the flow: its changing cross sectional area. The cross sectional area first increases, reaching its maximum value at plane I_{10}, and then decreases. The increase of the cross sectional area results in an adverse pressure gradient. The fluid is decelerated, and especially the low impetus fluid near the non-divider wall is affected by this adverse pressure gradient. Together with the curvature effect, this results in flow reversal near the non-divider wall at plane I_{05} and I_{10}. From plane I_{10} on, the cross sectional area reduces again, and the fluid is accelerated, resulting in a slightly flattened axial velocity distribution and high wall shear rates at plane I_{20}. Finally, the presence of a shear layer, separating the low velocity area in the central part of the cross section from the area with high velocities near the divider wall, is notable at plane I_{10} and I_{15}. The axial velocity distribution at plane I_{00} shows that the assumption of symmetry is valid. The flow features described above, agree well with previous studies on the steady flow in carotid artery models (e.g. Bharadvaj *et al.*, 1982b; Rindt *et al.*, 1990; Palmen *et al.*, 1997).

The comparison between the numerical and experimental results reveals good agreement. The high velocity gradients near the divider wall, flow reversal near the non-divider wall, the presence of the shear layer and the C-shaped axial isovelocity lines are predicted well.
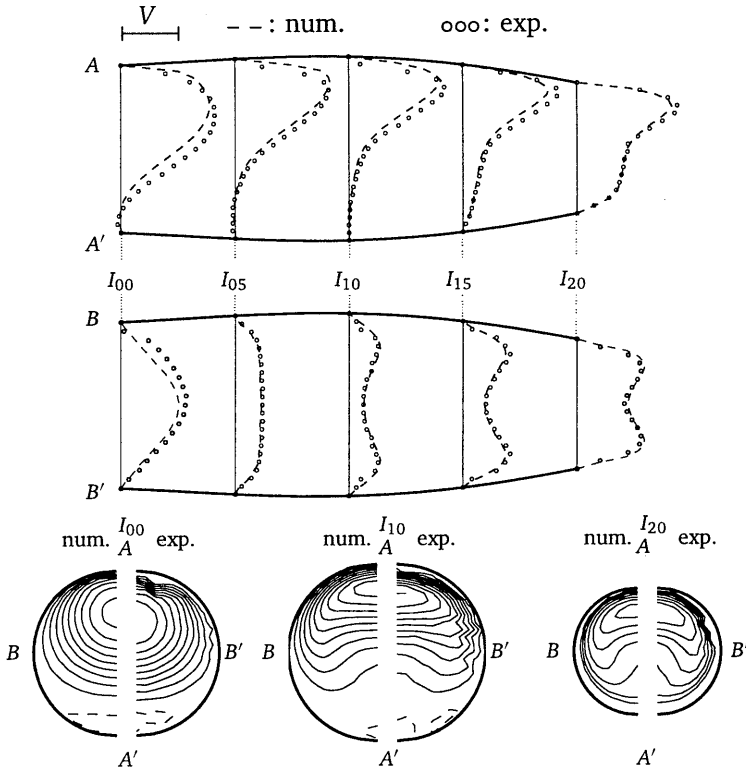
Figure 3.7: *The experimental and numerical axial velocity distribution for the Newtonian fluid. The axial velocity in the symmetry plane $(A - A')$ and perpendicular to this plane $(B - B')$ are presented in the two top figures and the contour plots for I_{00}, I_{10} and I_{20} are given in the bottom part of the figure (see also figure 3.4). The mean axial velocity in the common carotid artery (V), is indicated. The area with flow reversal is given by the dashed line in the contour plots.*

non-Newtonian (exp) vs. non-Newtonian (num)

The geometrical features of the carotid bifurcation also dominate the flow features for the non-Newtonian fluid. The flow division at the apex causes high velocities near the divider wall, the divergence of the lumen results in reduced velocities near the non-divider wall, and the convergence of the lumen is responsible for the increased velocity at plane I_{20}. The influence of the secondary flow on the axial velocity distribution is much less pronounced, as can be seen from the axial isovelocity lines. The
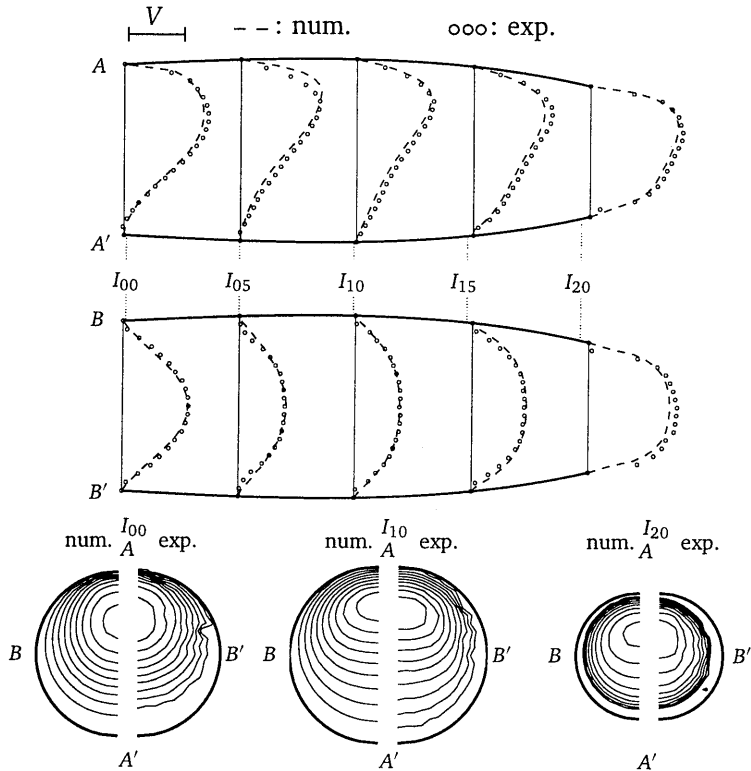
Figure 3.8: *The experimental and numerical axial velocity distribution for the non-Newtonian fluid. The axial velocity in the symmetry plane (A − A') and perpendicular to this plane (B − B') are presented in the two top figures and the contour plots for I_{00}, I_{10} and I_{20} are given in the bottom part of the figure (see also figure 3.4). The mean axial velocity in the common carotid artery (V), is indicated.*

viscoelastic properties of the fluid were not included in the numerical model. Despite this simplification, the agreement between the experimental and numerical results is good. As a consequence, it must be concluded that the viscoelasticity of the KSCN-X solution under steady flow conditions does not influence the velocity distribution in the carotid bifurcation significantly.

Newtonian (num) vs. non-Newtonian (num)

A comparison between the Newtonian and the non-Newtonian results reveals the influence of the shear thinning properties of the KSCN-X solution on the velocity distribution. Since for both the Newtonian and the non-Newtonian fluids the experimental results were predicted quite accurately by the numerical code, the numerical results are used for the comparison. The flow division at the apex results in high shear rates
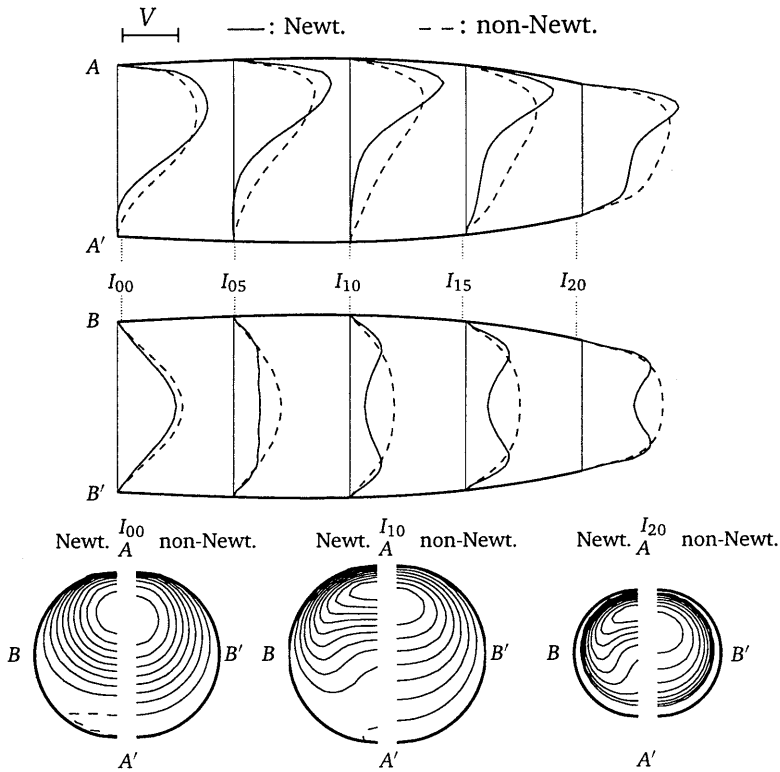
Figure 3.9: *Comparison of the computed axial velocity distribution for the Newtonian and the non-Newtonian fluid. The axial velocity in the symmetry plane (A − A′) and perpendicular to this plane (B − B′) are presented in the two top figures and the contour plots for I_{00}, I_{10} and I_{20} are given in the bottom part of the figure (see also figure 3.4). The mean axial velocity in the common carotid artery (V), is indicated. The area with flow reversal is given by the dashed line in the contour plots.*

near the divider wall. The velocity gradients are less steep for the KSCN-X solution. The flattened axial velocity profile in the common carotid artery might contribute to lower velocity gradients near the divider wall. The axial velocity distribution shows significant flattening and higher velocities near the non-divider wall. At the planes I_{05} and I_{10}, the shift of the peak axial velocity towards the divider wall is less pro-

nounced for the non-Newtonian fluid. The typical 'C'-shape in the contour plot of the axial velocity distribution, as present in the Newtonian case, is absent. The axial velocity profiles are flatter and the peak axial velocity is significantly lower. The region of flow reversal is absent for the non-Newtonian fluid. Further downstream, substantially lower axial velocity in the center of the vessel can be seen for the Newtonian fluid whereas the non-Newtonian fluid shows an almost fully recovered velocity profile at plane I_{20}.

3.5   Discussion and conclusion

Laser Doppler anemometry and numerical analyses were applied to obtain detailed quantitative information on axial velocity distribution in a three dimensional model of the carotid bifurcation for a Newtonian and non-Newtonian fluid under steady flow conditions. A concentrated KSCN solution with 250 *ppm* Xanthan gum served as a blood analog fluid. The investigation of the influence of the non-Newtonian properties of blood on the flow phenomena in a model of the carotid bifurcation was the main goal of this study. The distensibility of the vessel wall, pulsatility of the flow and the compliance of the arterial tree downstream of the bifurcation were not included in this study. Direct comparison of the results of this study with *in-vivo* velocity measurements in the carotid bifurcations is not possible because of the assumptions mentioned above. By carefully controlling the experimental conditions, this study provides the means to evaluate the influence of the non-Newtonian properties of the blood analog fluid on the flow patterns in the carotid bifurcation.
The velocity distribution for the Newtonian fluid in the internal carotid artery compares well to previous studies (Bharadvaj *et al.* (1982b); Rindt *et al.* (1990); Palmen *et al.* (1997)). The dominant features are flow separation, secondary flow due to the curvature, flow reversal due to widening of the lumen and the effect of the convergence of the lumen. Differences between the measured velocity distribution of the Newtonian and non-Newtonian fluid are evident. In the common carotid artery the non-Newtonian fluid shows a flattened axial velocity profile due to its shear thinning behavior. In the internal carotid artery, the non-Newtonian velocity field is flattened, has lower velocity gradients at the divider wall, and positive velocity gradients at the non-divider wall. Furthermore, the curvature induced secondary flow seems to be less dominant. The non-Newtonian flow in the carotid bifurcation was predicted quite well by the numerical simulations. The fact that only the shear thinning properties were included and that viscoelasticity was ignored in the numerical simulations indicates that shear thinning is the dominant non-Newtonian property of the blood analog fluid and that viscoelasticity can be ignored for the prediction of the axial velocity distribution. The effect of the non-Newtonian properties on oscillating flow features and wall shear stress remains to be investigated.
The results of Perktold *et al.* (1991) seem to disagree with the results obtained in the present study. They found only a minor influence of shear thinning on the end-diastolic flow features in the carotid bifurcation. The diameter of the common carotid artery in their study was smaller (6.2 *mm*), and the mean axial velocity higher. As a

consequence, the shear rates were higher. Under these circumstances, the influence of the shear thinning properties on the velocity distribution can be expected to be less dominant. Baaijens *et al.* (1993) studied the velocity distributions in a 2D model of the carotid bifurcation for a Newtonian and two non-Newtonian fluids numerically, and found only minor differences. They used a scaling procedure, involving increased mean axial velocity for the non-Newtonian fluids, thus increasing shear rate. The influence of the shear thinning properties can therefore expected to be smaller than in our study. The experimental results of Liepsch and Moravec (1984) and Ku and Liepsch (1986) showed a dramatic influence of the non-Newtonian properties of the blood analog fluid on the velocity patterns. The polyacrylamide solution, used as a blood analog fluid in these studies, is highly elastic. The results of Mann and Tarbell (1990) showed that polyacrylamide solutions are inadequate to mimic the behavior of blood. No reports on detailed velocity measurements, using an aqueous Xanthan gum solution as a blood analog fluid, could be found.

From this study, and the results of Perktold *et al.* (1991), it can be concluded that the influence of the shear thinning properties on the velocity distribution in larger arteries strongly depends on slight variations in shear rate. The validity of the scaling procedure, used by Baaijens *et al.* (1993), requires further research. Furthermore, the influence of viscoelasticity for unsteady flow conditions, and the validity of the blood analog fluid to mimic the behavior of blood have to be investigated. The 90° curved tube will serve as a model geometry for future experiments and simulations: the flow contains similar flow characteristics (secondary flow, skewed axial velocity profiles), without being influenced by a complex geometry.

Acknowledgements

<div align="right">Chapter 4</div>

Unsteady non-Newtonian flow in 90° curved tube [1]

4.1 Introduction

From clinical practice it is known that specific sites in the arterial tree are sensitive to the development of atherosclerotic lesions, causing progressive occlusion of the lumen of arteries. Local hemodynamics are believed to play an important role in the development of those lesions. The predilection of atherosclerosis for bends and bifurcations can be related to low or oscillating shear rates or shear stresses (Caro *et al.*, 1971; Friedman *et al.*, 1981; Zarins *et al.*, 1983; Nerem, 1992). The study of velocity distribution and wall shear stresses in a 90° curved tube can be used to gain more insight into the hemodynamical factors that promote the development of atherosclerosis.

Newtonian flow

The fully developed steady flow in loosely curved tubes was first analyzed by Dean (1927, 1928). Using stream functions and a perturbation method, Dean was able to solve the equations of motion. He found that the flow in the curved tube was governed by one dimensionless parameter, the Dean number. The Dean number is a combination of a geometry factor (curvature ratio, $\delta = \frac{a}{R}$, where a is the radius of the

---

Parts of the sections Introduction, Experimental methods and Numerical methods are almost identical to the previous chapter. The section on the dimensionless parameters in non-Newtonian flow is almost identical to the discussion in section 2.4.

tube and R is the radius of the curvature) and the Reynolds number ($Re = \frac{2\rho aV}{\eta}$, where V is the characteristic velocity, η the dynamic viscosity and ρ the density of the fluid). For time dependent fully developed flows, an additional dimensionless parameter is required. In literature on blood flow, the Womersley parameter ($\alpha = a\sqrt{\frac{\rho\omega}{\eta}}$, where ω is the frequency of the flow oscillation) is often used to characterize time dependent flow phenomena. Dean's theory was extended to include flow at a wide range of Dean numbers, curvature ratios, and Womersley parameters: a review of these studies is given by Pedley (1980) and Berger *et al.* (1983).

The entry flow in curved tubes, either developing from a parabolic or a uniform inlet velocity profile, is more complex. Only a few analytical studies are available (Singh, 1974; Yao and Berger, 1974; Pedley, 1980) and the applicability of these studies is often limited. Due to the complexity of the problem, several studies apply computational methods to solve the equations of motion for the entry flow in curved tubes. For the steady entry flow, developing from a uniform velocity profile, one is referred to e.g. Agrawal *et al.* (1978); Soh and Berger (1984). Development from a parabolic entry profile was studied by Olson and Snyder (1985); Bovendeerd *et al.* (1987) and van de Vosse *et al.* (1989). Unsteady entry flow, especially relevant for physiological flow in the arterial system, was studied by Mullin and Greated (1980); Chandran and Yearwood (1981); Talbot and Chong (1983); Rindt *et al.* (1991) and Naruse and Tanishita (1996).

non-Newtonian flow

Previous studies clearly demonstrated the non-Newtonian behavior of blood (Chien *et al.*, 1970; Thurston, 1979). In steady shear experiments, blood exhibits shear thinning behavior. Rouleaux of red blood cells are formed at low shear rates, effectively increasing the viscosity of blood. These structures break down at higher shear rates. The red cells orientate and deform and the viscosity of blood decreases. In oscillating shear flow, the viscoelastic properties of blood can be determined. In the linear viscoelastic regime, the complex viscosity of blood clearly shows the presence of an elastic component. The elastic component of the complex viscosity can be associated with the energy storing capacity of the deformable red blood cells and aggregates. Despite these findings, blood flow in larger arteries is usually modeled as a Newtonian fluid.

In the available literature, the assumption that in large arteries blood behaves like a Newtonian fluid, is under dispute. Several numerical studies indicate that the influence of the shear thinning properties of blood on the velocity distribution in complex flows are not very significant. Perktold *et al.* (1991) used the generalized Newtonian Casson model to compute instationary flow in a three dimensional model of the carotid bifurcation. They compared the Newtonian model fluid ($\eta = 3.5\ mPa.s$) to a Casson model fluid ($\eta_\infty = 3.2\ mPa.s$), using identical flow conditions for the two fluids. They observed slightly flattened velocity profiles in the common carotid artery for the Casson fluid. In the carotid sinus, the secondary velocities were somewhat lower and the region of flow reversal slightly smaller for the non-Newtonian fluid. Despite

these small differences, no significant influence of shear thinning on the large scale flow phenomena in the internal carotid artery was found. Some numerical studies (e.g. Cho and Kensey, 1991) confirm the results of Perktold *et al.* (1991), while other studies contradict them (e.g. Rodkiewicz *et al.*, 1990)), or apply scaling procedures while comparing Newtonian and non-Newtonian flow (Baaijens *et al.*, 1993; Ballyk *et al.*, 1994).

Experimental studies on viscoelastic flow in larger arteries are relatively sparse but indicate a significant influence of the viscoelasticity of the fluids on the flow phenomena. Liepsch and Moravec (1984) investigated the flow in a rigid 90° bifurcation under steady flow conditions. They found a striking influence of the non-Newtonian properties of a polyacrylamide solution on the axial velocity distribution. Especially the size and the location of the region of flow reversal were affected by the non-Newtonian properties of the fluid. Ku and Liepsch (1986) studied the axial velocity distribution in a 90° bifurcation under pulsatile flow conditions, also using a polyacrylamide solution. They found a reduction of the size of the region with flow reversal for the non-Newtonian fluid. One should realize though, that a polyacrylamide solution is much more elastic than blood. Mann and Tarbell (1990) applied a flush mounted hot film anemometer to evaluate the influence of non-Newtonian fluids on the magnitude of wall shear rate in a bend. They compared the shear rates of one Newtonian and three blood- analog fluids and found significantly higher wall shear rates in oscillatory flow for the viscoelastic fluids, especially at the inner bend. This study is of particular interest because it includes wall shear rate measurements, induced by blood flow.

The available literature on non-Newtonian flow in curved tubes is limited. Several analytical studies extended Dean's theory to include a range of generalized Newtonian and viscoelastic constitutive models. Most of the theoretical investigations are limited to fully developed flow at low Dean numbers (e.g. Jones, 1960; Clegg and Power, 1963; Bowen *et al.*, 1991; Robertson and Muller, 1996). Das (1992) used a boundary layer approximation to study fully developed flow at high Dean numbers. The unsteady fully developed flow for a viscoelastic fluid was studied by James (1975). To the authors best knowledge, no analytical studies are available to incorporate the non-Newtonian fluid properties in the equations of motion to investigate entry flow. The experimental studies on non-Newtonian flow in curved tubes are mostly limited to pressure drop measurements (e.g. Singh and Mishra, 1980). Takami *et al.* (1990) studied the entry flow of non-Newtonian fluids both numerically and experimentally. They used two different non-Newtonian fluids and applied a power law model to validate the experimental results. They found good agreement between experimental and numerical results, but did not include unsteady flow in their study.

Outline of the study

In this study, the unsteady flow of a Newtonian and a non-Newtonian blood analog fluid was investigated both numerically and experimentally. Both fluids were subjected to identical flow conditions and the velocity distribution in a 90° curved tube was studied in detail. Comparison between the experimental results for the Newto-

nian and non-Newtonian fluid revealed the influence of the non-Newtonian proper-
ties of the blood analog fluid. In the numerical simulations, viscoelasticity was not
included, thus allowing for a discrimination between the influence of shear thinning
and viscoelasticity on the velocity distribution.

4.2   Dimensionless parameters in non-Newtonian flow

The impact of the non-Newtonian properties of blood on the flow phenomena in large
arteries does not only depend on the fluid properties, but also on the flow conditions
the fluid is subjected to. Dimensionless parameters, consisting of a fluid parameter
and a flow parameter, can be used to estimate the combined effect of fluid proper-
ties and flow conditions. After adopting a constitutive model, three dimensionless
parameters can be formulated. To model the shear thinning properties of blood, the
Carreau-Yasuda model was employed (equation 4.1). The dimensionless viscosity
(η^*) can be written as:

$$\eta^* = \frac{\eta - \eta_\infty}{\eta_0 - \eta_\infty} = [1 + (\lambda_{cy}\dot{\gamma})^a]^{\frac{n-1}{a}} \tag{4.1}$$

where η is viscosity and $\dot{\gamma}$ shear rate. This model describes the behavior of fluids with
Newtonian plateaus at low (η_0) and high shear rate (η_∞), and a transition area gov-
erned by the parameters n, a and λ_{cy}. Using these observations, a shear rate number
can be defined:

$$N_{\dot{\gamma}} = \lambda_{st}\dot{\gamma}_c \tag{4.2}$$

where λ_{st} is a characteristic time constant and $\dot{\gamma}_c$ a characteristic shear rate. For high
values of the shear rate number $N_{\dot{\gamma}}$, the fluid will behave as a Newtonian fluid with
$\eta = \eta_\infty$, while at low values of $N_{\dot{\gamma}}$ a Newtonian model with $\eta = \eta_0$ can be used. At
intermediate values, the shear thinning behavior must be taken into account. Two
dimensionless parameters are available to determine the importance of the viscoelas-
ticity of a fluid: the Weissenberg number and the Deborah number. The definition of
these two dimensionless parameters can be derived from the dimensionless form of
the upper-convected Maxwell model:

$$De\frac{\partial \tau}{\partial t} + We(\mathbf{v} \cdot \nabla\tau - (\nabla\mathbf{v})^c \cdot \tau - \tau \cdot \nabla\mathbf{v}) + \tau = 2\mathbf{D} \tag{4.3}$$

where τ is the dimensionless stress tensor, and $\mathbf{D}$ the dimensionless rate of deforma-
tion tensor. The stress tensor is made dimensionless with $\frac{L}{V\eta}$. The rate of deformation
tensor is made dimensionless with $\frac{L}{V}$. The Weissenberg number (We) gives the ratio
of the characteristic time of the fluid to a characteristic convective time-scale of the
flow, while the Deborah number (De) relates the characteristic time of the fluid to the
characteristic time of the flow:

$$We = \lambda_{ve}\dot{\gamma}_c \quad ; \quad De = \frac{\lambda_{ve}}{T} \tag{4.4}$$

where λ_{ve} is the appropriate characteristic time constant of the fluid, and T a characteristic time of the flow. For $De \rightarrow 0$ and $We \rightarrow 0$, the elastic properties can be ignored and the fluid behaves in a purely viscous fashion. Above some critical value of De and We, the elastic properties of the fluid have to be taken into account. The values of De_{crit} and We_{crit}, usually of order one, have to be determined experimentally.

The values of λ_{st}, λ_{ve}, T and $\dot{\gamma}_c$ have to be determined to obtain the values of the above mentioned dimensionless parameters for blood flow in large arteries. For λ_{st}, the time constant in the Carreau-Yasuda model (λ_{cy}) can be used, and its value follows from viscometric data. For the viscoelastic time constant of blood, the relaxation time of the red blood cells (0.06 s) seems to be the most appropriate choice (Cokelet, 1972; Sharp *et al.*, 1996). The characteristic time-scale of the flow (T) is equal to the period time of the physiological flow pulse. The characteristic shear rate for the blood flow in larger arteries can be defined in various ways: some authors use wall shear rate, which in fact is often the highest shear rate occurring in blood flow, while others use a shear rate based on an average value (table 4.1). In this study, a simple definition,

study	definition of $\dot{\gamma}_c$
Baaijens *et al.* (1993)	$\frac{\pi V}{a}$
Ballyk *et al.* (1994)	$\frac{V}{a}$
Cho and Kensey (1991)	$\frac{3n+1}{4n}\frac{4V}{a}$
Mann and Tarbell (1990)	$\frac{3n+1}{4n}^{\frac{n}{1-n}}\frac{4V}{a}$
Takami *et al.* (1990)	$\frac{V}{2a}$
Thurston (1973)	$\frac{8V}{3a}$

Table 4.1: *Definitions of the characteristic shear rate in other studies.* n *is the power law index from the generalized Newtonian power law model.*

based on the average shear rate in a two dimensional Poiseuille flow, is used:

$$\dot{\gamma}_c = \frac{2V}{a} \tag{4.5}$$

The definition of the characteristic shear rate shows resemblance to the definitions used by Thurston (1973) and Baaijens *et al.* (1993).

The above mentioned dimensionless parameters, depending on fluid properties and flow conditions, will be used to estimate the importance of shear thinning and viscoelasticity.

4.3   Experimental methods

4.3.1   Blood analog fluid

The shear thinning and viscoelasticity of blood are closely related to its microscopic structure. The red blood cells determine the rheological behavior of blood: both shear thinning and viscoelasticity are related to aggregation, deformation and alignment of the red blood cells. A suitable blood analog fluid should include the non-Newtonian properties of blood. Application of the blood analog fluid for laser Doppler anemometry (LDA) in a three dimensional Plexiglas model imposes two additional requirements: transparency and a matched refraction index. A concentrated solution of potassium thiocyanate (KSCN, 71 % by weight) meets the latter two demands and was used as the Newtonian control fluid ($\eta = 2.9\ mPa.s$, $\rho = 1410\ kg.m^{-3}$) while addition of 250 ppm Xanthan-gum (*95465 Fluka*) resulted in shear thinning and viscoelastic behavior. Viscometric experiments, using a cone-plate viscometer (*RFSII, Rheometrics*), showed a good agreement between the KSCN-Xanthan gum solution (KSCN-X) and blood for the shear thinning behavior (figure 4.1). The Carreau-Yasuda
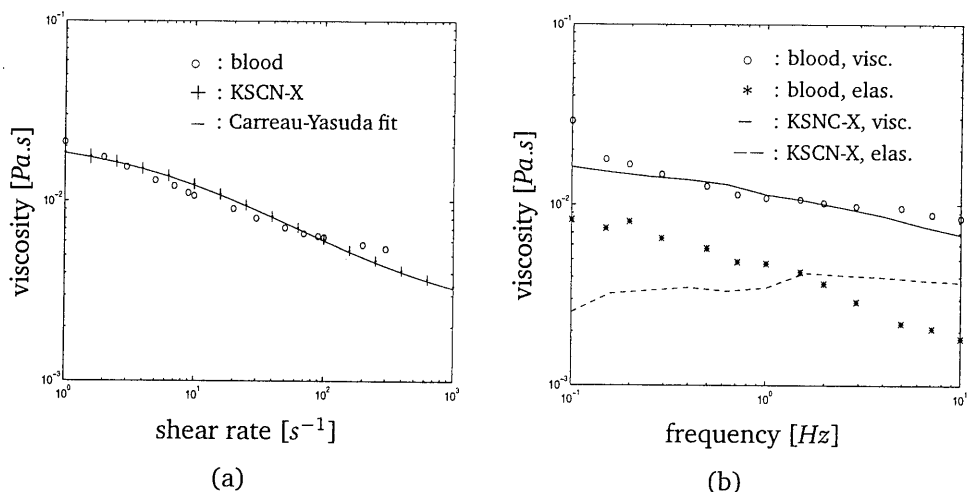
Figure 4.1: *Shear thinning (left) and linear viscoelastic (right) properties of the KSCN-X solution, compared to the properties of blood. The blood measurements were taken from Thurston (1979). The steady shear data of the KSCN-X solution are presented with vertical error-bars.*

model was fitted to the experimental data (solid line in figure 4.1a), resulting in the following set of parameters:

$$\eta_0 = 22\ mPa.s\ ;\ \eta_\infty = 2.2\ mPa.s\ ;\ a = 0.644\ ;\ n = 0.392\ ;\ \lambda = 0.110\ s \quad (4.6)$$

The results of oscillatory shear experiments showed that the linear viscoelastic properties of the KSCN-X solution did not match the properties of blood very well. The fit of a four-mode Maxwell model to the linear viscoelastic data rendered a relaxation time of the KSCN-X solution of 0.3 s. The microscopic mechanism responsible for the viscoelastic properties of the KSCN-X solution differ from those for blood, and thus it is not likely that a complete match of all the rheological properties of blood can be found. The properties of the KSCN-X solution were measured before, during and after the LDA experiments. No differences were seen, indicating that the KSCN-X solution was not damaged by the pump.

4.3.2   Test rig

The velocity measurements were performed in a three dimensional model of a curved tube, using LDA. A schematic presentation of the fluid circuit is given in figure 4.2. The reservoir containing the measuring fluid was immersed in a container filled with water that was kept at a constant temperature (36°C). A positive displacement pump (*Moyno, Robbins & Myers inc.*) was used to pump the fluid to a constant head tank. This constant head tank was successfully employed to eliminate disturbances of stationary flow caused by the pump. The unsteady flow component was generated by a computer controlled piston pump (*Vitro Systems Inc.*). The model of the 90° curved tube was made of Plexiglas. The diameter of the tube was 8 mm, and the curvature radius was 24 mm. Before entering the model of the 90° curved tube, the fluid passed through an inlet tube of a length of 200a, where a represents the radius of the tube. This inlet tube was necessary to guarantee a stable and fully developed flow as the fluid entered the measuring section. A return tube with a tab and flow sensor (*Transflow 601, Skalar Instruments*) transported the fluid back to the reservoir. Titanium-oxide flakes (*Iriodine 111, Merck*) were added to the fluid in a concentration of about 20 $g.m^3$ to serve as seeding for the LDA measurements. The velocity measurements were performed by means of a two-component fiber optics LDA system in backscatter mode in combination with a Flow Velocity Analyser (*58N20, Dantec*). A 300 mW Argon-ion laser (*5500A, Ion Laser Technology*) generated a green ($\lambda = 514.5$ nm) and a blue laser beam ($\lambda = 488.0$ nm). Glass fibers transmitted the laser light to the measuring probe. A front lens with a focal length of 80 mm focused the laser beams to form a measuring volume ($50 \times 50 \times 120$ μm).

4.3.3   Experimental procedure and error estimation

The velocity measurements, using the Newtonian KSCN solution, were performed under unsteady flow conditions. The mean axial velocity (V) as a function of time is given in figure 4.2. *Re* varied from 300 (diastole) to 750 (peak systole), while α based on the period time of the flow pulse ($T = 1$ s) was equal to 7. After mapping the velocity field for the Newtonian control fluid, 250 ppm Xanthan gum was added to the KSCN solution and the measurements were repeated for identical flow rate and period time of the flow pulse. Since the viscosity of the KSCN-X solution depends on the shear rate, determination of *Re* and α is not trivial. This issue will be discussed in
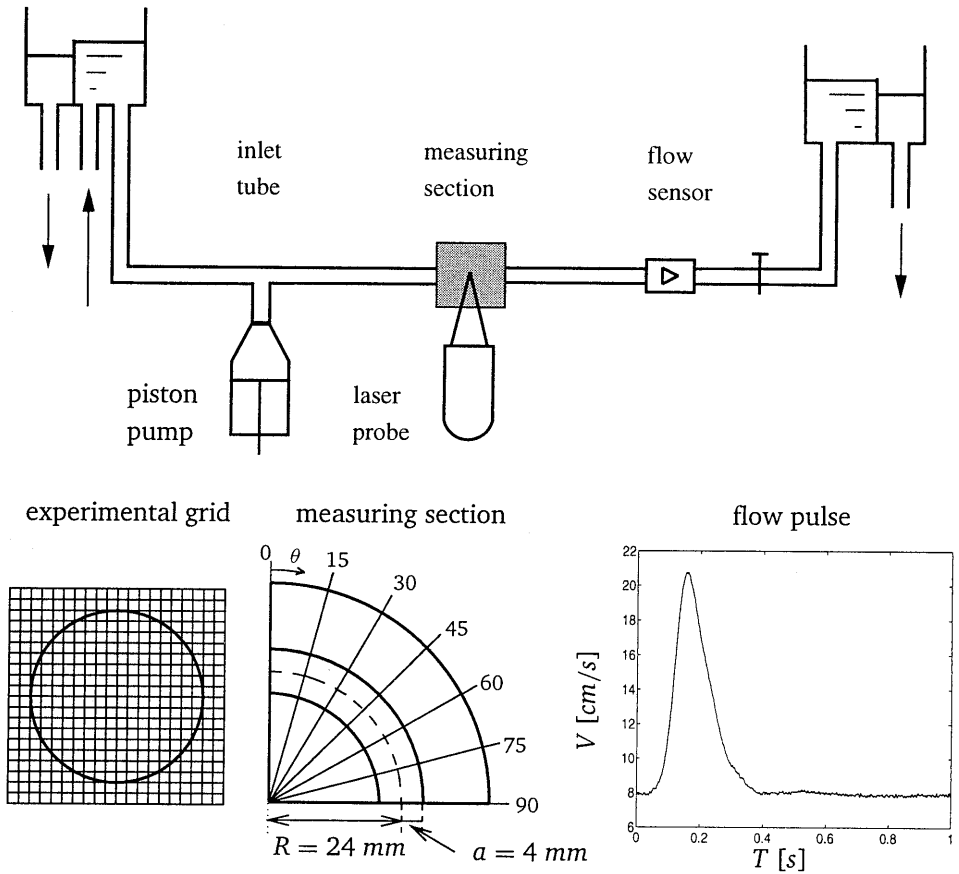
Figure 4.2: *The test rig is shown in the upper part. In the bottom part, the experimental grid is shown on the right side. The measuring section indicates the planes for the velocity measurements. The flow pulse is shown on the left side. The mean axial velocity (V) was obtained from the flow sensor.*

the section 4.6.

The flow parameters, fluid properties and the dimensionless parameters for the non-Newtonian flow are summarized in table 4.2. The values for the KSCN-X solution are compared to *in-vivo* measurements of Hoeks *et al.* (1995). The shear thinning properties of blood are assumed to be identical to the KSCN-X solution and the flow pulse frequency is assumed to be 70 beats per minute. The values for blood[1] refer to healthy young individuals while the data for blood[2] originates from older individuals (table 4.2). End-diastolic values are used to determine the mean axial velocity. From

fluid	flow parameters			fluid properties		dimensionless parameters		
	a	V	T	λ_{st}	λ_{ve}	$N_{\dot{\gamma}}$	We	De
	mm	$cm.s^{-1}$	s	s	s	$-$	$-$	$-$
blood[1]	3.3	12.0	0.85	0.1	0.06	7.3	4.4	0.07
blood[2]	3.9	7.8	0.85	0.1	0.06	4.0	2.4	0.07
KSCN-X	4.0	7.8	1.0	0.1	0.3	4.0	12.4	0.3

Table 4.2: *Characteristic parameters for blood and the blood analog fluid. The data for blood flow are taken from Hoeks* et al. *(1995). Blood[1] and blood[2] refers to data taken from younger and older individuals, respectively. The data for end diastolic flow are used to obtain the values for V.*

this comparison, it can be seen that the shear thinning of the KSCN-X solution can be compared to blood flow for the older individuals, while the influence of viscoelasticity is overestimated. Based on the values of the dimensionless parameters, both viscoelasticity and shear thinning cannot be neglected.

The velocity components were measured according to the experimental grid, given in figure 4.2. Starting at the inlet of the curved section, seven planes were measured from $\theta = 0°$ to 90° with increments of 15°. During 16 flow cycles, the velocity was measured at each location with an effective data rate of about 30 *Hz*. Comparison of the results of the velocity measurements to the numerical data was facilitated by dividing each flow cycle into 64 intervals and averaging the velocities in these intervals. The experimental error in the determination of the velocity vector originates from several sources: errors in the positioning of the measuring volume, variation in the flow pulse, and noise on the velocity signal. These errors account for an error in the measured velocity of less than 3 % of the mean axial velocity (see also Rindt *et al.*, 1991). Another source of inaccuracy of the velocity measurement is due to the presence of a velocity gradient in the measuring volume. Generally, this error is less than 2 %, but at locations with steep velocity gradients the error can increase to 8 % of the mean axial velocity.

4.4   Numerical methods

4.4.1   Newtonian fluid

The numerical modeling of incompressible and isothermal flow of a (generalized) Newtonian fluid requires the solution of the impulse or Navier-Stokes equations and the continuity equation:

$$\begin{cases} \rho\dot{\mathbf{v}} + \rho(\mathbf{v}\cdot\nabla)\mathbf{v} - \nabla\cdot\boldsymbol{\sigma} = \mathbf{f} \\ \\ \nabla\cdot\mathbf{v} = 0 \end{cases} \tag{4.7}$$

where $\mathbf{v}$ is the velocity vector, $\boldsymbol{\sigma}$ the Cauchy stress tensor, $\mathbf{f}$ the body force per unit mass, ∇ the gradient operator and $\dot{\mathbf{v}}$ is the time derivative $\frac{\partial \mathbf{v}}{\partial t}$. A constitutive equation is required to couple the Cauchy stress to the rate of deformation and/or the deformation of the fluid. For a Newtonian fluid with a constant dynamic viscosity η, the Cauchy stress tensor can be written as:

$$\boldsymbol{\sigma} = -p\mathbf{I} + 2\eta\mathbf{D} \tag{4.8}$$

$$\mathbf{D} = \frac{1}{2}[\nabla\mathbf{v} + (\nabla\mathbf{v})^T] \tag{4.9}$$

where p is the pressure and $\mathbf{D}$ the rate of deformation tensor. Substitution of equations (4.8) and (4.9) in the Navier-Stokes equations, followed by a discretization, using Galerkin's finite element method (e.g. Cuvelier *et al.*, 1986), leads to the following set of non-linear differential equations:

$$\begin{cases} \mathbf{M}\dot{\tilde{\mathbf{v}}} + [\mathbf{S} + \mathbf{N}(\tilde{\mathbf{v}})]\tilde{\mathbf{v}} + \mathbf{L}^T\tilde{\mathbf{p}} = \tilde{\mathbf{f}} \\ \\ \mathbf{L}\tilde{\mathbf{v}} = 0 \end{cases} \tag{4.10}$$

where $\tilde{\mathbf{v}}$ and $\tilde{\mathbf{p}}$ are columns containing the unknown velocity components and pressure values in the discrete points, $\mathbf{M}$ the mass matrix, $\mathbf{S}$ the diffusion matrix, $\mathbf{N}(\tilde{\mathbf{v}})$ the non-linear convection matrix and $\mathbf{L}$ the divergence matrix. The column $\tilde{\mathbf{f}}$ contains the body and boundary forces. The time derivative was approximated by applying the Crank-Nicholson discretization scheme. The convective term was linearized using the Newton-Raphson method. In the system of equations (4.10), the boundary conditions were included. The time dependent solution for unsteady flow in a straight tube (Womersley profiles) was prescribed as the axial inlet velocity profile. No-slip conditions served as the boundary conditions at the wall. Symmetry was prescribed for the symmetry plane and stress-free outflow conditions were used (see also figure 4.3). The set of linear differential equations was solved on the mesh depicted in figure 4.3. The Crouzeix-Raviart type elements contain 27 nodes, with a quadratic approximation for the three velocity components in each node. Both the pressure and the pressure gradient were defined in the centroïd of each element. The mesh consisted of 1084 elements and contained 10353 nodal points. The package SEPRAN (Segal, 1984) was employed to generate the mesh and to build and solve the system of equations. The equations (4.10) were solved using the integrated method (e.g.
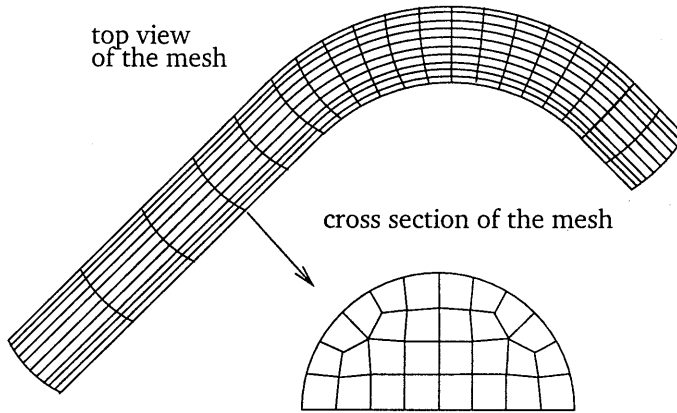
Figure 4.3: *finite element mesh*

Cuvelier *et al.*, 1986). Renumbering of the unknown quantities $\tilde{\mathbf{v}}$ and $\tilde{\mathbf{p}}$ (Segal and Vuik, 1995) was performed to avoid zero diagonal elements in the assembled matrix. The preconditoning of the assembled matrix according to a incomplete LU decomposition limited the required CPU time. A BiCGstab iterative solver was applied and the iteration process was stopped using the following criterion:

$$\frac{res^k}{res^0} \leq \epsilon \quad ; \quad \epsilon = 10^{-5} \tag{4.11}$$

with k the iteration number, and res^k and res^0 the residual at iteration k and 0 respectively. For the flow pulse, 64 time steps per period were used, and two complete periods were computed.

4.4.2 non-Newtonian fluid

In the numerical part of this study, only the shear thinning properties of the KSCN-X solution were taken into account. Since viscoelasticity was not included, the comparison of the numerical and experimental results should indicate whether viscoelasticity significantly alters the velocity distribution.

The shear rate dependent viscosity slightly altered the computational method. For the shear rate in the Carreau-Yasuda model, a scalar measure of the rate of deformation tensor was used (Macosko, 1994).

$$II_{\mathbf{D}} = tr(\mathbf{D}^2) \tag{4.12}$$
$$\dot{\gamma} = \sqrt{2II_{\mathbf{D}}} \tag{4.13}$$

The shear rate dependent Cauchy stress tensor read:

$$\sigma = -p\mathbf{I} + 2\eta(\dot{\gamma})\mathbf{D} \tag{4.14}$$

In the subsequent discretization, the diffusion tensor was non-linear:

$$\begin{cases} M\dot{\tilde{v}} + [S(\tilde{v}) + N(\tilde{v})]\tilde{v} + L^T\tilde{p} = \tilde{f} \\ \\ L\tilde{v} = 0 \end{cases} \qquad (4.15)$$

The non-linear diffusion matrix was linearized by application of the Picard method. The subsequent solution of the equations (4.15) was identical to the procedure followed for the Newtonian fluid.

4.5   Results

In figures 4.4 till 4.9, the experimental and numerical results are presented. The axial velocity distribution in the plane of symmetry $(A - A')$ and perpendicular to this plane $(B - B')$ are shown in the upper part of each figure. Furthermore, the isovelocity lines for the axial velocity distribution are presented in contour plots at plane 15, 45 and 75. At these planes, the secondary velocity distribution is given as well.

4.5.1   Newtonian (exp) vs. Newtonian (num)

end diastole (figure 4.4)

At the entrance of the curved section, the axial velocity profile was nearly parabolic. The upstream influence of the curved section caused the axial velocity distribution to be slightly skewed towards the inner bend. The secondary velocities, though being very small, were directed towards the inner bend throughout the entire cross section. At plane 15, secondary flow, originating from a balance between the centrifugal and viscous forces, was set up. The faster moving fluid in the core moved towards the outer wall, while the slower moving fluid near the side wall was propelled towards the inner wall. The axial velocity distribution was hardly influenced by the secondary flow pattern at this site. The strength of the secondary vortex increased further downstream, reaching its maximum at plane 30. The increased strength of the secondary vortex also influenced the axial velocity distribution: the locus of the peak axial velocity moved towards the outer wall, while particles with low velocity were transported to the center, taking account for lower axial velocity in the central part of the tube further downstream. From plane 45 on, the circumferential transport of the faster moving fluid took account for C-shaped axial isovelocity lines. In plane 75 and 90, the vortex developed a tail. The results at end diastole compare well to the experimental results of Bovendeerd *et al.* (1987), indicating that steady flow conditions prevail during end diastole.

A comparison between the numerical and the experimental results revealed that the numerical code predicted the measured velocity very well. Due to low data rates, the measured velocities at near wall sites were sometimes erroneous. The magnitude of the secondary flow was slightly overestimated, and the center of the vortex in the experimental results was slightly shifted towards the inner bend for planes 45 till 90, while the numerical results predicted a more central position of the vortex.

Figure 4.4: *Experimental and numerical velocity distribution at end diastole for the Newtonian fluid. The axial velocity in the symmetry plane (A − A′) and perpendicular to this plane (B − B′, top left) are presented in the two top figures. The contour plots of the axial velocity and the secondary velocities are given for plane 15, 45 and 75 in the bottom part of the figure. The time is indicated in the schematic presentation of the flow pulse (bottom left).*

peak systole (figure 4.5)

The inertia forces, taking account for the acceleration of the fluid, dominated the flow features during systole. The axial velocity field was not dominated by the secondary
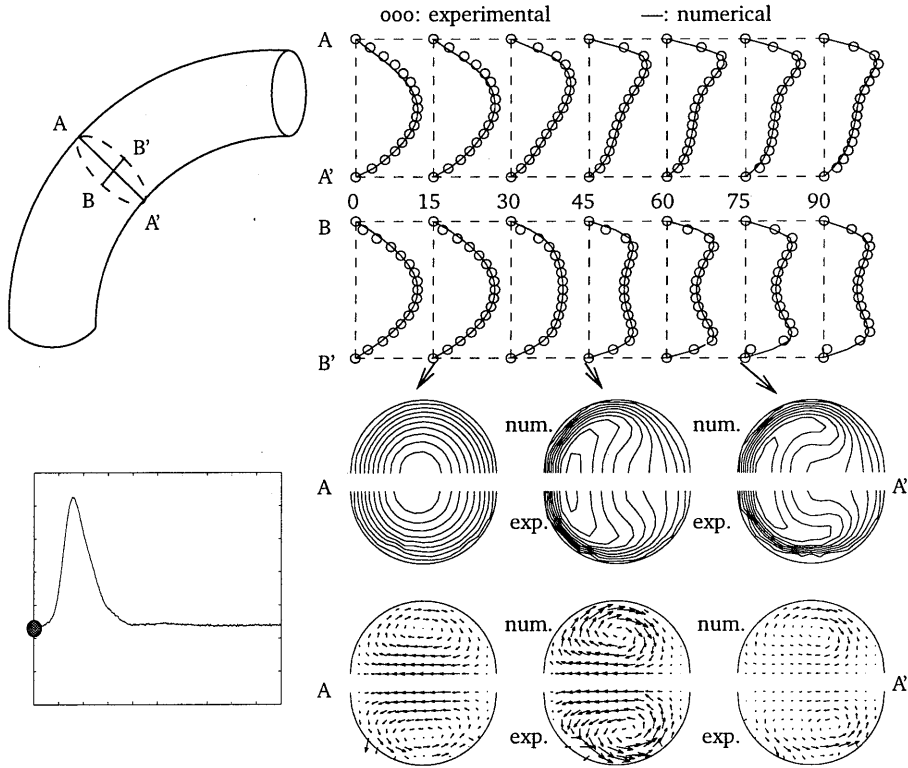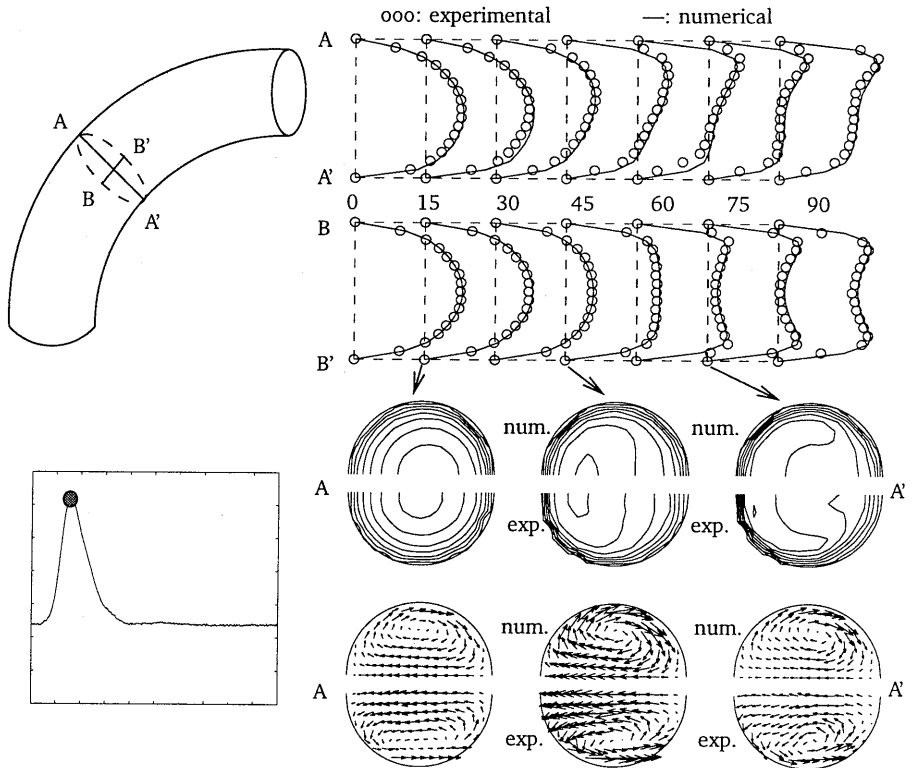

Figure 4.5: *Experimental and numerical velocity distribution at peak systole for the Newtonian fluid. The axial velocity in the symmetry plane (A − A') and perpendicular to this plane (B − B', top left) are presented in the two top figures. The contour plots of the axial velocity and the secondary velocities are given for plane 15, 45 and 75 in the bottom part of the figure. The time is indicated in the schematic presentation of the flow pulse (bottom left).*

flow, resulting in a more blunted velocity distributions. The viscous boundary layer was much thinner, resulting in steep velocity gradients near the wall. A slight shift of the peak axial velocity towards the outer bend, combined with lower velocities in the central part of the tube, was found from plane 45 on. The C-shaped isovelocity lines were much less pronounced. The secondary vortex, apart from being somewhat stronger, showed essentially the same features as during end diastole.

In peak systole, the agreement between numerical and experimental results was not as good as at end diastole. At the outer wall, the predicted velocities were somewhat

lower than the measured velocities. This discrepancy could not be attributed to the coarseness of the mesh: refinement near the wall did not improve the results. In the measured secondary velocity field, a slightly elongated vortex was be seen from plane 15 on. The numerical results indicated a more compact structure of the vortex. Furthermore, the tail of the vortex in plane 75 and 90 seemed to be more pronounced in the experimental data.

begin diastole (figure 4.6)

At begin diastole, an adverse axial pressure gradient was present to decelerate the fluid. This adverse pressure gradient was expected to influence the regions with low
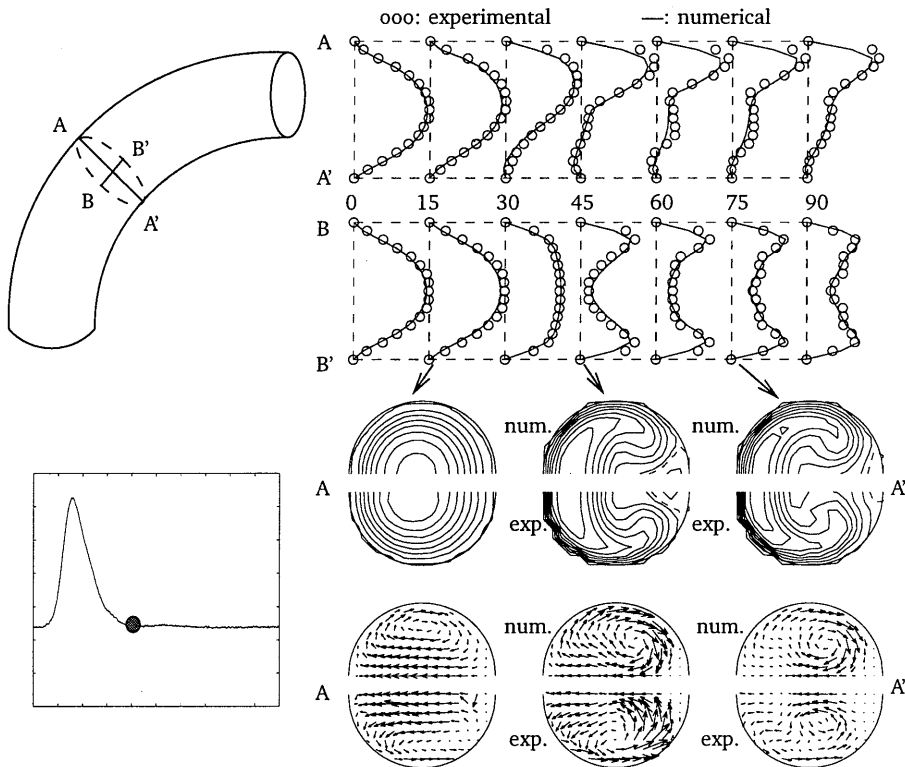
Figure 4.6: *Experimental and numerical velocity distribution at begin diastole for the Newtonian fluid. The dashed line in the contour plot denotes zero axial velocity. The axial velocity in the symmetry plane (A − A′) and perpendicular to this plane (B − B′, top left) are presented in the two top figures. The contour plots of the axial velocity and the secondary velocities are given for plane 15, 45 and 75 in the bottom part of the figure. The time is indicated in the schematic presentation of the flow pulse (bottom left).*

velocity. At the entrance of the curved tube, the velocity at near wall sites was lower than at end diastole. From plane 15 on, the outward shift of the peak axial velocity was still observable, and flow reversal near the inner bend was seen from plane 30 on. The plateau region in the central part of the tube was extended, and a free shear layer with high axial velocity gradients developed near the outer wall. The axial velocity distribution showed a second minimum in the central part of the tube, approaching zero at plane 45. The strength of the secondary vortex reached its maximum at plane 15, indicating a rapid build up of the secondary motion. The center of the vortex was displaced to the inner wall at plane 30, and a tail developed from plane 45 on. This tail developed further, being most pronounced at plane 75. Due to the rapid build up of the secondary motion, the C-shaped axial isovelocity lines developed early, and the lines with high axial velocity bent over towards the central part of the tube from plane 60 on.

Comparison with the numerical results indicated that the high velocity near the outer wall was underestimated, and that the region with flow reversal was predicted quit well. Generally, the results for the Newtonian flow showed a good agreement with the results obtained by Rindt (1989).

4.5.2   non-Newtonian (exp) vs. non-Newtonian (num)

end diastole (figure 4.7)

At the entrance of the curved section, a slightly flattened axial velocity distribution, in combination with an upstream influence of the bend, was observed for the non-Newtonian fluid. The secondary velocity distribution showed the development of a Dean vortex, resulting in a shift of the peak axial velocity towards the outer wall. Flattened axial velocity profiles were observed in the plane perpendicular to the plane of symmetry. The influence of the secondary velocity distribution on the axial flow features was not as pronounced as for the Newtonian fluid. Generally, the flow features for the non-Newtonian fluid showed the expected curved tube flow features.

The numerical code, considering the shear thinning properties of the Xanthan gum solution only and ignoring its viscoelasticity, provided a good prediction of the velocity distribution. Only the secondary velocities at plane 75 showed some deviations. This was probably due to an error in the position of the measuring volume in the experiments.

At end diastole, the steady flow features prevailed. This means that the time dependent contribution of the elastic stress tensor is not important for the velocity field at this stage in the flow pulse. The convective contribution of the elastic stress tensor, however, could influence the velocity distribution. The good agreement between experiments and numerical results indicates that the convective viscoelastic properties of the Xanthan gum solution do not influence the velocity distribution: the convective elastic stress contribution can therefore be ignored. For these flow conditions, We does not exceed its critical value.

Figure 4.7: *Experimental and numerical velocity distribution at end diastole for the non-Newtonian fluid. The axial velocity in the symmetry plane (A − A′) and per-pendicular to this plane (B − B′, top left) are presented in the two top figures. The contour plots of the axial velocity and the secondary velocities are given for plane 15, 45 and 75 in the bottom part of the figure. The time is indicated in the schematic presentation of the flow pulse (bottom left).*

peak systole (figure 4.8)

The observations at end diastole hold for peak systole as well. The overall flow features were close to the ones of the Newtonian fluid. Inertia dominated flow, with the corresponding flat axial velocity distributions and high shear rates near the wall. The comparison between the experimental and numerical results still indicated good

Figure 4.8: *Experimental and numerical velocity distribution at peak systole for the non-Newtonian fluid. The axial velocity in the symmetry plane (A − A') and perpendicular to this plane (B − B', top left) are presented in the two top figures. The contour plots of the axial velocity and the secondary velocities are given for plane 15, 45 and 75 in the bottom part of the figure. The time is indicated in the schematic presentation of the flow pulse (bottom left).*

agreement. Only at plane 75, the magnitude of the secondary velocity component directed towards the outer wall in the plane of symmetry was higher for the experimental results.

At peak systole, the time dependent contribution of the elastic stress tensor could influence the flow features. The excellent prediction of the numerical code indicates that the time dependent viscoelastic properties of the Xanthan gum solution are not

important for the velocity distribution. Not only the *We* number, but also the *De* number remain below its critical value. This means that the viscoelastic properties of the Xanthan gum solution do not have to be taken into account for the prediction of the velocity distribution in a curved tube for the used flow conditions.

begin diastole (figure 4.9)

The conclusions from the previous sections on the non-Newtonian flow, are confirmed by the results of begin diastole. The flow features were in accordance with the ex-
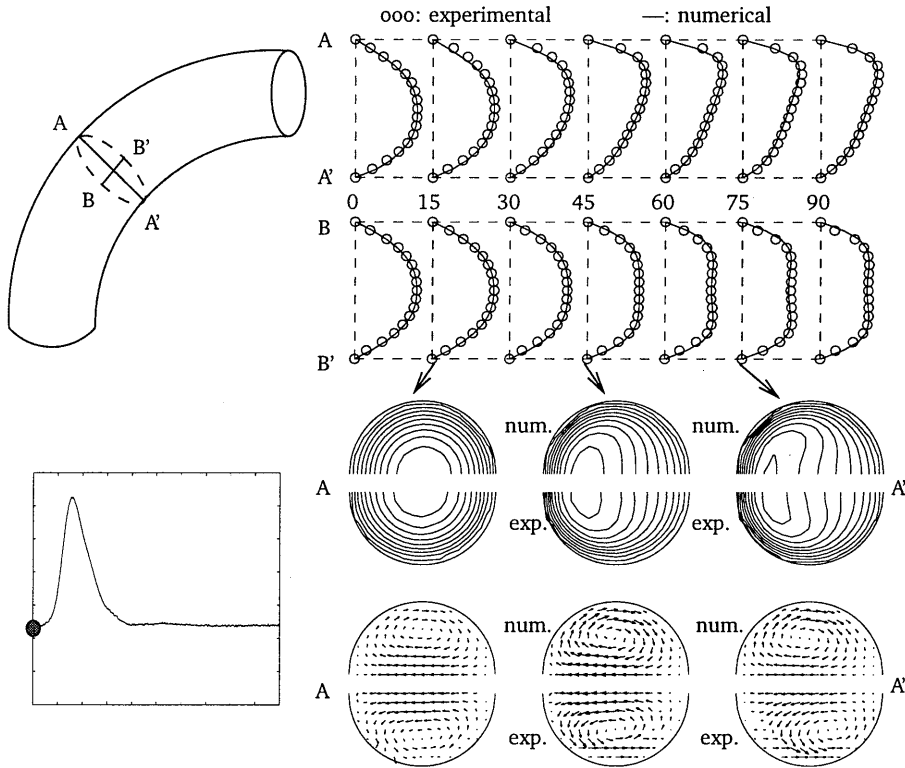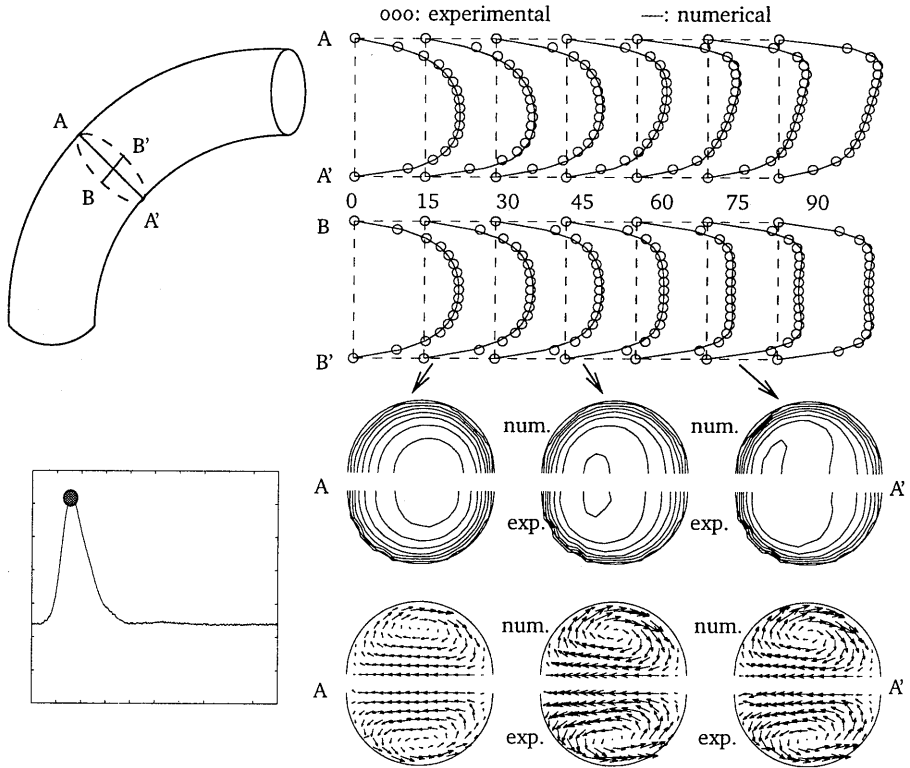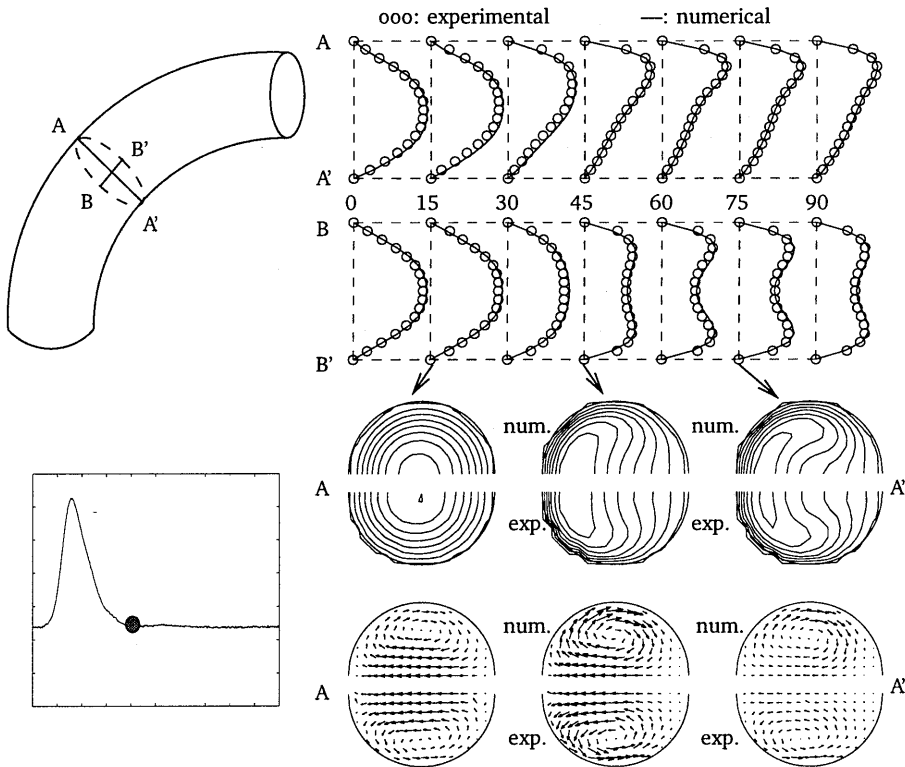

Figure 4.9: *Experimental and numerical velocity distribution at begin diastole for the non-Newtonian fluid. The axial velocity in the symmetry plane (A − A′) and perpendicular to this plane (B − B′, top left) are presented in the two top figures. The contour plots of the axial velocity and the secondary velocities are given for plane 15, 45 and 75 in the bottom part of the figure. The time is indicated in the schematic presentation of the flow pulse (bottom left).*

pected curved tube flow, and the experimental results showed good agreement with the numerical data.
The fact that the numerical code predicts the experimental results accurately indicates

that the viscoelastic properties of the experimental fluid can be ignored for determination of the velocity distribution.

4.5.3   Newtonian (num) vs. non-Newtonian (num)

From the previous discussion, it is obvious that viscoelasticity is not important for the velocity distribution: both *We* and *De* are below their critical value. The influence of shear thinning remains to be investigated. Since computations predicted the experiments well, the numerical results were used for a comparison between Newtonian and non-Newtonian flow characteristics (figure 4.10). At end diastole, the shear thin-

——— Newtonian fluid   - - - non-Newtonian fluid
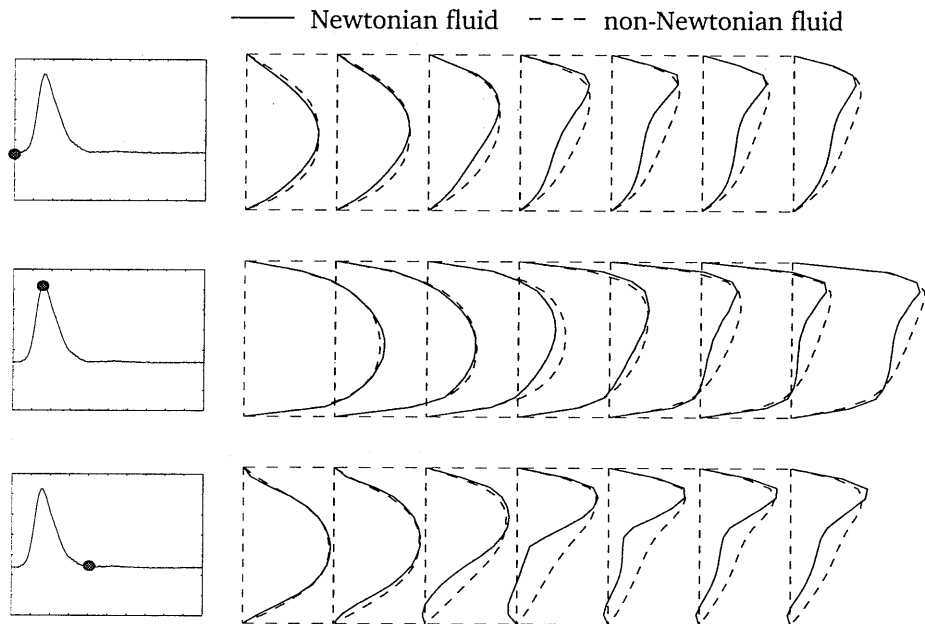
Figure 4.10: *Numerical axial velocity distribution in the plane of symmetry for the two fluids. The axial velocity in the symmetry plane (A − A') and perpendicular to this plane (B − B', top left) are presented in the two top figures. The contour plots of the axial velocity and the secondary velocities are given for plane 15, 45 and 75 in the bottom part of the figure. The time is indicated in the schematic presentation of the flow pulse (bottom left).*

ning fluid showed a flatter profile at the entrance of the tube, and the influence of the secondary velocity on the axial velocity distribution was much less pronounced: the dip in the central part of the tube, present for the Newtonian fluid from plane 45 on, was absent for the shear thinning fluid. The velocity gradients at the outer and the inner wall of the curved section were almost identical. At peak systole the same features were found. At begin diastole, the differences between the two fluids

were even more evident: the local minimum in the central part of the cross section as well as the flow reversal at the inner wall was absent for the shear thinning fluid. The slower development of the secondary flow for the non-Newtonian fluid clearly influenced the axial velocity profiles.

4.6   Implications for blood flow modeling

In the previous section, the experimental and numerical results for the unsteady flow for a Newtonian and a non-Newtonian blood analog fluid were presented. In this section, the implications of the presented results for the modeling of blood flow in large arteries are discussed.

The determination of *Re* requires a measure of the viscosity. For the Xanthan gum solution, the viscosity is a function of shear rate, and the determination of *Re* requires careful consideration. Shear rate varies throughout the cross section of the tube: high values at the outer wall and low values near the inner wall and the central part of the tube. At lower shear rates, the viscosity of the Xanthan gum solution increases, thus accounting for a more viscous behavior. The results of the previously discussed velocity distribution point into this direction. For the flow conditions in our experiments, the value of the characteristic shear rate (equation 4.5) is $39 \ s^{-1}$. A characteristic viscosity (η_c), based on the characteristic shear rate and the parameters of the Carreau-Yasuda model, yields a value of 7.8 *mPa.s*. Using this value for the viscosity, *Re* and α for the KSCN-X solution can be determined and compared to the values for blood flow (see also table 4.2). The shear thinning properties of the KSCN-X solution are assumed to be representative of blood and end diastolic flow conditions are used in table 4.3. Due to the higher density of the KSCN-X solution, *Re* and α are

fluid	fluid properties		dimensionless parameters	
	ρ	η_c	*Re*	α
	$kg.m^{-3}$	*mPa.s*	–	–
blood[1]	1080	6.7	128	3.6
blood[2]	1080	8.1	82	3.9
KSCN-X	1410	7.8	113	4.2

Table 4.3: *Dimensionless parameters for blood and KSCN-X. The data for blood are taken from Hoeks et al. (1995). Blood[1] and blood[2] refers to data taken from younger and older individuals, respectively. The data for end diastolic flow are used to obtain the values for Re.*

higher than the values for the blood flow for the older individuals. We investigated whether flow of KSCN-X solution can be described by Newtonian fluid model, using the characteristic viscosity. The experimental results of the KSCN-X solution were compared to numerical Newtonian results, based on the parameters, given in table 4.3.

The main flow features for the non-Newtonian fluid were discussed in the previous

section, so the focus will be on the comparison between the results. The results of this comparison are shown in figure 4.11 for end diastole. A remarkable agreement be-
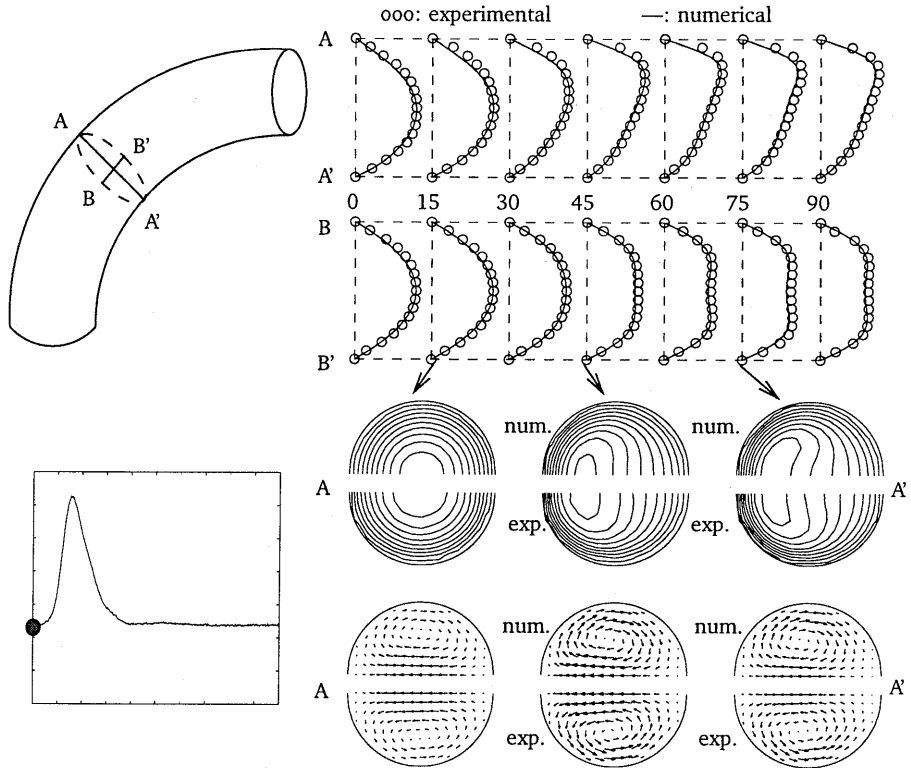
Figure 4.11: *Velocity distribution at end diastole for the non-Newtonian fluid (experimental results) and the rescaled Newtonian fluid (numerical results). The axial velocity in the symmetry plane (A − A′) and perpendicular to this plane (B − B′, top left) are presented in the two top figures. The contour plots of the axial velocity and the secondary velocities are given for plane 15, 45 and 75 in the bottom part of the figure. The time is indicated in the schematic presentation of the flow pulse (bottom left).*

tween the experimental non-Newtonian and the Newtonian numerical results, using $\eta = \eta_c$, can be observed at any location. All the flow features from the non-Newtonian flow can be described with the rescaled Newtonian fluid. The results for peak systole and begin diastole (not shown) also gave good agreement. The conclusion of this comparison is that the non-Newtonian flow of KSCN-X under the flow conditions in this study can be approximated by a Newtonian model, using $\eta = \eta_c$. The viscosity for this Newtonian model is based on the characteristic shear rate, and is about three times the high shear rate viscosity.

Takami *et al.* (1990) compared steady flow of a Newtonian and a non-Newtonian fluid. They rescaled the Newtonian flow, using the characteristic shear rate given in table 4.1. The basis of the definition they used is not clear. They found good agreement between numerical and experimental results, but differences were seen between the non-Newtonian and the Newtonian flow. Whether this discrepancy can be explained from the low characteristic shear rate they used to determine viscosity and Re for the Newtonian fluid cannot be concluded from the available information.

4.7   Discussion and conclusions

The unsteady non-Newtonian flow of a blood analog fluid in a 90° degree curved tube was studied both numerically and experimentally. The experimental results show that the non-Newtonian flow cannot be predicted with a Newtonian model with a viscosity of η_∞. The comparison with numerical results indicates that the main differences between the two flows can be attributed to the shear thinning behavior of the blood analog fluid. Despite the relatively high values of We, viscoelasticity does not significantly change the velocity field. The absence of a high normal stress differences and the relative importance of convection might explain the low impact of the viscoelastic properties of the blood analog fluid.

The shear thinning behavior of the blood analog fluid allows for linearization: the shear rate dependent viscosity can be approximated by a viscosity evaluated at the characteristic shear rate of the flow. The results of the scaled Newtonian flow field, using $\eta = \eta_c$, compared well to the non-Newtonian flow field. The definition of the characteristic shear rate is under dispute (see table 4.1). The good agreement between the non-Newtonian and rescaled Newtonian velocity field indicates that a definition of $\dot{\gamma}_c$, based on an average shear rate, as proposed in this study and in the studies of Thurston (1979) and Baaijens *et al.* (1993), is appropriate. The good agreement between the rescaled Newtonian flow field and the non-Newtonian flow field also has implications for the determination of the Re number. The value of Re for the non-Newtonian flow, based on the characteristic viscosity, is about three times lower than the Re number for the Newtonian flow.

Comparison with other studies including non-Newtonian flow in physiologically relevant flow indicates that shear rate is important. The study of Perktold *et al.* (1991) included the shear thinning of blood through a Casson model. They found only minor differences between the velocity field of the shear thinning fluid and a Newtonian fluid ($\eta = \eta_\infty$). The shear rate in their study is relatively high, and explains why they did not find any significant differences between the two flow fields. From this, it can be concluded that the influence of shear thinning on the flow field is sensitive to small variations in shear rate. Although speculative, the sensitivity to the characteristic shear rate might also help to explain the differences between the flow fields in younger and older individuals (Reneman *et al.*, 1985). Since the characteristic shear rate in the older individuals is lower, the characteristic viscosity is higher, and a more viscous behavior of blood is expected. Using these arguments, the absence of flow reversal in the internal carotid artery in the older individuals could be explained.

Two main points of interest remain: the validity of the KSCN-X solution to mimic the behavior of blood and the blood flow induced wall shear stresses. Whether or not blood can be mimicked by the KSCN-X solution can only be evaluated by direct comparison: the velocity measurements in a physiologically relevant geometry should be used to confront the two fluids. Wall shear stresses are difficult to obtain from the measured velocity distribution: the extrapolation of the velocity at near wall sites to obtain wall shear rate is rather inaccurate (Lou and Yang (1993)). Furthermore, it remains unclear whether the two-phase nature of blood has a significant influence of the near wall viscosity and thereby blood flow induced wall shear stress. An alternative approach (Gijsen *et al.*, 1997a) could be used to elucidate this matter.

Chapter 5

Wall shear rate distribution in backward-facing step flow of a red blood cell suspension [1]

5.1 Introduction

The development of atherosclerosis and the failure of vascular grafts is often associated with local hemodynamics. The predilection of atherosclerotic lesions for specific sites in the arterial tree can be correlated to low and oscillating wall shear stresses or low wall shear rates (Nerem, 1992; Caro *et al.*, 1978). The re-occlusion of vascular grafts at the distal anastomoses can also be linked to local hemodynamics (Ku and Allen, 1995). Modeling of blood flow in large arteries, including the choice of an appropriate constitutive model for blood, is therefore a relevant research topic. Clinically, ultrasound velocity measurements can be used to estimate wall shear rate *in-vivo* (Brands *et al.*, 1995). To link the development of atherosclerosis to hemodynamical variables, the accuracy of the clinical procedure to estimate wall shear rate has to be known.

Blood is a concentrated suspension of blood cells in plasma, and its non-Newtonian behavior has been demonstrated previously (Chien *et al.*, 1970; Thurston, 1979). The macroscopic viscometric properties of blood can be approximated by application of a wide range of non-linear constitutive models ranging from inelastic shear thinning models (see Cho and Kensey, 1991) to viscoelastic models, in which the time-dependent behavior of blood is included (e.g. Sharp *et al.*, 1996). Inelastic shear thinning models were used in a number of numerical investigations of blood flow

---

in large arteries (e.g. Perktold *et al.*, 1991; Baaijens *et al.*, 1993). From the exper-
imentalists point of view, a similar approach can be followed: a blood analog fluid
can be chosen such that its macroscopic viscometric properties mimic the behavior of
blood (e.g. Liepsch and Moravec, 1984; Ku and Liepsch, 1986). Gijsen *et al.* (1997a)
employed a Carreau-Yasuda model to successfully describe the behavior of a macro-
scopic blood analog fluid in various geometries under physiologically relevant flow
conditions. They found good agreement between the numerical and experimental
results, indicating that the macroscopic blood analog fluid behaved like an inelastic
shear thinning fluid. These approaches yield predictions of the velocity distribution
of blood in large arteries, but they discard the particulate nature of blood. The ability
of these numerical and physical macroscopic models to predict the blood velocity in
large arteries remains to be investigated.

In the present study, flow of a red blood cell suspension was studied in a two-
dimensional backward-facing step flow under steady flow conditions. Flow down-
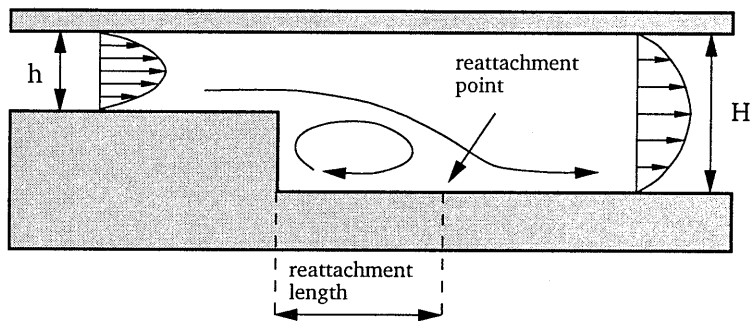
Figure 5.1: *Two-dimensional backward-facing step flow*

stream a backward-facing step contains physiologically relevant flow features: flow
reversal and a reattachment point (figure 5.1). A comparable geometry was used
to mimic flow downstream a stenosis (van de Vosse, 1987), and to investigate the
response of cultured endothelial cells to flow recirculation (Truskey *et al.*, 1995).
Furthermore, flow was studied in this geometry extensively, thus enabling validation
of the results obtained in the current study.

Armaly *et al.* (1983) investigated Newtonian flow downstream a backward-facing
step both experimentally (laser Doppler anemometry) and numerically (finite differ-
ence method) for a wide range of Reynolds numbers. The Reynolds number (Re)
was based on the height (h) of and the mean axial velocity (U) in the inlet channel
(figure 5.1). They concluded that the flow remained essentially two-dimensional up
to $Re \approx 400$ in a setup with a width to height ratio of 36. For these values of Re,
they were able to predict the measured velocity distribution and reattachment length
with two-dimensional computations. At higher values of Re, the flow showed three-
dimensional features, and the axial velocity distribution in the symmetry plane could
not be predicted with two-dimensional computations. Halmos *et al.* (1975a,b) studied
the flow of an inelastic non-Newtonian fluid in a tubular expansion. They compared

computed and measured reattachment length and the velocity field for a Newtonian and a shear thinning power law fluid. The velocity distribution was computed by means of a finite difference technique, and reattachment length and velocity field were determined through visualization of stream lines and a particle tracking technique, respectively. They were able to predict the reattachment length and velocity distribution accurately. For the power law fluid, they defined *Re* using a viscosity (η_c), based on a characteristic shear rate ($\dot{\gamma}_c$):

$$Re = \frac{\rho h U}{\eta_c} \quad ; \quad \eta_c = \eta(\dot{\gamma}_c) \quad ; \quad \dot{\gamma}_c = \frac{U}{h} \tag{5.1}$$

with ρ the density of the fluid. Application of equation (5.1) enables a comparison between the Newtonian and the power law fluid: the reattachment length for the power law fluid was only slightly longer, indicating that the velocity field of the power law fluid could be approximated by a Newtonian model, using the characteristic viscosity. Pak *et al.* (1990) used three different fluids: a Newtonian, an inelastic non-Newtonian and a viscoelastic fluid. They visualized the flow in a tubular expansion, and compared measured reattachment lengths. They confirmed the results of Halmos *et al.* (1975b), finding hardly any difference between reattachment lengths for the non-Newtonian inelastic fluid and the Newtonian fluid, using the characteristic viscosity. They observed that viscoelasticity of the fluid decreased the reattachment length considerably.

The aim of this study was to validate a macroscopic constitutive model for blood and a clinical method to determine wall shear rate *in-vivo*. Ultrasound velocimetry was applied to determine the velocity distribution in a red blood cell suspension. The viscometric properties of the suspension were used as an input to determine the parameters of an inelastic non-Newtonian constitutive model. This model was used in a finite element computation, and the resulting velocity distribution was compared to experimental results. From this comparison, the ability of the macroscopic constitutive model to predict the velocity distribution of the red blood cell suspension can be assessed. Accurate determination of wall shear rate from ultrasound velocity measurements depends on the ability of the ultrasound system to measure velocity close to the wall. The accuracy of the clinical method to measure wall shear rate can be assessed, using experimentally validated numerical results.

5.2 Methods

The velocity distribution of the red blood cell suspension in backward-facing step flow was determined by means of ultrasound velocimetry. In this section, the preparation and the properties of the red blood cell suspension, the fluid circuit and ultrasound system are described briefly. A brief account of the numerical procedure is given and finally, the experimental procedure is discussed.

5.2.1   Red blood cell suspension

The shear thinning and viscoelasticity of blood are closely related to its microscopic structure. The red blood cells determine the rheological behavior of blood: both shear thinning and viscoelasticity are related to aggregation, deformation and alignment of the red blood cells. Three liters of fresh blood were obtained through venipuncture of a pig. EDTA was added to the fresh blood to avoid coagulation. The blood was centrifuged and the plasma, blood platelets and white blood cells were removed. The red blood cells were washed three times in an isotonic TEMS buffer. The packed red blood cells were resuspended in the buffer at hematocrite of 35%. The removal of the plasma and the platelets was necessary to avoid platelet coagulation and denaturation of plasma proteins. The red blood cell suspension was characterized in viscometric flow (parallel-plate device, *RFSII, Rheometrics*). The steady shear data, together with the fit of the inelastic shear thinning Carreau-Yasuda model (e.g. Bird *et al.*, 1987), are shown in figure 5.2a. The linear viscoelastic properties are shown in figure 5.2b. The viscometric data indicate that the red blood cells do not aggregate: the steady
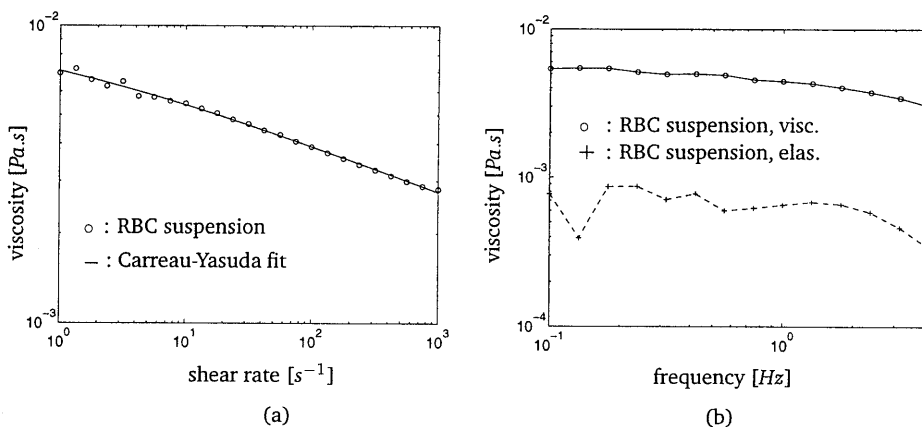
Figure 5.2: *Steady (a) and linear viscoelastic (b) properties of the red blood cell suspension (RBC suspension). The solid line in (a) denotes the Carreau-Yasuda fit.*

shear viscosity remains fairly low at low shear rates and the elastic component of the complex viscosity is low. These findings were confirmed by microscopic inspection: no aggregation was found. Since red blood cell aggregates are unlikely to occur in blood flowing in large arteries (e.g. Sharp *et al.*, 1996), the red blood cell suspension can be regarded as an appropriate blood analog fluid.

The viscosity was measured before and after the experiments and no significant differences were found, indicating that the red blood cells were not damaged during the experiments. Microscopic inspection revealed that the red blood cells retained their biconcave shape, and no significant amount of damaged red blood cells was detected.

5.2.2   Fluid circuit

The flow model, to study the flow downstream a backward-facing step, was constructed from Plexiglas (figure 5.3). The length of the channel was 500 *mm*, and the width 100 *mm*. The channel expanded from $h = 2.5$ *mm* to $H = 5$ *mm* (see also figure 5.1). The upper plate of the channel contained a slit surrounded by a container to accommodate the ultrasound probe. The slit was located in the plane of symmetry of the channel. A polycarbonate film was introduced into a chamber in the upper plate, separating container from channel. The container was filled with water, and
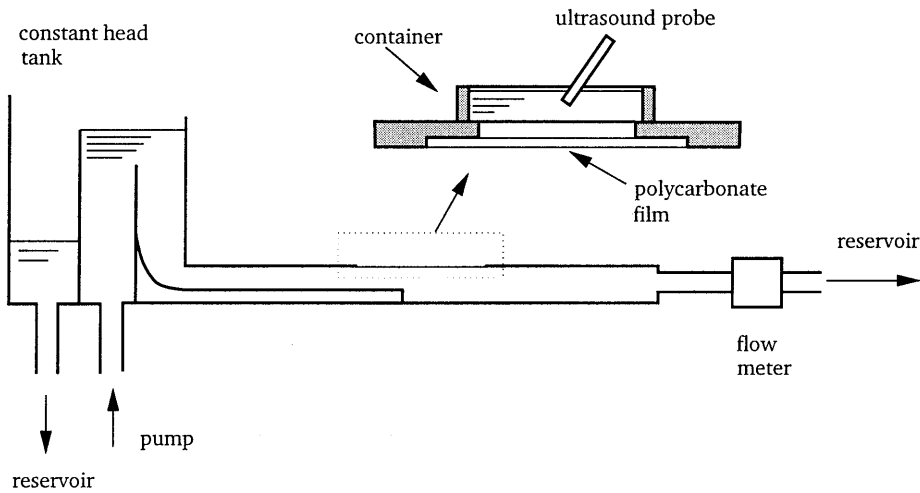
Figure 5.3: *The fluid circuit.*

the ultrasound probe was mounted to a traverse under an angle of observation of 70°. A constant head tank provided a constant pressure gradient across the flow model, thus ensuring steady flow conditions in the setup. The flow rate through the duct was adjusted by controlling the pressure gradient between the constant head tank and the reservoir and was monitored by a flowmeter (*Transflow 601, Skalar*) in the outlet tube. A centrifugal pump (*Biopump BP-80, Medtronics*) was applied to circulate the red blood cell suspension. An arterial filter was employed to remove air bubbles and red cell aggregates from the suspension.

5.2.3   Ultrasound velocimetry

The details of the ultrasound echo system were described by Brands *et al.* (1995). The three main constituents of the system were the ultrasound transmitter and receiver, the data acquisition system (DAS), and a personal computer with dedicated software for signal processing. The echo system was operated in the pulsed Doppler mode with a pulse repetition frequency (PRF) of 1 *KHz*. The carrier frequency of

the ultrasound wave was 5 *MHz* and pulse trains of 2 periods were transmitted. The reflected and scattered radio frequency (RF) signals were sampled with a frequency of 20 *MHz* during 4 seconds. The RF-signals were stored in the so-called RF-matrix, containing the RF signals in time and depth. The RF-matrix, the basic object for signal processing, was transferred to the PC. In the post-processing, the RF-matrix was divided into half-overlapping estimation windows. In this configuration, the ultrasound system measured velocity along the line of observation with a spatial resolution of 150 μm and a temporal resolution of 10 *ms*. The diameter of the ultrasound beam was approximately 1 *mm*. The reflections from the polycarbonate film and bottom wall served as a window for the RF signal. Within this window, the RF signal was averaged over 600 *ms* to improve the signal-to-noise ratio. A sixth order high pass filter with a cut-off frequency of 5 *Hz* was employed to eliminate the reflections from the walls. A mean frequency estimator, based on analytic radio frequent domain signals, was applied to determine the velocity distribution (Brands *et al.*, 1997).

5.2.4   Numerical methods

The numerical modeling of steady, incompressible and isothermal flow of a Newtonian fluid requires the solution of the Navier-Stokes equations. These equations were
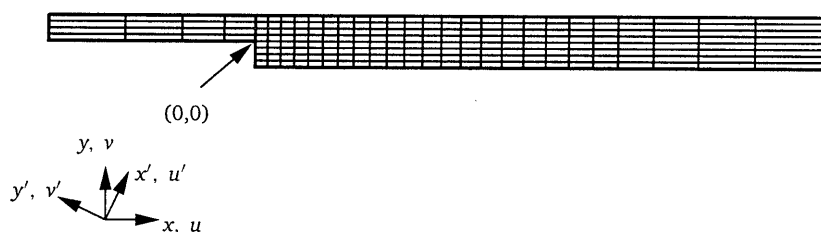
Figure 5.4: *Schematic presentation of the mesh for the fluid part. In the actual computations, four times as many elements were used. The coordinate system and the corresponding velocity components are given as well.*

discretized, following Galerkin's finite element method (e.g. Cuvelier *et al.*, 1986). The convective term was linearized using a Newton-Raphson method. The pressure was approximated by a penalty function with penalty parameter equal to 10^{-6}, ensuring that the divergence of the velocity field was of order 10^{-6}. A parabolic velocity profile was prescribed at the inlet. No-slip conditions served as the boundary conditions at the wall and stress-free outflow was used. The equations were solved on a 2-dimensional mesh (figure 5.4). The Crouzeix-Raviart type elements contained 9 nodes, with a biquadratic approximation for the two velocity components. Both the

pressure and the pressure gradient were defined at the centroïd of each element. The package SEPRAN (Segal, 1984) was employed to generate the mesh and to build and solve the system of equations.

The velocity distribution was computed for two different constitutive equations: an inelastic non-Newtonian model and a Newtonian model, using a characteristic viscosity. The shear thinning properties of the red blood cell suspension were taken into account by employing the Carreau-Yasuda model:

$$\frac{\eta - \eta_\infty}{\eta_0 - \eta_\infty} = [1 + (\lambda\dot\gamma)^a]^{\frac{n-1}{a}} \tag{5.2}$$

The Carreau-Yasuda model was fitted to the experimental data (solid line in figure 5.2), resulting in the following set of parameters:

$$\eta_0 = 12 \ mPa.s \ ; \ \eta_\infty = 1.0 \ mPa.s \ ; \ a = 0.222 \ ; \ n = 0.681 \ ; \ \lambda = 0.086 \ s \tag{5.3}$$

The non-linear viscous term, introduced by the shear rate dependent viscosity, was linearized by application of the Picard method. The viscoelastic properties of the red blood cell suspension were not accounted for. For the Newtonian model, the characteristic shear rate was determined following equation (5.1), and the parameters of the Carreau-Yasuda model were used to determine the characteristic viscosity.

5.2.5 Experimental procedure and error estimates

The velocity distribution was measured for a flow rate of $Q = 15 \ ml/s$, corresponding to an average velocity in the inlet channel of $U = 60 \ mm/s$. The velocity was measured at 3 positions in the inlet channel and in the outlet channel. Downstream of the step, measurements were taken at axial coordinates $x = 2 \ mm$ to $x = 20 \ mm$ with increments of $1 \ mm$ (for the coordinate system, see figure 5.4). The axial coordinate of the measurement sites is defined as the intersection of the ultrasound beam with the lower wall of the channel.

The estimated velocity from the ultrasound data is a projection of the velocity vector on the line of observation. The axial velocity was obtained by dividing the estimated velocity by the cosine of the angle of observation. The numerical data were treated in the same way: the components of the velocity vector were projected on the line of observation and divided by the cosine of the angle of observation. This procedure enabled a comparison of the experimental and numerical velocity distribution. It has to be kept in mind though that this procedure yields the axial velocity only in absence of axial velocity gradients. Not only the velocities, but also the shear rates were compared. The shear rates were extracted from the experimental data by finite difference of the estimated velocity (for the coordinate system, see figure 5.4):

$$\dot\gamma_{usd} = \frac{\Delta u'}{\Delta x'} \tag{5.4}$$

The numerical data were subjected to the same procedure.

Determination of the absolute value of the velocity is sensitive to the angle of observation: a deviation of the angle of 3% may lead to differences of the absolute value

of the velocity of about 25%. Since the angle could not be determined accurately, one scaling factor was used for the measured velocity. The scaling factor was determined by comparing the measured maximum velocities to the computed maximum velocities in the inlet and outlet section. This scaling procedure eliminates systematic errors caused by inaccuracies in determining the angle of observation and estimating the speed of sound in the red blood cell suspension. Another systematic error occurs in the vicinity of the wall. Due to the dimensions of the measuring volume, both fluid and wall will attribute to the reflected signal if the center of the measuring volume is close to the wall (partial volume effect). In the setup used, this distance is approximately $330 \mu m$. The reflections from the wall are suppressed by high-pass filtering. As a consequence, the estimated velocity will be biased towards a higher value at near-wall sites. (Hoeks *et al.*, 1993)), inaccuracies of axial positioning of the ultrasound probe, and inaccuracy of the flowmeter. These error sources were estimated to add up to 5% of the mean axial velocity.

5.3   Results

5.3.1   Numerical results

The numerical results were validated by exploring the dimensionless location of the reattachment point (figure 5.1) as a function of *Re* for a Newtonian fluid model and the Carreau-Yasuda model. For the non-Newtonian fluid, equation (5.1) was used to determine characteristic shear rate, viscosity and *Re*. In figure 5.5, the results for the two fluid models are compared with the measurements of Armaly *et al.* (1983) and the empirical relationship for tubular expansion, given by Ward-Smith (1980). The results indicate that the numerical results for the Newtonian fluid agree well with the values given in literature. For the non-Newtonian fluid, the reattachment length is predicted quite accurately by employing *Re*, based on a characteristic viscosity. At higher values of *Re*, the reattachment length is slightly longer for the non-Newtonian fluid. These findings indicate that previously reported results of Halmos *et al.* (1975b) and Pak *et al.* (1990) on inelastic non-Newtonian fluid flow in a tubular expansion also hold for backward-facing step flow.

The accurate prediction of reattachment length indicates that the velocity distribution in backward-facing step flow of an inelastic non-Newtonian fluid can be approximated by a Newtonian model, using a characteristic viscosity. Using equation (5.1) and $Q = 15 \; ml/s$, the characteristic viscosity and *Re* can be computed:

$$\dot{\gamma}_c = 24 \; 1/s \; ; \;\; \eta_c = 4.8 * \eta_\infty \; ; \;\; Re = 32 \tag{5.5}$$

Comparison of the velocity distribution obtained with the non-Newtonian fluid model and those obtained with the Newtonian model with a characteristic viscosity reveals a good agreement (figure 5.6). Peak velocities in inlet and outlet are somewhat higher for the Newtonian model, and in the neighborhood of the reattachment point some differences are found. This can be attributed to the non-linear properties of the shear thinning fluid. From these results, it can be concluded that both the reattachment
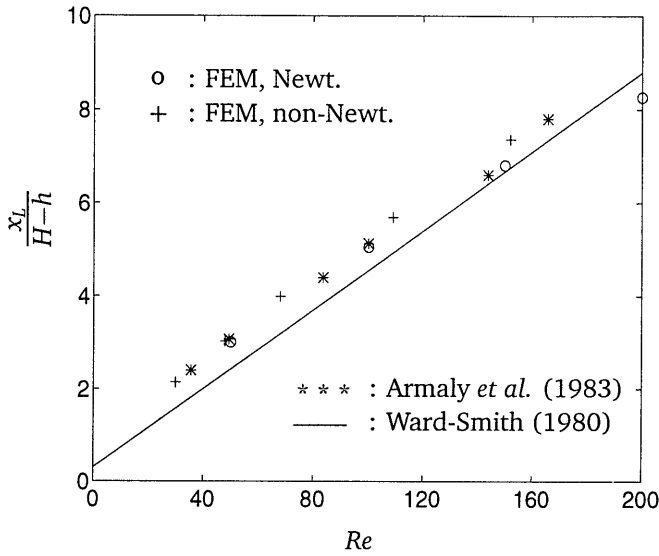
Figure 5.5: *The dimensionless position of the reattachment point for the Newtonian and the non-Newtonian fluid. The reattachment length (x_L) is made dimensionless with step height ($H - h$).*
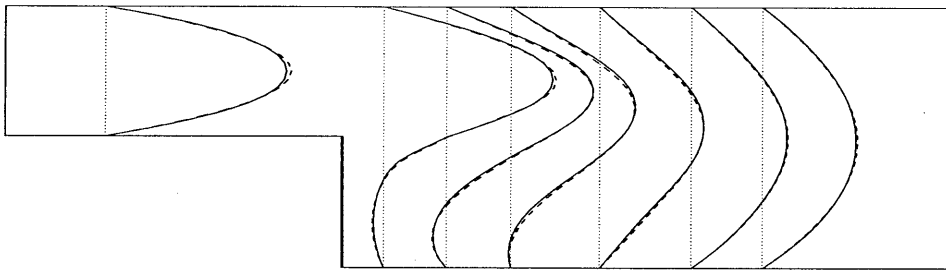

Figure 5.6: *Axial velocity distribution for the non-Newtonian (solid) and Newtonian (dashed) fluid. For the Newtonian fluid, the characteristic viscosity $\eta_c = 4.8 * \eta_\infty$ is used.*
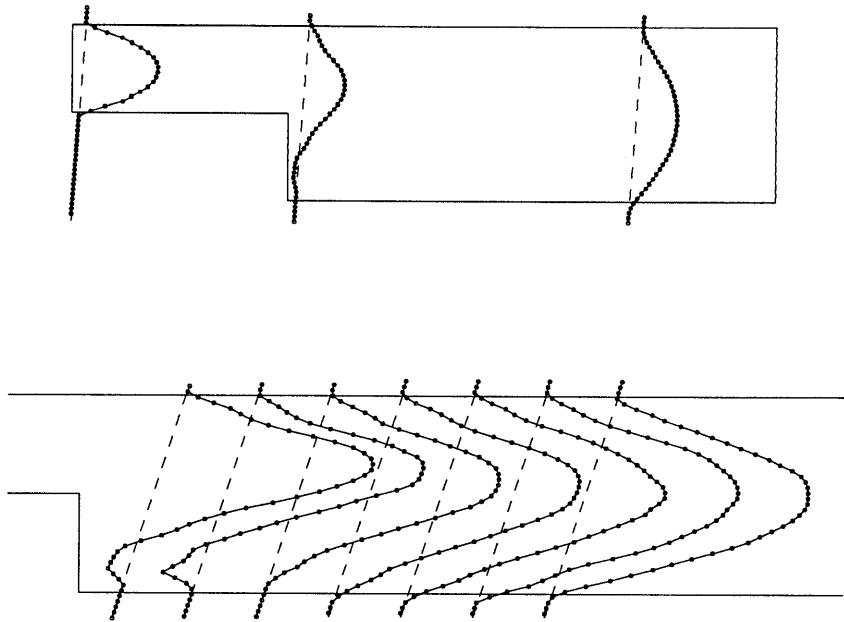
Figure 5.7: *Measured velocity profiles for Q = 15 ml/s*

length and the velocity distribution for an inelastic non-Newtonian fluid can be predicted accurately by application of a Newtonian model based on an appropriate characteristic viscosity.

5.3.2 Ultrasound velocity measurements

The measured velocity distribution for the red blood cell suspension is shown in figure 5.7. At each site, the RF-signals were measured during 4 *s*, and averaged over 600 *ms*. The velocity distribution in figure 5.7 was obtained by taking the median of the time averaged velocity estimates. In the top figure, inlet, outlet and the first velocity profile behind the step are shown. In the bottom part of the figure, a zoomed image of 7 velocity measurements behind the step is presented. The nearly parabolic velocity distribution in the inlet and the outlet channel can be clearly discerned. The shear thinning properties of the red blood cell suspension do not give rise to an appreciable flattening of the velocity profiles. Behind the step, a recirculation zone with negative axial velocities is present. The measured velocity at the wall often shows non-zero values. This can be attributed to the finite size of the measuring volume: the center of the measuring volume is in the wall, while part of the measuring volume is still in the fluid, resulting in a non-zero velocity estimate. In the region with flow reversal and near the reattachment point, the measuring volume sometimes contains only very low velocities. The high-pass filtering removes these velocities, resulting in zero velocity estimates in those areas.
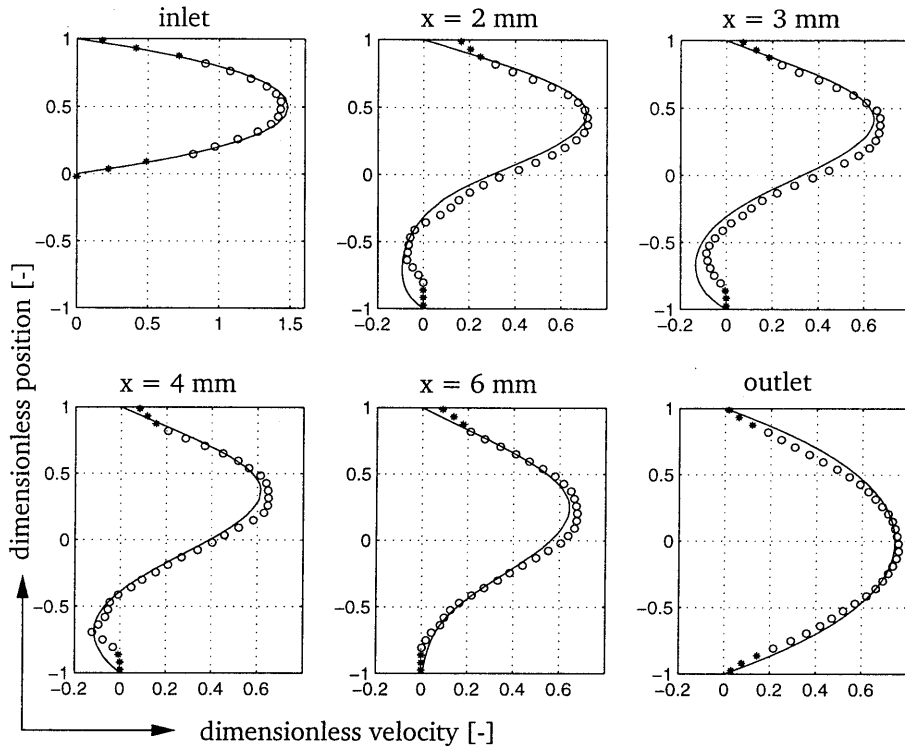
Figure 5.8: *Comparison between numerical (solid line) and experimental results (o): velocity profiles in the inlet, outlet and downstream the step. The experimental results, possibly influenced by the presence of the channel wall, are marked with an asterix. The velocity is scaled with the mean axial inlet velocity and the coordinate with the inlet height.*

5.3.3   Numerical vs. experimental results

Velocity distribution

The measured velocity distributions were compared to the computational results, using the non-Newtonian fluid model. The inlet and outlet profiles, as well as four profiles behind the step, are shown in figure 5.8. The computed velocity profiles in the inlet and outlet were used to scale the experimental results. A good agreement between measured and computed velocity distribution at those locations can therefore be expected. Behind the step, the comparison is presented for $x = 2$, 3, 4 and 6 *mm*. At these locations, good agreement between the measured and predicted velocities was found as well. The location and the size of the recirculation zone are predicted accurately. The measured negative velocities in the recirculation zone are somewhat lower than the computed values. At near-wall sites, some deviations of the
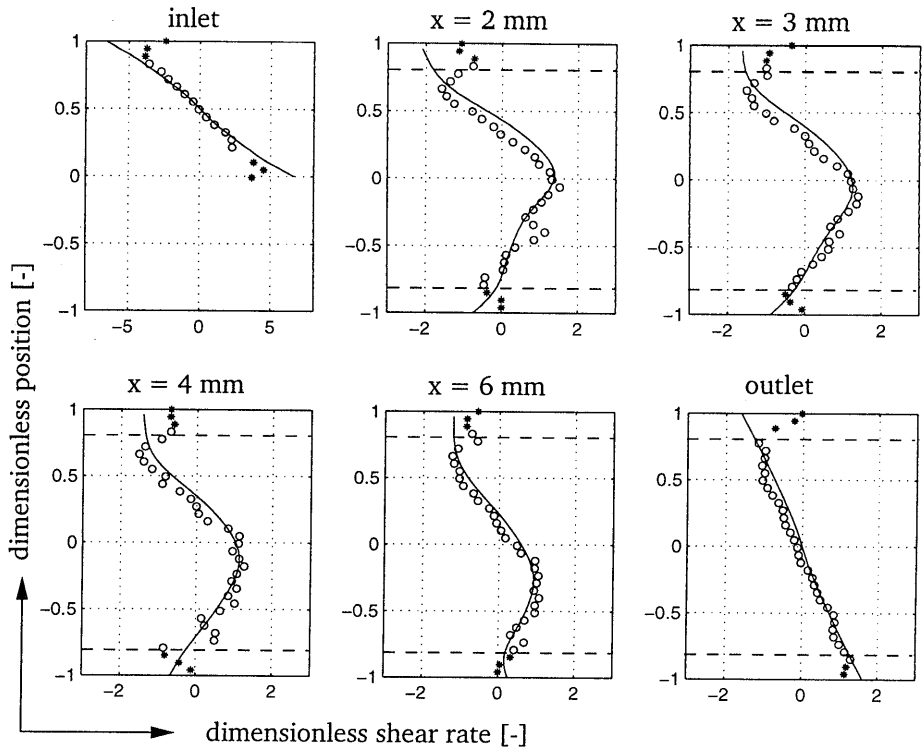
Figure 5.9: *Comparison between numerical(solid line) and experimental (o) shear rates. The experimental results, possibly influenced by the presence of the wall, are marked with an asterix. The shear rate is scaled with $\dot{\gamma}_c$ and the coordinate with the inlet height.*

measured and computed velocities were found. These differences can be attributed to the finite size of the measuring volume, and the use of the high-pass filtering. The measurement points, where an influence of the presence of the wall can be expected, are denoted by an asterix. From these observations, it can be concluded that the non-Newtonian fluid model provides a good prediction of the main features of the flow field of the red blood cell suspension. Especially in the central part of the channel, a good agreement between numerical and experimental data was obtained.

Shear rates

In figure 5.9, the measured and computed shear rates are presented. The results are given for the same locations as in figure 5.8. The shear rate estimations, possibly influenced by the presence of the wall, are denoted by an asterix. In the central part of the channel, a good agreement between the experimental and numerical results was

obtained. At near-wall sites, some deviations of predicted and measured shear rates can be observed, even for those measuring sites that are not influenced by the presence of the wall. These results confirm that the flow of the red blood cell suspension can be modeled with the inelastic non-Newtonian fluid model.

Wall shear rates

The *in-vivo* velocity measurements with ultrasound can be used to estimate wall shear rates. In the procedure, proposed by Brands *et al.* (1995), wall shear rates are de-
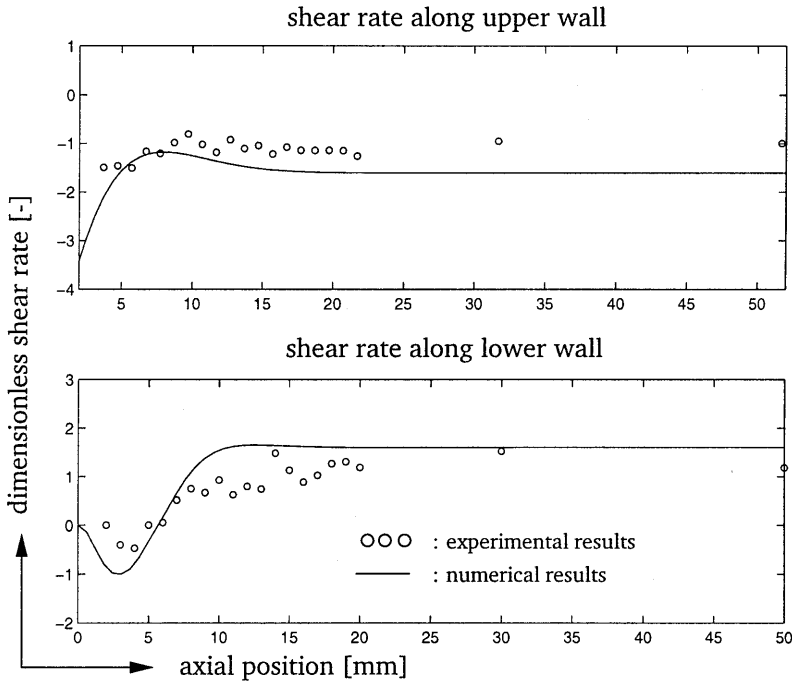
Figure 5.10: *Computed (solid line) and measured (o) wall shear rates along the upper and lower wall. The shear rate is made dimensionless with* $\dot{\gamma}_c$.

termined by computing the maximum value of the spatial derivative of the measured velocity profile in the vicinity of the wall:

$$\dot{\gamma}_w = max|\frac{\Delta u'}{\Delta x'}|_{\frac{y}{h} \to 1 \text{ or } -1} \tag{5.6}$$

In the inlet and outlet section, the highest shear rates occur *at* the wall. In ultrasound velocity measurements, the partial volume effect leads to an overestimation of velocity and underestimation of shear rate close to the wall. The maximum value of the spatial derivative of the measured velocity profile will therefore occur close to,

but not *at* the wall. The procedure to estimate wall shear rates is therefore likely to underestimate true wall shear rates. In fully developed flow, the maximum value of the spatial derivative of the velocity profile can be found at the last measuring point in the vicinity of the wall that is not influenced by the partial volume effect (see for example shear rate in the inlet and outlet channel, figure 5.9). The loci of these points are indicated by the dashed lines in figure 5.9. Measurements closer to the wall cannot be used to determine shear rate accurately due to the partial volume effect. The experimentally determined values of the shear rates along the dashed lines in figure 5.9 are compared to the computed wall shear rates (figure 5.10). As expected, the experimental shear rates underestimate the computed wall shear rates. In the region of constant wall shear rate in the outlet section ($x > 12\ mm$), the experimentally determined wall shear rates were averaged using the data along the upper and lower wall. The average value of the experimentally determined wall shear rate was approximately 25% lower than the computed wall shear rate.

5.4   Discussion and conclusions

In this study, the flow of a red blood cell suspension downstream a backward-facing step was investigated experimentally and numerically. The velocity distribution was measured by means of ultrasound velocimetry. An inelastic non-Newtonian fluid model and a Newtonian fluid model, using a viscosity based on a characteristic shear rate, were used to compute the velocity distribution. From the comparison of the numerical results of the two fluid models, it can be concluded that the velocity distribution of the inelastic non-Newtonian fluid can be approximated by the Newtonian model, using a characteristic viscosity, confirming the results of Halmos *et al.* (1975a) and Pak *et al.* (1990).

The numerical and experimental velocity and shear rate distribution were compared to evaluate the ability of the inelastic non-Newtonian fluid model to predict the flow of the red blood cell suspension. The comparison indicates that the main flow features can be described using the inelastic non-Newtonian fluid model. Both the position and the size of the recirculation zone, as well as recovery to a near parabolic velocity distribution were predicted accurately. Only at near wall sites, the experimental results are influenced by the presence of the wall, and some deviations between numerical and experimental results are found. From literature, it is known that viscoelasticity significantly influences the reattachment length (Pak *et al.*, 1990). Since the reattachment length of the red blood cell suspensions was predicted accurately with the inelastic fluid model, viscoelasticity of the suspension does not significantly influence the flow features under the flow conditions used in this study. This finding is in agreement with the results of Brookshier and Tarbell (1992). They investigated wall shear rate distribution in a curved tube by means of hot-film anemometry. Wall shear rates for a porcine red blood cell suspension and for an inelastic aqueous Xanthan-gum solution were compared, and a qualitative agreement was obtained. Assuming that the non-Newtonian model predicts the velocity and shear rate distributions accurately, it can be concluded that the experimental results can be used to

determine shear rates in the central part of the channel. The dimensions of the measuring volume influence the shear rate estimates in the vicinity of the wall: in this study, a good agreement between numerical and experimental results was obtained if the center of the measuring volume was further than 330 μm from the wall. This distance depends on the size of the measuring volume and the angle of observation. In clinical practice, the maximum value of the experimentally determined shear rates serves as an estimate of wall shear rate (Brands *et al.*, 1995). In the region with constant wall shear rate, this maximum shear rate coincides with last measuring point in the central part of the channel, that is not influenced by the partial volume effect. In this region, the clinical procedure underestimates the wall shear rate by approximately 25%. The procedure to estimate wall shear rate *in-vivo*, as proposed by Brands *et al.* (1995), can serve as a least estimate of true wall shear rate.

The red blood cell suspension, used in this study, does not exhibit any aggregation. The presence of red blood cell aggregates influences the viscoelastic properties of blood. The influence of the elastic properties of blood are therefore underestimated in this study. Red blood cell aggregates, however, are probably small in size or not present at all in blood flowing in large arteries (e.g. Sharp *et al.*, 1996). Furthermore, previous research showed that viscoelasticity did not influence the velocity distribution of a macroscopic blood analog fluid with a significant elastic component of the complex viscosity (Gijsen *et al.*, 1997a). It can therefore be assumed that the influence of viscoelasticity of whole blood under steady flow conditions can be ignored. The impact of unsteady flow on the ability of the inelastic fluid model to predict blood flow in large arteries remains to be investigated. So has the impact of the particulate nature of blood on the wall shear stress distribution. The presence of a cell-free layer at near wall sites does not have a significant impact on the velocity distribution, but could influence wall shear stress. To further investigate this matter, an alternative approach to measure wall shear stress distribution (e.g. Gijsen *et al.*, 1997b) is required.

Acknowledgements

Chapter 6

A new method to determine wall shear stress distribution [1]

6.1 Introduction

Information about the wall shear stress, exerted by a fluid flowing over a solid surface, is important to comprehend the performance of various systems. Determination of wall shear stress can be applied to optimize drag reduction in pipe flow or skin friction in aerodynamics. In a more fundamental application, wall shear stress measurements can be combined with fluid velocity measurements to evaluate the performance of constitutive models. This study focuses on a physiological application: the role of wall shear stress in the development of atherosclerosis. Atherosclerosis is a complex disease that causes a progressive occlusion of the lumen of large arteries. The predilection of atherosclerosis for specific sites in the arterial tree is believed to be related to low or oscillating wall shear stresses (Nerem, 1992). Wall shear stress is defined as the product of wall shear rate ($\dot{\gamma}_w$) and dynamic viscosity of the fluid (η). Wall shear rates in large arteries can be determined by means of ultrasound velocimetry: the velocity distribution is measured along the radius of the artery, and the wall shear rate is defined as the maximum of the spatial derivative of the axial velocity distribution. Subsequently, wall shear stress is computed by adopting a model for the viscosity of blood (e.g. Samijo et al., 1997). Validation of this non-invasive procedure to evaluate blood flow induced wall shear rate and stress in a physiologically relevant flow (e.g. flow downstream a backward-facing step) is desirable.

In the introduction, some topics from chapter 2 reappear. The blood analog fluid in this study is slighlty different from one used in chapter 3 and 4.

The clinical procedure to determine wall shear rate can be evaluated by using an alternative measuring technique, e.g. hot wire anemometry (Mann and Tarbell, 1990). A review on other available methods to measure wall shear rate is given by Hanratty and Campbell (1983). Estimation of the viscosity of concentrated suspensions, such as blood, at near wall sites poses major difficulties. The constitutive behavior of blood is governed by the suspended particles. Both in viscometric and in tube flow, the concentration distribution of the suspended particles in blood does not have to be homogeneous (Karnis *et al.*, 1966; Tangelder *et al.*, 1986). Therefore, the viscosity of blood near the wall can not be inferred directly from viscometric experiments. As a consequence, an accurate determination of wall shear stress, exerted by the flow of a suspension like blood, requires a different measurement technique.

Instead of focusing on the fluid, the response of a sensing element, attached to the wall, can be used to measure wall shear stress. In aerodynamics, wall shear stress in air flow is often measured using compact strain gauges that consist of a sensing element that can move parallel to the boundary of the wall. The deformation of the element, or the force required to keep it in its original position, is a measure of wall shear stress. A review of the available gauges is given by Winter (1977). If wall shear stress is low, as expected in blood flow in large and medium sized arteries (maximum values: $2 - 3$ *Pa*, (Giddens *et al.*, 1990), $3 - 4$ *Pa*, (Samijo *et al.*, 1997)), accurate measurement of stress is only possible if the surface of the sensing element is relatively large, thus limiting the applicability of these devices in physiologically relevant geometries. Tanner and Blows (1976) measured the thickness of an oil film in air flow and related the thickness variation to wall shear stress distribution. Although the thickness of the oil layer was measured quite accurately, the method was inapt for measuring absolute values of wall shear stress. Together with its quasi-static nature, this limits the applicability of this method. Parmar (1991) investigated the applicability of shear stress sensitive liquid crystals to determine wall shear stress. When the liquid crystals are illuminated with white light, the reflected light will change color when the crystals are subjected to a mechanical load. Although the response time of the crystals is very short, the resolution of this method (5 *Pa*) is too low for physiological applications.

In this paper an alternative method to determine the wall shear stress is presented (figure 6.1). A highly deformable gel layer is used as the sensing element. The gel
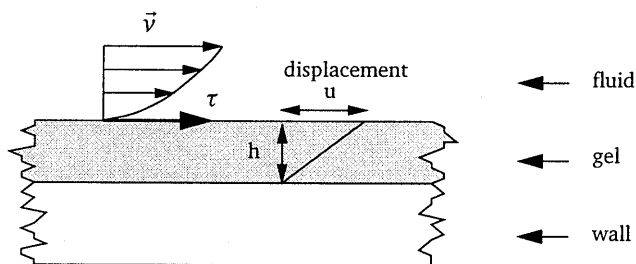

Figure 6.1: *Wall shear stress measurement through displacement of gel layer.*

layer is attached to the inner wall of a flow model. The wall shear stress, exerted by the fluid, deforms the gel layer slightly. The small deformation of the gel layer can be measured accurately by means of speckle pattern interferometry (SPI). Through the known properties of the gel, wall shear stress (τ_w) can be inferred from the deformation of the gel layer:

$$\tau_w = \eta \dot{\gamma}_w = G(\frac{du}{dh}) \approx \frac{G}{h} u \tag{6.1}$$

where G is the shear modulus, h the thickness and u the displacement of the gel layer. Using this method, wall shear stress can be determined without prior knowledge of the viscosity of the fluid. In this paper, it is shown that the proposed method can be used to determine physiologically relevant wall shear stress values. This is demonstrated by assessment of wall shear stress in a rectangular duct under steady flow conditions, using water as a measuring fluid. The experimental data are compared to the analytically determined wall shear stress values. The method can also be applied to measure the influence of blood-like shear thinning behavior on wall shear stress. The experimental results for a blood analog fluid are compared to numerically determined values. If blood is used as a measuring fluid, the combination of the proposed method and clinically applied velocity measurements in a physiologically relevant geometry can be used to validate the procedure to determine wall shear stress in arteries.

6.2   Experimental methods

The feasibility of the proposed method is assessed by measuring wall shear stress in a rectangular duct. The deformation of the gel layer, attached to the inner wall of the duct, was measured by means of SPI. The principle of SPI used in this study will be explained briefly, followed by a description of the SPI apparatus, the set-up and the experimental fluids.

6.2.1   Speckle Pattern Interferometry

When a monochromatic light source illuminates a diffusive surface, the reflected light interferes and a speckle pattern is generated. In the configuration, as shown in figure 6.2, two laser beams are used to illuminate a diffusive surface, and the speckle pattern is recorded by a CCD camera. The speckle pattern can be used to measure displacements of the surface in the plane of the laser beams, perpendicular to the viewing direction of the camera (Jones and Wykes, 1989). Each laser beam generates a speckle pattern, and the two speckle patterns interfere. The intensity distribution ($I(x,y)$) on the image plane of the CCD camera, can be decomposed into the intensities of the two separate speckle patterns and an interference term:

$$I(x,y) = I_1(x,y) + I_2(x,y) + 2\sqrt{I_1(x,y)I_2(x,y)}cos(\phi(x,y)) \tag{6.2}$$

where (x,y) denotes the position vector on the image plane of the CCD camera, $I_1(x,y)$ and $I_2(x,y)$ the intensities of laser beam 1 and 2, respectively, and the third
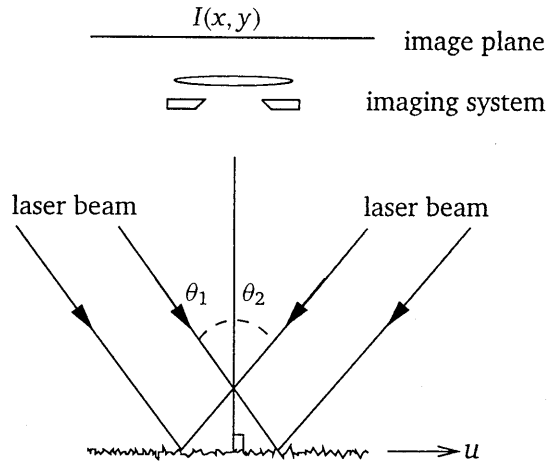
$$I(x,y)$$
_____   image plane

imaging system

laser beam   laser beam

θ_1 θ_2

$\longrightarrow u$

Figure 6.2: *In-plane displacement measurement with SPI.*

term the interference term. The contribution of the interference term depends on the phase difference ($\phi(x,y)$) between the two laser beams. The phase difference between the two laser beams depends on the surface height, leading to a random distribution of the intensity. If the surface is subjected to small deformations (deformation on the order of the wavelength of the laser light), I_1 and I_2 remain unchanged while the phase difference between the two laser beams reflected from the diffusive surface changes ($\phi(x,y) + \delta(x,y)$), and so will the contribution of the interference term. The simplest way of obtaining information about the displacement induced phase difference $\delta(x,y)$ is application of video signal subtraction. If the intensity of the recorded speckle pattern before deformation is subtracted from the intensity of the speckle pattern after deformation of the surface, the resulting intensity distribution (I_r) is:

$$I_r(x,y) = 4\sqrt{I_1(x,y)I_2(x,y)} \mid sin\frac{1}{2}(\phi(x,y) + \delta(x,y))sin\frac{1}{2}(\delta(x,y)) \mid \qquad (6.3)$$

The intensity distribution after video signal subtraction still has a random character, but it is modulated by the displacement induced phase difference. The phase difference depends on the in-plane displacement u of the surface and on the configuration of the speckle apparatus:

$$\delta(x,y) = \frac{4\pi sin(\theta)u}{\lambda} \qquad (6.4)$$

where λ is the wavelength of the laser beam and θ the angle between the laser beam and the viewing direction of the CCD camera (see also figure 6.2). The phase change will only occur due to a displacement in the plane of the laser beams, perpendicular to the viewing direction (x-direction in figure 6.3). Only one component of the displacement field of the surface can be monitored and the displacement measurements are not disturbed by out-of-plane movements.
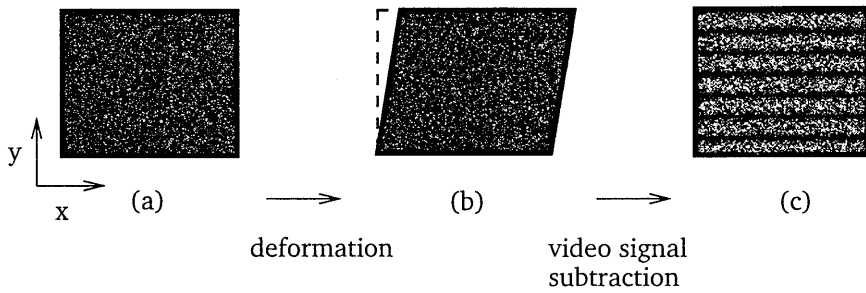
Figure 6.3: *In-plane displacement measurement on a surface subjected to shear: image of the undeformed surface (a), the deformed surface (b) and fringe pattern after video signal subtraction (c).*

In figure 6.3, the principle of SPI is demonstrated for a surface subjected to in-plane simple shear. The speckle pattern of the undeformed surface is shown in figure 6.3a. The deformation of the surface results in a linear displacement $u(y)$ (figure 6.3b). Since the displacement is a function of y only, the displacement induced phase difference between the laser beams will be a function of y as well (equation 6.4). After video signal subtraction, the phase difference δ appears as the argument in the absolute sine function for the resulting intensity (equation 6.3). Each time the phase difference is $n \cdot 2\pi$, the resulting intensity shows a local minimum, resulting in a fringe pattern (figure 6.3c).
For further reading on SPI, one is referred to Jones and Wykes (1989) and Cloud (1995).

6.2.2   Experimental setup

The SPI configuration is schematically shown in figure 6.4. A 10 *mW* He-Ne laser (*105-L, Spectra Physics*) produces a laser beam with a diameter of approximately 1 *mm* and a wavelength of 632.8 *nm*. The laser beam is expanded by the lens L and split by the beam splitter BS. The two laser beams, reflected by the adjustable mirrors M, eventually overlap on the surface, the displacement of which has to be measured. The CCD camera (*MXR, HCS*) records the generated speckle patterns. The camera is connected to a PC with a frame grabber. Image processing software (*TIM, Difa Measuring Systems*) provides the necessary tools for video signal subtraction. The position of individual components of the apparatus can be adjusted so the angle θ can be varied from 30° to 60° and the dimension of the investigated area from 2 x 2 *mm* to approximately 40 x 40 *mm*. The performance of the speckle apparatus was evaluated in a benchmark experiment. The displacement of surface, subjected to a small rotation, was measured, and a reproducibility and resolution of 50 *nm* was achieved.
The deformation of the gel layer was measured in a Plexiglas rectangular duct (height x width x length = 5 x 100 x 500 *mm*). Two constant head tanks provided a constant
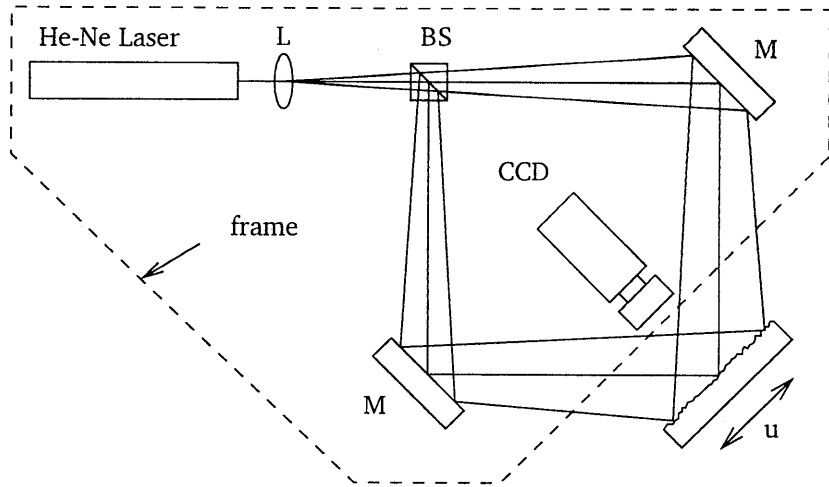
Figure 6.4: *SPI apparatus.*

pressure gradient over the flow model, thus ensuring steady flow conditions in the setup. The flow rate through the duct was adjusted by controlling the pressure gradient and was monitored by a flowmeter (*Transflow 601, Skalar*) in the outlet tube. The gel layer (height $h = 2.2\ mm$) was attached to the lower wall of the duct. Since a diffusive surface is required to perform SPI, a thin layer of titanium oxide (sl Iriodine 111, Merck) was used to cover part of the gel layer, 350 mm downstream of the entrance of the duct (figure 6.5). The diffusive patch extended from the side wall ($y = 0\ mm$) into the duct ($y = 15\ mm$). The displacement of the diffusive patch was measured to determine wall shear stress. In figure 6.5, the expected wall shear stress distribution in the rectangular duct is shown. In fully developed flow, shear stress along the bottom wall of the duct is independent of the axial position and increases from zero at the side wall to its maximum value in the central part of the duct.

Accurate determination of wall shear stress from the displacement measurements of the gel depends on detailed knowledge of the properties of the gel layer (equation 6). The gel layer was produced from a 3.5% gelatin solution in water and its properties were measured in a parallel-plate viscometer (*Rheometrics, RFSII*). Dynamic strain experiments were performed with a strain amplitude of 1% at a frequency of 1 Hz and the results indicate that the gel was essentially elastic ($G = 175\ Pa$). No further treatment of the gelatin or the Plexiglas was required to ensure proper attachment of the gelatin to the wall of the duct. The height of the gel layer was determined by carefully controlling the amount of the gelatin solution, poured into the duct. During curing of the gel layer, no change of volume was seen.
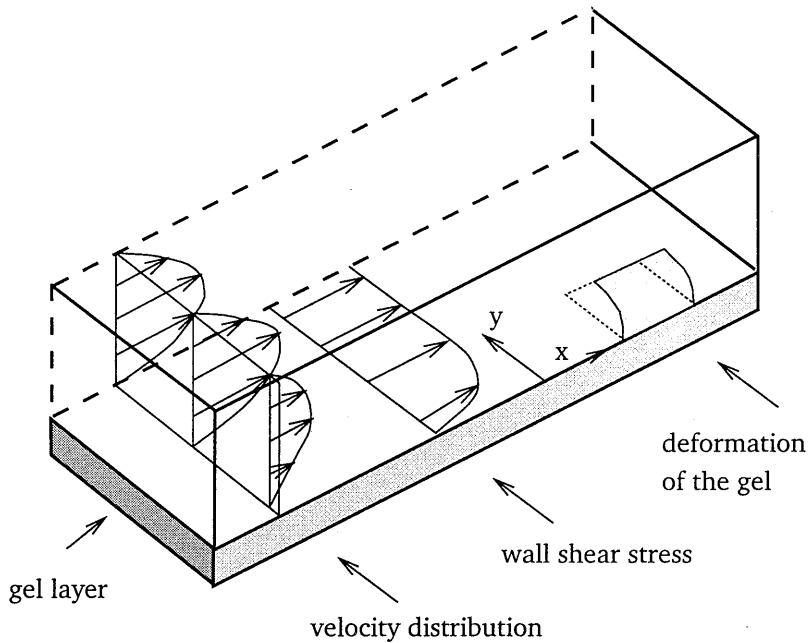
Figure 6.5: *Schematic presentation of the duct and the expected velocity, shear stress and deformation distribution.*

6.2.3 Experimental fluids

Two fluids were used in this study: a Newtonian fluid to evaluate the performance of the developed method and a non-Newtonian fluid to investigate the influence of shear thinning properties of blood on the magnitude of wall shear stress. Water was used as the Newtonian fluid and a Xanthan gum solution ($275ppm$ in water) served as non-Newtonian fluid. The steady shear viscosity of the Xanthan gum solution (figure 6.6) was measured in a parallel-plate viscometer (*Rheometrics, RFSII*). The Xanthan gum solution mimics the shear thinning behavior of blood as was shown by for example Mann and Tarbell (1990). To validate the method, the measured wall shear stress was compared to analytically (water) and numerically (Xanthan gum solution) obtained wall shear stress values. From the analytical solution of the velocity field in a rectangular duct (Ward-Smith, 1980), the velocity gradient along the gel layer was computed for the flow rates used in the experiments. The wall shear rates, multiplied by the dynamic viscosity of water, yielded the analytical wall shear stresses, which were compared to the experimental results. The shear thinning behavior of the non-Newtonian fluid was fitted with the Carreau-Yasuda model (Bird *et al.*, 1987). Using the parameters of this generalized Newtonian model, the velocity distribution, the wall shear rates and the wall shear stresses were computed with the finite element package SEPRAN (Segal, 1984). The measured wall shear stresses for the non-Newtonian fluid were compared to the computational results.
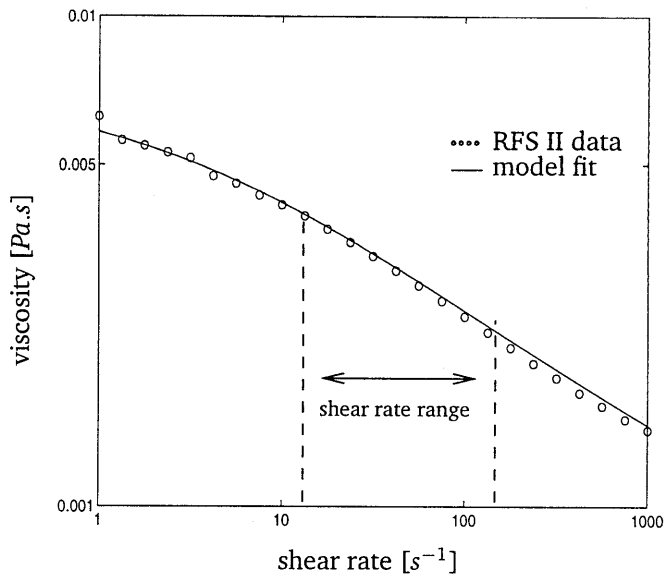
Figure 6.6: *Measured steady shear viscosity of the Xanthan gum solution (o) and the Carreau-Yasuda fit (–). The shear rate range in the experiments is indicated.*

6.3   Results

For the Newtonian fluid, the deformation of the gel layer was measured for 7 different flow rates. For each flow rate, the measured speckle pattern was subtracted from the reference speckle pattern at zero flow. Since the flow was assumed to be fully developed and the gel layer to be homogeneous, the displacement of the gel layer was expected to be constant for constant y (see also figure 6.5). The fringe distribution should therefore exhibit fringes parallel to the side wall of the duct (figure 6.7). The intensity of the measured fringe pattern was averaged over an area Δx and the resulting fringe distribution was approximated by an absolute sine function (equation 6.3). The approximation procedure resulted in an optimally fitted intensity distribution, that was converted to a displacement through equation (6.4). The procedure is visualized in figure 6.7 for a flow rate of 1.11 l/min. In the top panel, the measured fringe pattern is depicted. The averaged and fitted mean intensity are shown in the mid panel and the resulting displacement in the bottom panel. The expected fringe pattern, with the fringes parallel to the wall, can be discerned clearly. In the averaged fringe distribution, the position of the fringes can readily be seen. The fitting procedure yields a displacement distribution that is non-zero at the wall: this is caused by a displacement of the duct. This off-set of the displacement can be subtracted from the fitted displacement to obtain the displacement of the gel layer. The measured wall shear stress was inferred directly from the displacement through equation (6) and compared to the analytical wall shear stress distribution for three flow rates
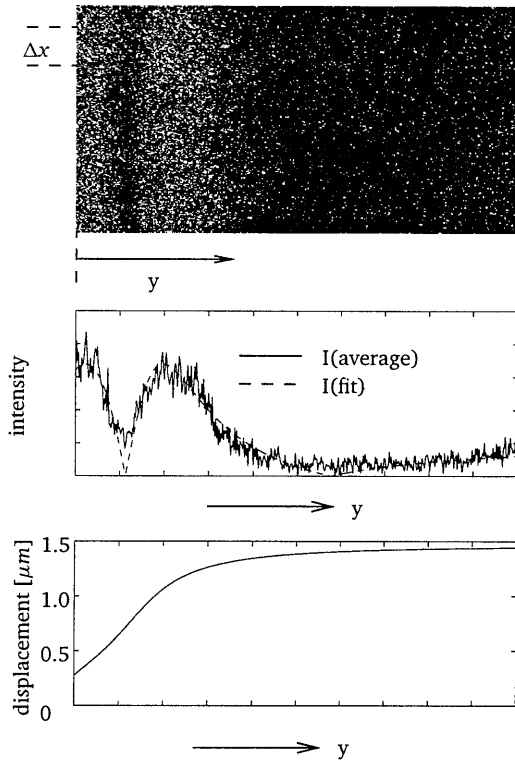
Figure 6.7: *Fringe distribution (top) at a flow rate of* 1.11 *l/min and the averaged and fitted intensity distribution (center) and the resulting displacement (bottom).*

(figure 6.8). In the region that is not affected by the presence of the side wall, the measured values of the wall shear stress show an excellent agreement with the analytical wall shear stress values. Near the side wall, the measured wall shear stress is substantially lower than the analytical wall shear stress. This can be attributed to the kinematic boundary conditions for the gel layer. The gel layer is not only attached to the bottom wall but also to the side wall: the displacement of the gel layer close to the side wall will be lower than one would expect on the basis of equation (6.1). Finally, a comparison between the analytical and the measured wall shear stress at $y = 7\ mm$ is presented in figure 6.9. The measured wall shear stress shows an almost perfect linear fit (not shown), but the slope of the fitted line is not exactly equal to one, being 4% higher. This indicates that the estimated value of G/h is too high: either the thickness of the gel layer or the shear modulus of the gel were not determined accurately or altered during the measurements.

For the non-Newtonian fluid, wall shear stress was determined for 10 flow rates, ranging from 0.1 to 1.0 l/min. The shear rate varied from 13 s^{-1} to 130 s^{-1} (see also figure 6.6). As a calibration, the gel layer displacements were also measured using water at flow rates of 0.5 and 1.0 l/min. These measurements were used to deter-
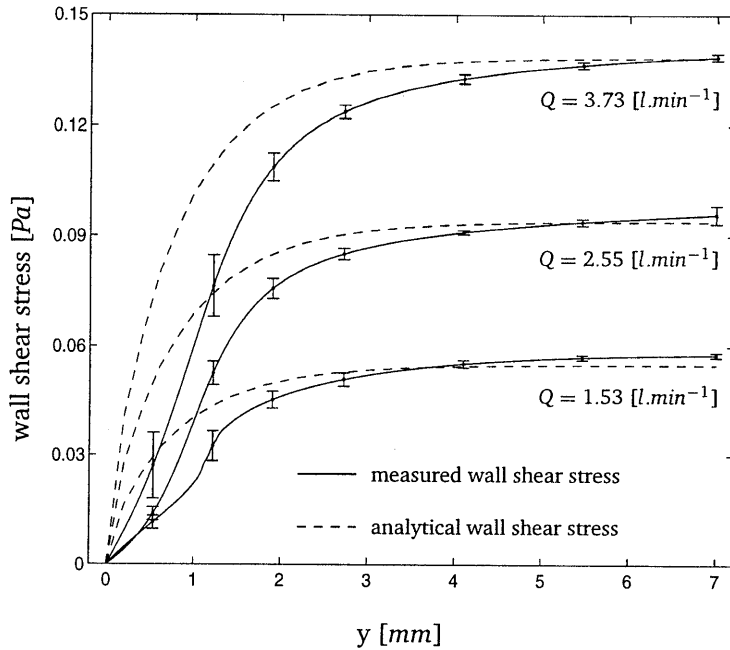
Figure 6.8: *Wall shear stress as a function of the distance from the side wall (y). A comparison between the measured and the analytical Ward-Smith (1980) wall shear stresses for three different flow rates.*

mine the value for G/h. This value was used to convert measured displacement to wall shear stress for the non-Newtonian fluid. The measured wall shear stress values for the Xanthan gum solution, scaled with the computed values for water, are shown in figure 6.10. As expected for a shear thinning fluid, the shear stress ratio for the Xanthan gum solution decreases as flow rate increases, and it compares favorably with the computed values. Only at lower flow rates, some differences can be seen between the measured and the computed values. These discrepancies can be attributed to the increased sensitivity to inaccuracy in determining flow rate and counting fringes.

6.4   Discussion and conclusions

A new method to determine wall shear stress for flow in a rectangular duct is described and was evaluated for a Newtonian and a non-Newtonian fluid. The value of the wall shear stress was inferred from the deformation of an elastic gel layer inside the flow model. The deformation of the gel layer was accurately measured by means of speckle pattern interferometry and through the properties of the gel layer, wall shear stress was computed. The measured wall shear stress far enough from the side wall showed good agreement with the computed wall shear stress for both the Newto-
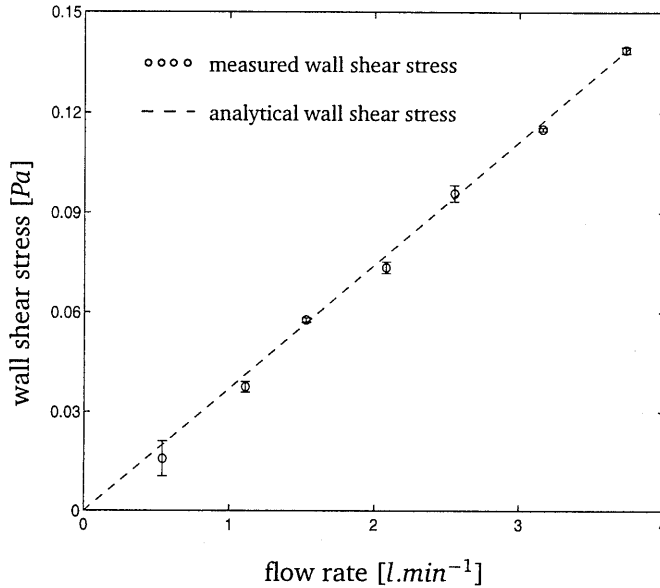
Figure 6.9: *Measured (o) and analytical (- -) wall shear stress as a function of the flow rate at y = 7 mm.*

nian and the non-Newtonian fluid. The wall shear stress measurements were accurate enough to discriminate between the two fluids. The kinematic boundary conditions for the gel layer influenced its response near the side wall of the duct. With the proposed method, wall shear stress can be determined without prior knowledge of the properties of the fluid.

Three aspects determine the accuracy of the wall shear stress measurement: the displacement measurement, the properties of the gel layer and the loading condition of the gel layer in the flow model. The displacement measurements were performed with a relatively simple speckle apparatus. The reproducibility and resolution of the speckle apparatus are satisfactory. The main drawback of the apparatus is its lack of direction-sensitivity: a positive displacement yields the same fringe pattern as a negative displacement. The properties of the gel layer, the shear modulus of the gel and the thickness of the layer, reflect the response of the gel layer to wall shear stress. Both properties must be determined accurately and remain unaltered once placed in the flow model. Depending on the chemical composition of the fluid, the gel layer may swell or part of the solid fraction of the gel may dissolve in the fluid, thus changing the properties of the gelatin. Application of the method in more complex flows or fluids should therefore be accompanied by a calibration procedure to determine the value of G/h *in-situ* as was done for the non-Newtonian fluid. The third aspect that influences the measured displacement is the loading condition of the gel layer. Equation (6.1) is only valid for a freely moving gel layer subjected to a shear load. Both the dynamic and the kinematic boundary conditions for the gel layer can alter
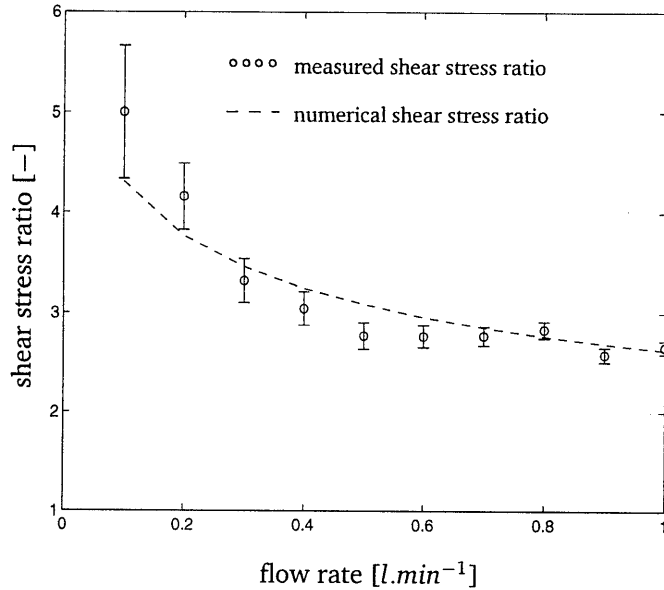
Figure 6.10: *Scaled measured wall shear stress for the Xanthan gum solution (o), compared to the numerical results (- -) as a function of the flow rate at $y = 7$ mm.*

the response of the gel layer and equation (6.1) should be regarded with caution. A gradient in wall shear stress, e.g. in the neighborhood of a stagnation point, results in a load on the gel layer that consists of both shear and tensile stress. In this situation, equation (6.1) cannot be applied. Equally important for the response of the gel layer are the kinematic boundary conditions, as can be concluded from figure 6.8. The gel layer clings to the side wall and the response of the gel layer is altered.

Extension of this method to physiological flow conditions imposes several additional requirements. Since the displacement of the gel layer in more complex flow can be both positive and negative, direction-sensitivity of the speckle apparatus is required. Several methods to include direction-sensitivity are available (Creath, 1985). These methods (e.g. phase stepping speckle interferometry) can be used to determine the exact value of the displacement induced phase difference: direction-sensitivity is included and the accuracy will improve. A second, and more important requirement, is additional knowledge of the behavior of the gel layer. In more complex flow, both the wall shear stress gradients and kinematic boundary conditions for the gel layer influence the response of the gel layer. Since the displacements of the gel layer are small and the gel is elastic, the measured displacements of the gel can be used as a boundary condition for a simple, linear elastic finite element computation to predict the behavior of the gel. Wall shear stress can then be obtained as a result from these computations. The combination of phase stepping speckle interferometry and finite element analysis of the gel layer will enable validation of the *in-vivo* procedure to determine wall shear stress in physiologically relevant flows.

<div align="right">

Chapter 7

</div>

Wall shear stress distribution in backward-facing step flow of a red blood cell suspension [1]

7.1 Introduction

The development of atherosclerosis and the failure of vascular grafts is often associated with local hemodynamics. The predilection of atherosclerotic lesions for specific sites in the arterial tree can be correlated to low and oscillating wall shear stresses or low wall shear rates (Nerem, 1992; Caro *et al.*, 1978). The re-occlusion of vascular grafts at the distal anastomoses can also be linked to locally disturbed wall shear stress patterns (Ku and Allen, 1995). From these observations, it can be concluded that the modeling of blood flow induced wall shear stress in large arteries is a relevant research topic.

Blood is a concentrated suspension of blood cells in plasma, and the non-Newtonian behavior of blood has been demonstrated previously (Chien *et al.* (1970); Thurston (1979)). The macroscopic viscometric properties of blood can be approximated by application of a wide range non-linear constitutive models, ranging from inelastic shear thinning models (see Cho and Kensey, 1991) to viscoelastic models in which time-dependent behavior of blood is included (e.g. Sharp *et al.*, 1996). These equations serve as an input for a number of numerical investigations of the blood flow in large arteries (e.g. Perktold *et al.*, 1991; Baaijens *et al.*, 1993). From the experimentalists point of view, a similar approach can be followed: a blood analog fluid can

---

[1]The contents of this chapter are submitted to *Biorheology*, under the title:

<div align="center">

Wall shear stress in backward-facing step flow of a red blood cell suspension

F.J.H. Gijsen, F.N. van de Vosse, and J.D. Janssen

</div>

The introduction, the discussion on the red blood cell suspension as well as some parts of the numerical methods in this chapter are identical to the corresponding parts in chapter 5.

be chosen with viscometric properties identical to blood (e.g. Liepsch and Moravec, 1984; Ku and Liepsch, 1986). Gijsen *et al.* (1997a) employed a Carreau-Yasuda model to successfully describe the behavior of a macroscopic blood analog fluid in various geometries under physiologically relevant flow conditions. They found a good agreement between numerical and experimental results, indicating that the macroscopic blood analog fluid behaves like an inelastic shear thinning fluid. These physical and numerical macroscopic models are used to model blood flow in large arteries, but they discard the particulate nature of blood.

Wall shear stress (τ_w) can be determined by multiplying wall shear rate ($\dot{\gamma}_w$) and dynamic viscosity (η) of the fluid. In the numerical studies, wall shear stresses are computed from the velocity field and the macroscopic constitutive equation. Wall shear rates in experimental studies are usually obtained from extrapolation of measured velocity profiles using ultrasound (e.g. Brands *et al.*, 1995) or by application of hot-film anemometry in *in-vitro* models (e.g. Brookshier and Tarbell, 1993). To compute wall shear stresses, a model is used to infer the viscosity of blood (e.g. Samijo *et al.*, 1997). The particulate nature of blood complicates the choice of an appropriate model for blood viscosity: near wall concentration distribution of red blood cells might be important for the determination of wall shear stress. An alternative approach to determine wall shear stress was presented by Gijsen *et al.* (1997b). They used the deformation of a gel layer to infer wall shear stress. Using this method, wall shear stress can be determined without having to model the near wall viscosity of blood.

The aim of this study is to determine the blood flow induced wall shear stress distribution and to investigate whether this wall shear stress distribution can be predicted by a macroscopic constitutive model for blood. The flow of a red blood cell suspension
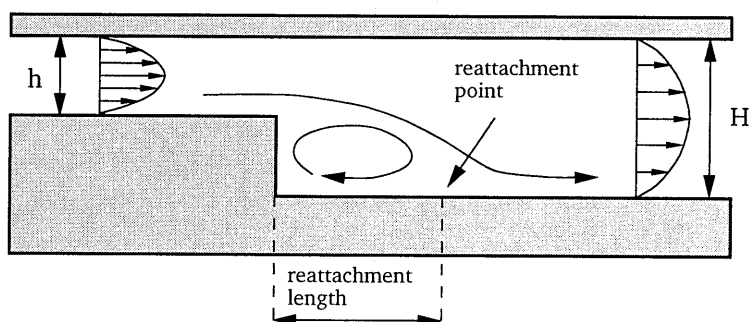
Figure 7.1: *Backward-facing step flow.*

will be studied in two-dimensional backward-facing step flow under steady flow conditions. Flow downstream a backward-facing step contains physiologically relevant flow features: a stagnation point and flow reversal. Furthermore, flow in this geometry was studied extensively, both experimentally and numerically (Halmos *et al.*, 1975a,b; Armaly *et al.*, 1983; Pak *et al.*, 1990, e.g.), thus enabling detailed validation of the results of the current study.

In a previous study, it was shown that for a red blood cell suspension the velocity distribution and shear rates in backward-facing step flow could be modeled with an inelastic non-Newtonian fluid model Gijsen *et al.* (1998). The results for the non-Newtonian fluid model were compared to a Newtonian model with a characteristic viscosity. The characteristic viscosity (η_c) was based on a characteristic shear rate ($\dot{\gamma}_c$), following the procedure of Halmos *et al.* (1975a):

$$Re_c = \frac{\rho h U}{\eta_c} \quad ; \quad \eta_c = \eta(\dot{\gamma}_c) \quad ; \quad \dot{\gamma}_c = \frac{U}{h} \tag{7.1}$$

with η the shear rate dependent dynamic viscosity of the fluid and U and h the mean velocity in and height of the inlet channel, respectively.

In this study, wall shear stress distribution downstream a backward-facing step was determined experimentally. The measured wall shear stresses were compared to numerically determined values, using the inelastic Carreau-Yasuda model and a Newtonian model, based on the characteristic viscosity.

7.2 Experimental methods

7.2.1 Procedure

The method to study wall shear stress distribution downstream a backward-facing step is based on a method proposed by Gijsen *et al.* (1997b). In that study, displacement of a gel layer was measured at the fluid-solid interface in a rectangular duct (figure 7.2). The wall shear stress was inferred directly through the properties of the
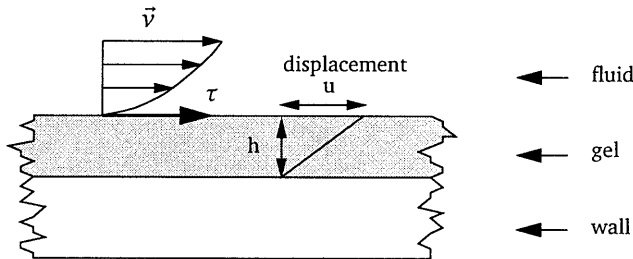
Figure 7.2: *Determination of wall shear stress through displacement of gel layer*

gel layer:

$$\tau = \eta \dot{\gamma}_w = G \cdot \left(\frac{du}{dh}\right) \approx \frac{G}{h} \cdot u \tag{7.2}$$

where G is the bulk modulus of the gel, h the height of the gel layer and u the displacement measured. In this study, the gel layer was located downstream a backward-facing step (figure 7.3). In this setup, the wall shear stress is negative in the recir-
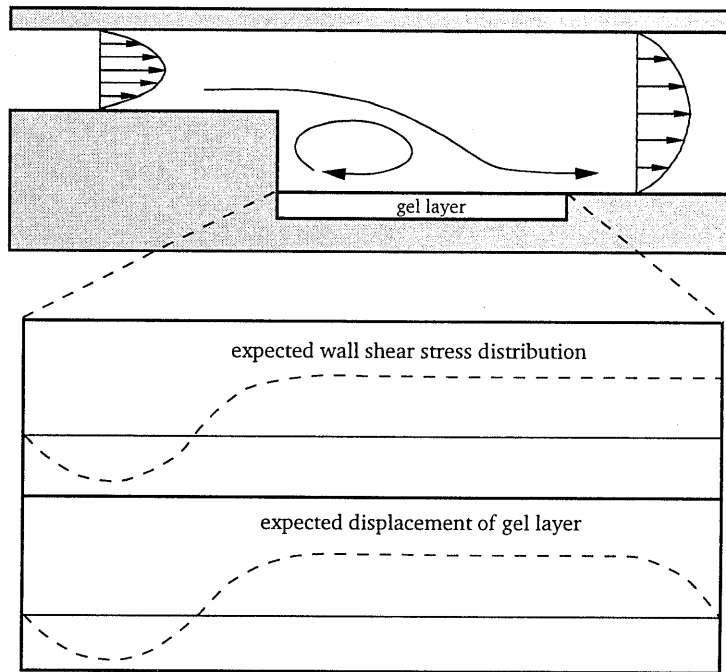
Figure 7.3: *Wall shear stress distribution and expected displacement of gel layer downstream a backward-facing step.*

culation zone, zero at the reattachment point and it attains a constant positive value further downstream. Due to the presence of a gradient in the wall shear stress and the influence of kinematic boundary conditions for the gel layer, equation (7.2) cannot be applied: a finite element computation of the deformation of the gel layer is required to convert measured displacement to wall shear stress. To be able to perform these computations, the properties of the gel layer (G and h) have to be known.

The procedure to determine the wall shear stress in backward-facing step flow of a red blood cell suspension is visualized in figure 7.4. A calibration procedure with a Newtonian fluid was used to determine the properties of the gel layer. The wall shear stress distribution was obtained from a finite element computation of the Newtonian fluid flow (*step 1*), and served as a dynamic boundary condition for the computation of the deformation of the gel layer. The displacement of the gel layer was measured by means of phase stepping speckle interferometry (PSSI), and the computed displacement was compared to the measured displacement (*step 2*). Since the behavior of the gel layer is linear in its modulus (small deformations, linear elastic behavior), computed deformation can be fitted to measured deformation and the modulus of the gel follows from this fitting procedure. The modulus of the gel served as an input to convert measured displacement to wall shear stresses (*step 3*), using a red blood cell suspension as measuring fluid. The measured wall shear stress distribution can then

Figure 7.4: *Schematic presentation of the procedure to determine the wall shear stress distribution induced by a red blood cell suspension. PSSI refers to phase stepping speckle interferometry and FEM to finite element computations. The encircled numbers are referred to as 'step' in the text.*

be compared to the computed wall shear stress distribution (*step 4*).

In the following sections, the experimental and numerical methods, required for the determination of the wall shear stress downstream the backward-facing step are discussed. Phase stepping speckle interferometry is applied to determine the displacement of the gel layer. The principle of PSSI is discussed briefly, followed by a description of the red blood cell suspension and the fluid circuit. Finally, the numerical methods are discussed.
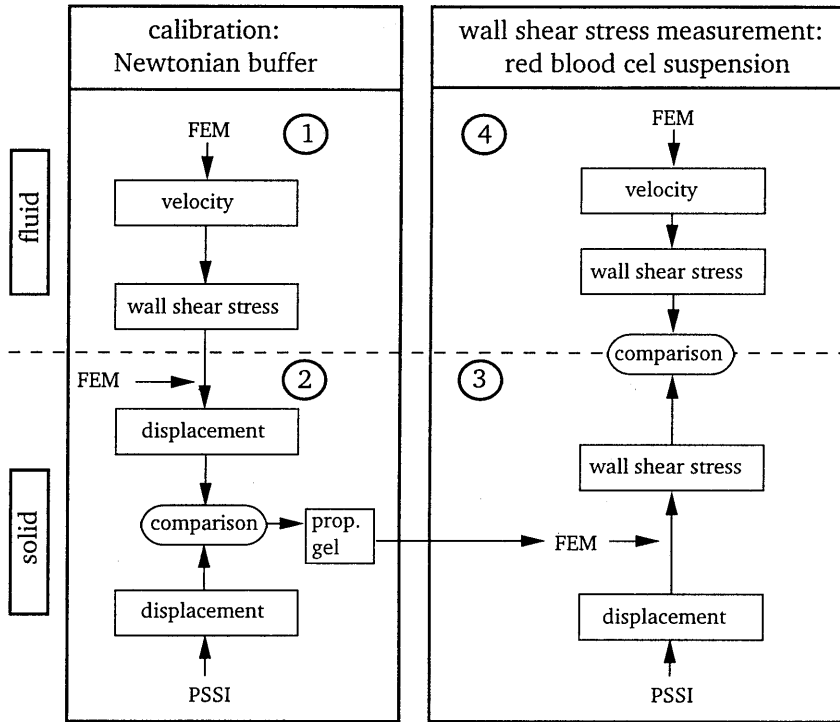
7.2.2   Phase stepping speckle interferometry

The displacement of the gel layer was determined by application of speckle pattern interferometry. The speckle pattern originates from the interference of monochromatic coherent light, reflected from a diffusive surface. If the diffusive surface is illuminated by two laser beams, and the image of the surface is recorded by a CCD camera (figure 7.5), electronic speckle pattern interferometry can be applied to measure in-plane displacements of the surface (see e.g. Jones and Wykes, 1989; Cloud, 1995). The intensity distribution from the speckle pattern on the image plane of the CCD camera can be written as:

$$I(x,y) = I_B(x,y) + I_M cos(\phi(x,y)) \tag{7.3}$$

where I_B and I_M is the background and the modulation intensity respectively and (x,y) denotes the position vector on the image plane of the CCD camera. The contribution of the modulation intensity is determined by the phase difference between the two laser beams ($\phi(x,y)$) and it has a random nature due to the roughness of the reflecting surface. In-plane displacement of the surface induces an additional phase difference ($\Delta\phi(x,y)$) between the two laser beams:

$$\Delta\phi(x,y) = \frac{2\pi}{\lambda}u(x,y)(\sin\theta_1 + \sin\theta_2) \tag{7.4}$$

where λ is the wavelength of the laser light, θ_1 and θ_2 the angle between the incident light beams and the optical axis, and $u(x,y)$ the in-plane displacement of the surface (figure 7.5). In phase stepping speckle interferometry, the phase difference $\phi(x,y)$ of each point of the speckle pattern is determined. This can be achieved by application of the five-bucket method (e.g. Cloud, 1995). Five images of the speckle pattern are recorded. These five images are separated from each other by a step in the phase difference (β) between the two laser beams. The phase difference is induced by changing the optical path length of one of the incident laser beams. The value of $\phi(x,y)$ can be determined from the five measured intensity distributions:

$$I_i(x,y) = I_B(x,y) + I_M cos(\phi(x,y) + (i-1)\beta) \tag{7.5}$$

$$\beta = \frac{\pi}{2} \quad ; \quad i = 1,2,3,4,5 \tag{7.6}$$

$$\phi(x,y) = \arctan\left[\frac{2I_2(x,y) - 2I_4(x,y)}{2I_3(x,y) - I_5(x,y) - I_1(x,y)}\right] \tag{7.7}$$

To obtain information on the displacement induced phase difference between the laser beams $\Delta\phi(x,y)$, five images are recorded before and after displacement of the
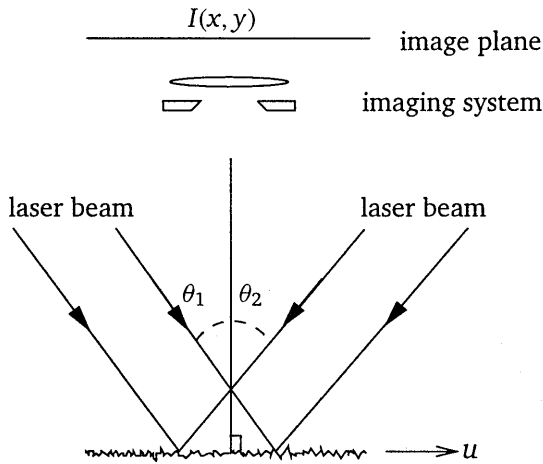
Figure 7.5: *In-plane displacement measurements with speckle interferometry.*

gel layer. Since the phase difference is known before and after deformation at each position in the image plane, the displacement induced phase difference can be determined. The displacement of the surface can be obtained through equation (7.4). Determination of the value of $\phi(x,y)$ is subjected to noise from several sources and generally some pixels have to be excluded from further processing. The nominator ($N(x,y)$) and denominator ($D(x,y)$) in equation (7.7) are used to compute a modulation intensity amplitude ($A(x,y)$):

$$A(x,y) = \sqrt{D(x,y)^2 + N(x,y)^2} \tag{7.8}$$

The modulation intensity is used as a filter: pixels with a modulation intensity below a threshold are marked as invalid and are excluded from further processing. After marking the invalid pixels, the phase maps before and after deformation are filtered and subtracted from each other. The resulting map of $\Delta\phi(x,y)$ can be determined modulo 2π. Phase unwrapping, applied to remove the modulo 2π steps, is based on a method proposed by van Haasteren (1994). The resulting phase map is converted to a displacement map, and filtered.

7.2.3   Red blood cell suspension

The shear thinning and viscoelasticity of blood are closely related to its microscopic structure. The red blood cells determine the rheological behavior of blood: both shear thinning and viscoelasticity are related to aggregation, deformation and alignment of the red blood cells. Three liters of fresh blood were obtained through venipuncture of a pig. EDTA was added to the fresh blood to avoid coagulation. The blood was centrifuged and the plasma, blood platelets and white blood cells were removed. The red blood cells were washed three times in an isotonic TEMS buffer. The packed red

blood cells were resuspended in the buffer at a hematocrite 35%. The removal of the plasma and the platelets was necessary to avoid platelet coagulation and denaturation of plasma proteins. The red blood cell suspension was characterized in viscometric flow (parallel-plate device, *RFSII, Rheometrics*). The steady shear data, together with the inelastic shear thinning Carreau-Yasuda model (e.g. Bird *et al.*, 1987), are shown in figure 7.6a. The linear viscoelastic properties are shown in figure 7.6b. The visco-
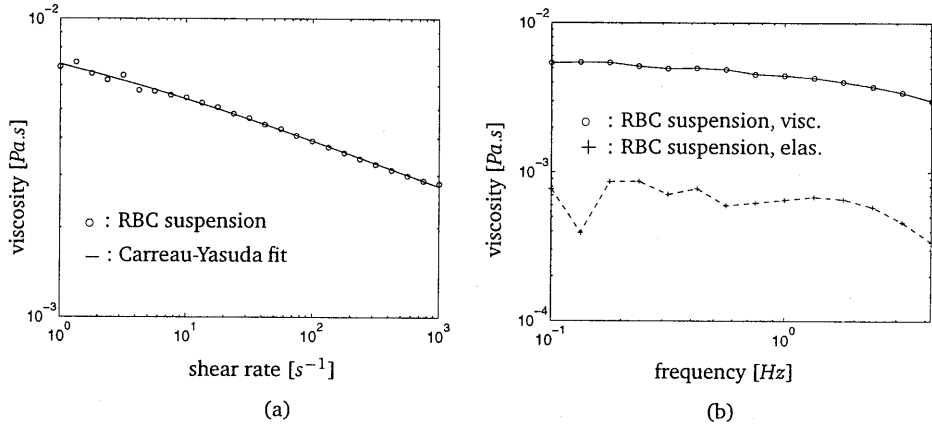
Figure 7.6: *Steady (a) and linear viscoelastic (b) properties of the red blood cell suspension (RBC suspension). The solid line in (a) denotes the Carreau-Yasuda fit.*

metric data indicate that red blood cells do not aggregate: the steady shear viscosity remains fairly low at low shear rates and the elastic component of the complex viscosity is low. These findings are confirmed by microscopic inspection: no aggregation was found.

The viscosity was measured before and after the experiments and no significant differences were found, indicating that the red blood cells were not damaged during the experiments. Microscopic inspection revealed that the red blood cells retained their biconcave shape, and no significant number of damaged red blood cells was detected.

7.2.4   Test rig

The speckle apparatus

The configuration of the speckle apparatus is shown in figure 7.7. A 10 *mW* He-Ne laser (*105-L, Spectra Physics*) produces a laser beam with a diameter of approximately 1 *mm* and a wavelength of 632.8 *nm*. The laser beam passes through a beam expander and is split by the beam splitter. The two laser beams, reflected by two adjustable mirrors and expanded by a microscope objective, overlap on the surface the displacement of which has to be measured. One of the mirrors is connected to a piezo electric transducer (*P-841, Physik Instrumente*) with an expansion of 1.501 $\mu m.V^{-1}$.

The closed loop controller of the piezo electric transducer (*P-862, Physic Instrumente*) is hooked up to a PC. The PC supplies an analog input signal for the piezo controller. The CCD camera (*1550/RS, JAI*) records the generated speckle patterns. Image processing software (*TIMWIN, Difa Measuring Systems*) is applied to record the speckle patterns. The camera is connected to a PC with a frame grabber (*Pulsar, Matrox*).
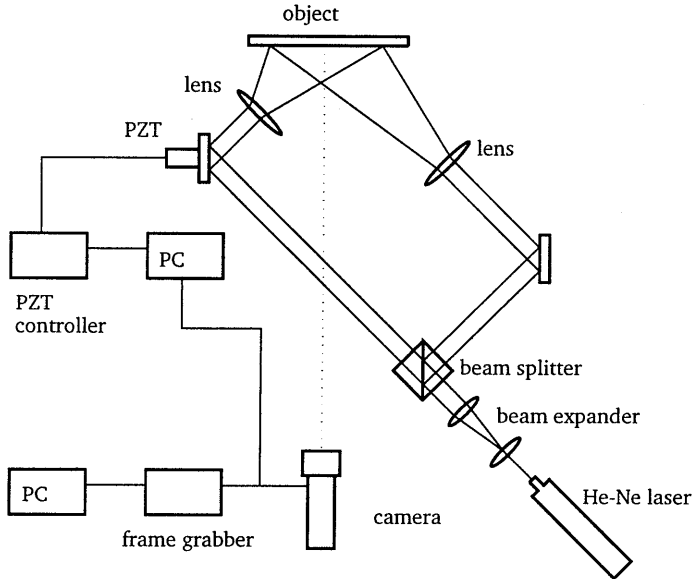
Figure 7.7: *The speckle apparatus.*

The five images, required for PSSI, are recorded consecutively: the PC generates a signal for the piezo controller, the mirror is displaced and subsequently a trigger is generated for the CCD camera. An image is recorded and the process is repeated till five images of the surface are obtained before and after deformation. The performance of the speckle apparatus was evaluated in a benchmark experiment. In the benchmark experiment, the displacement of a surface, subjected to a small rotation, was measured and reproducibility and resolution of 20 *nm* was achieved.

Fluid circuit

The flow model, to study the flow downstream a backward-facing step, was constructed of Plexiglas (length: 500 *mm*, and width: 100 *mm*). The rectangular channel expanded halfway from $h = 2.5$ *mm* to $H = 5$ *mm*. A constant head tank provided a constant pressure gradient along the flow model, thus ensuring steady flow conditions in the setup. The flow rate through the channel was adjusted by controlling the pressure gradient between the constant head tank and the reservoir and was monitored by a flow meter (*Transflow 601, Skalar*) in the outlet tube (figures 7.8). A

centrifugal pump (*Biopump BP-80, Medtronics*) was used to circulate the red blood cell suspension. A reservoir was milled in the lower plate downstream the step to
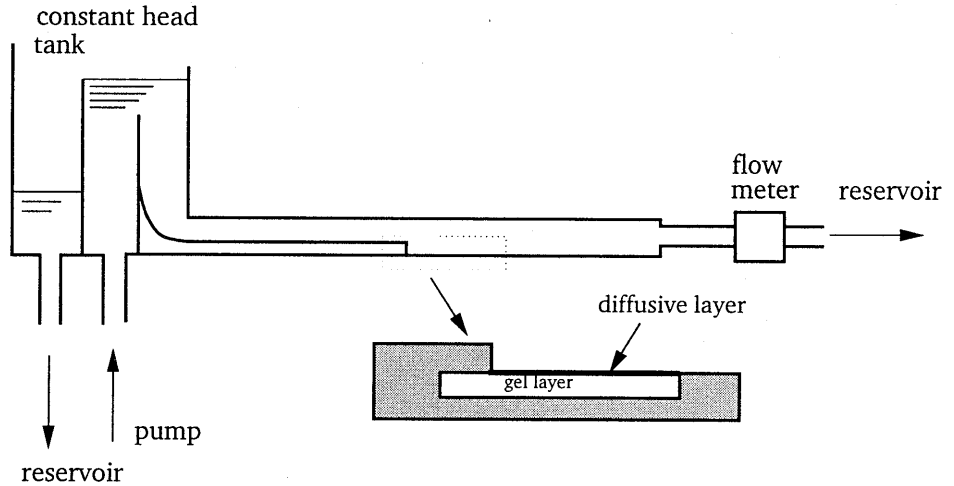
Figure 7.8: *The fluid circuit.*

accommodate the gel layer (height $h = 4.1$ *mm*, length $L_{gel} = 70$ *mm*). The reservoir extended under the step to avoid excessive reflection of the laser light from the side of the step. Since a diffusive surface is required to perform PSSI, a thin layer of titanium oxide (*Iriodine 111, Merck*) was used to cover the gel layer. The gel layer was produced from a 8.0% gelatin solution in TEMS buffer. No further treatment of the gelatin or the Plexiglas was required to ensure proper attachment of the gelatin to the wall of the duct.

7.3   Numerical methods

The numerical part of this study involves two aspects: computation of velocity distribution downstream the backward-facing step and determination of wall shear stress induced displacement of the gel layer.

7.3.1   Flow downstream a backward-facing step

The numerical modeling of steady, incompressible and isothermal fluid flow requires the solution of the Navier-Stokes equations. These equations were discretized, following Galerkin's finite element method (e.g. Cuvelier *et al.*, 1986). The convective term was linearized using a Newton-Raphson method. The pressure was approximated by a penalty function with the penalty parameter equal to 10^{-6}, ensuring that the divergence of the velocity field was of order 10^{-6}. A parabolic velocity profile was

prescribed at the inlet. No-slip served as boundary condition at the wall and stress-free outflow was used. The equations were solved on a 2 dimensional mesh (figure 7.9). The Crouzeix-Raviart type elements contained 9 nodes, with a biquadratic approximation for the two velocity components. Both the pressure and the pressure gradient were defined at the centroïd of each element. The package SEPRAN (Se-

mesh for fluid computation

step 2:
wall shear stress

step 3:
displacement

mesh for solid computation
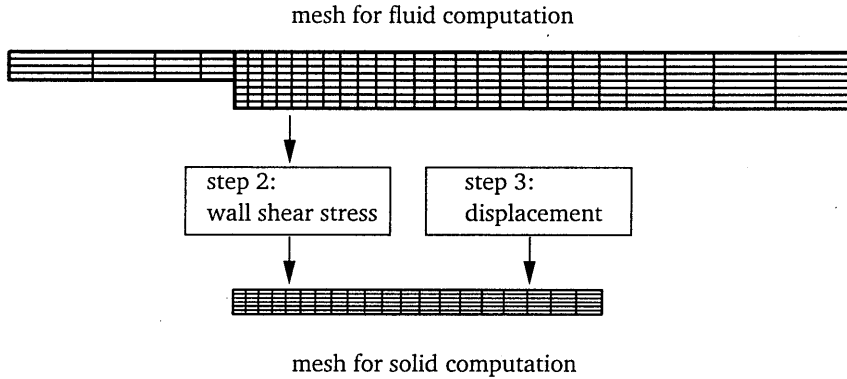
Figure 7.9: *Schematic presentation of the meshes for the fluid and the solid part. In the actual computations, four times as many elements were used. Step 2 and step 3 refer to figure 7.4.*

gal, 1984) was employed to generate the mesh and to build and solve the system of equations.

The velocity and wall shear stress distributions were computed for three different constitutive equations. A Newtonian model with $\eta = 1\ mPas$ was used for the buffer solution in the calibration procedure (figure 7.4, *step 1*). For the red blood cell suspension, an inelastic non-Newtonian model and a Newtonian model, based on a characteristic viscosity, was used (figure 7.4, *step 4*). The shear thinning properties of the red blood cell suspension were taken into account by employing the Carreau-Yasuda model:

$$\frac{\eta - \eta_\infty}{\eta_0 - \eta_\infty} = [1 + (\lambda\dot{\gamma})^a]^{\frac{n-1}{a}} \tag{7.9}$$

The Carreau-Yasuda model was fitted to the experimental data (solid line in figure 7.6), resulting in the following set of parameters:

$$\eta_0 = 12\ mPa.s\ ;\ \eta_\infty = 1.0\ mPa.s\ ;\ a = 0.222\ ;\ n = 0.681\ ;\ \lambda = 0.086\ s \tag{7.10}$$

The non-linear viscous term, introduced by the shear rate dependent viscosity, was linearized by application of the Picard method. The viscoelastic properties of the red

blood cell suspension were not accounted for. For the Newtonian model, the characteristic shear rate was determined following equation (7.1), and the parameters of the Carreau-Yasuda model were used to determine the characteristic viscosity.

7.3.2   Deformation of the gel layer

The presence of a wall shear stress gradient downstream a backward-facing step necessitates numerical modeling of of gel layer deformation. The computation of this deformation was straightforward: The gelatin was modeled as an isotropic, nearly incompressible, linear elastic material. The displacement of the gel layer was small enough to guarantee linear deformations. Plain strain was assumed, and zero displacement was prescribed at all boundaries of the gel layer, except at the fluid-solid interface. At this interface, two different boundary conditions were used (see figure 7.9). For calibration of the gel layer (figure 7.4, *step 2*) the flow induced wall shear stress of the Newtonian fluid computations served as the boundary condition. To determine red blood cell suspension induced wall shear stress (figure 7.4, *step 3*), the measured displacement served as a kinematic boundary condition. SEPRAN was also used to compute the deformation of the gel layer, thus facilitating the exchange of boundary conditions between fluid and solid computations.

7.4   Results

7.4.1   Validation of the numerical results

The wall shear stress along the gel layer, induced by the red blood cell suspension and the buffer solution, follow from the computed velocity distribution downstream the backward-facing step. The numerical results are validated by exploring the location of the reattachment point as a function of Re (figure 7.1). For the non-Newtonian fluid, equation (7.1) was used to determine Re. In figure 7.10, the results for the Newtonian and non-Newtonian fluid are compared with the measurements of Armaly *et al.* (1983) and the empirical relationship for tubular expansion, given by Ward-Smith (1980). The results indicate that the numerical results for the Newtonian fluid agree well with the values given in literature. For the non-Newtonian fluid, the reattachment length is predicted quite accurately by employing Re, based on the characteristic viscosity. At higher values of Re, the reattachment length is slightly longer. These findings indicate that previously reported results of Halmos *et al.* (1975b) and Pak *et al.* (1990) on inelastic non-Newtonian fluid flow in a tubular expansion also hold for backward-facing step flow.

The accurate prediction of reattachment length indicates that the velocity distribution in backward-facing step flow of an inelastic non-Newtonian fluid can be approximated by a Newtonian model, using a characteristic viscosity.
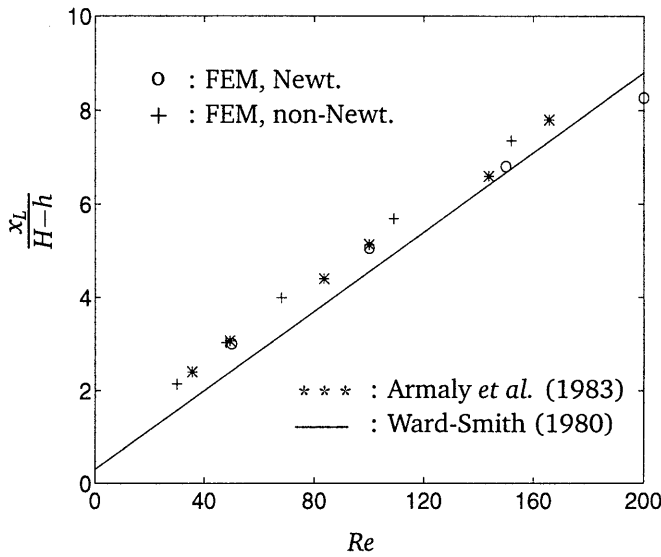
Figure 7.10: *The dimensionless position of the reattachment point for the Newtonian and the non-Newtonian fluid. The reattachment length (x_L) is made dimensionless with step height ($H - h$).*

7.4.2   Characterization of the gel layer

The first step in the procedure, given in figure 7.4, involves calibration of the gel layer. The calibration procedure starts with the computation of the wall shear stress induced by a Newtonian fluid (*step 1*). The computed wall shear stress serves as an input for the computation of the displacement of the gel layer. The properties of the gel layer are established by the comparison of the computed and measured displacements (*step 2*).

The buffer solution served as Newtonian calibration fluid ($\eta = 1$ *mPas*, $Re = 150$). The computed wall shear stress along the gel layer is shown in figure 7.11a. The position downstream the step is made dimensionless with the step height:

$$x' = \frac{x}{H - h} \tag{7.11}$$

The zone with flow reversal (negative wall shear stress), the reattachment point, and the development towards fully developed flow can be observed.

Measurement of the displacement of the gel layer for the Newtonian buffer solution was repeated eight times, and the mean displacement of the gelatin layer is shown in figure 7.11b. The displacements approach zero at $x' = 0$ and $x' = 28$. Negative displacements are found in the recirculation zone and a plateau of constant displacement can be observed from $x' = 14$ on.

Deformation of the gel layer is linear with the modulus of the gelatin, allowing for a least square fit of the measured and the computed displacement (figure 7.11b). A
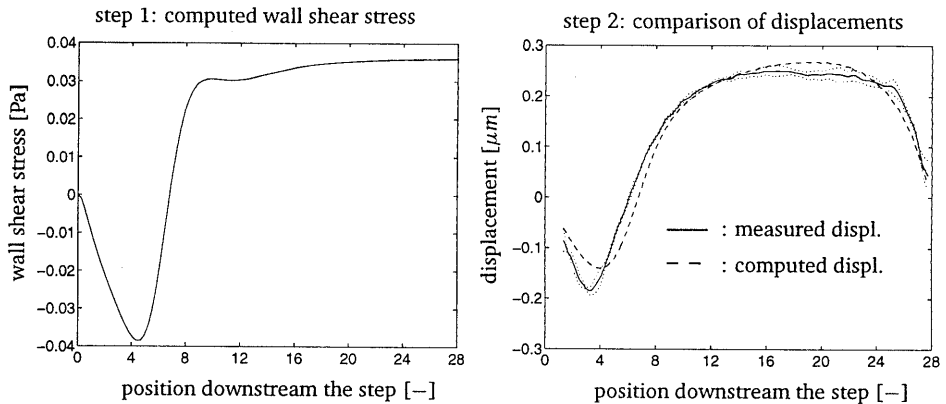
Figure 7.11: *The computed wall shear stress distribution along the gel layer and the measured (solid line) and computed (dashed line) displacement of the gel layer for the buffer solution. The standard deviation of the displacement measurements is indicated by the dotted line. Position behind the step is made dimensionless with step height.*

close agreement between measured and fitted displacements is observed, indicating that the method is suitable to determine wall shear stresses downstream a backward-facing step. From the fitting procedure the modulus of the gelatin was determined ($E = 2440Pa$) and this modulus was used for the subsequent wall shear stress measurements for the red blood cell suspension.

7.4.3   Wall shear stresses: Red blood cell suspension

The displacement measurements for the red blood cell suspension were performed at three flow rates: $Q = 15$, 22.5 and 30 $ml.s^{-1}$. These flow rates correspond to a mean axial inlet velocity of $U = 60$, 90 and 120 $mm.s^{-1}$, respectively. The mean results of eight displacement measurements are shown in the top part of figure 7.12. As expected, the displacements for the red blood cell suspension are larger than those the buffer solution: the viscosity of the red blood cell suspension is higher, thus inducing higher shear stresses and larger displacements. Only at the highest flow rate, significant negative displacements are measured, indicating that flow reversal is less dominant for the red blood cell suspension than for the Newtonian buffer solution. The modulus of the gel layer, determined with the buffer solution, and the measured displacements served as input for the computation of the wall shear stress along the gel layer (figure 7.4, *step 3*). The standard deviation of the measured displacements were used as upper and lower limits, and an indication of the accuracy of the wall shear stress measurements was obtained. The results of the conversion of the measured displacements to wall shear stress distribution is shown in the bottom part of figure 7.12. Negative wall shear stresses are present in the region with flow reversal at the higher flow rates, and a constant wall shear stress is obtained downstream.

step 3:
displacement measurement

step 3 and step 4:
comparison of wall shear stress

position [-]

position [-]

——— : measured WSS　　– – : computed WSS (non-Newt.)　　– · – : computed WSS (Newt.)
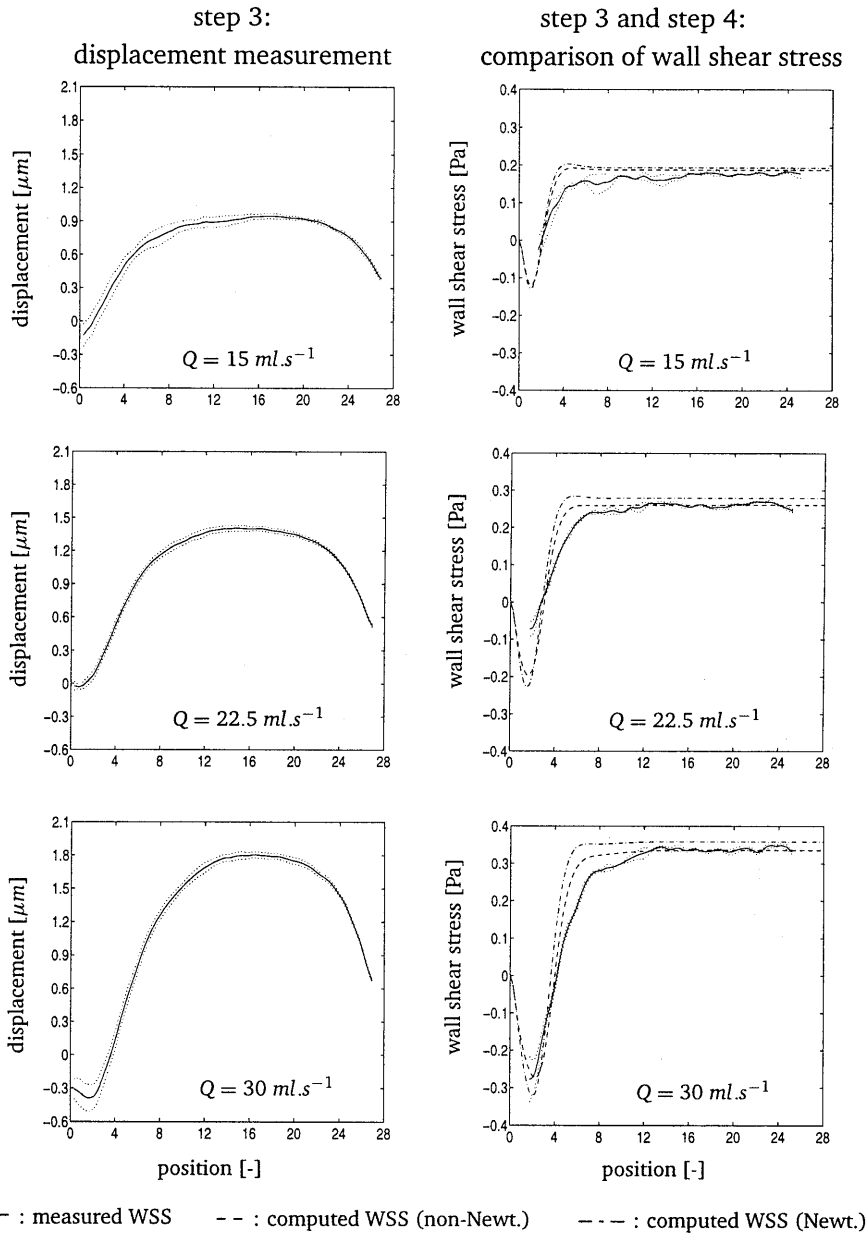
Figure 7.12: *Top figure: displacement measurements of the gel for the red blood cell suspension at three flow rates (solid line). Bottom figure: measured (solid line) wall shear stress for the red blood cell suspension. The computed wall shear stresses are given by the dashed line (non-Newtonian) and the dashed-dotted line (Newtonian, $\eta = \eta_c$). The standard deviation is for the displacement and the wall shear stress is indicated by the dotted line.*

The accurate prediction of reattachment length indicates that the velocity distribution in backward-facing step flow of an inelastic non-Newtonian fluid can be approximated by a Newtonian model, using a characteristic viscosity. Using equation (7.1), characteristic shear rate, viscosity and Re can be computed (table 7.1). These values

Q $ml.s^{-1}$	U $mm.s^{-1}$	$\dot{\gamma}_c$ s^{-1}	η_c $mPa.s$	Re $-$
15	60	25	5.3	29
22.5	90	37.5	5.1	46
30	120	50	4.9	64

Table 7.1: *Values for the characteristic shear rate, viscosity and Re.*

are used to assess the ability of Newtonian fluid model to predict wall shear stress, induced by the red blood cell suspension (figure 7.4, *step 4*).

In the bottom part of figure 7.12, measured and computed wall shear stresses are shown. The measured wall shear stress is compared to the inelastic non-Newtonian and Newtonian predictions. In general, the non-Newtonian fluid model provides an accurate prediction of the measured wall shear stress distribution. The values of the wall shear stress in fully developed flow show excellent agreement: only at the lowest flow rate the model overestimates wall shear stress slightly. The location of the reattachment point is predicted accurately. Only downstream of the reattachment point, measured wall shear stress is significantly lower than computed wall shear stress. The origin of this deviation is not known. From the comparison of the measured and computed wall shear stresses, it can be concluded that the wall shear stresses, induced by the red blood cell suspension, can be predicted accurately with the purely viscous Carreau-Yasuda model. The Newtonian model, based on a characteristic viscosity, also gives a fair prediction of the wall shear stress distribution. However, for all flow rates, the Newtonian fluid model overestimates wall shear stresses: this effect increases with increasing flow rate.

7.5   Discussion and conclusions

The aim of this study was to measure blood flow induced wall shear stress and to assess the ability of a macroscopic model for blood to compute the wall shear stresses. A previously developed method to determine wall shear stress distribution (Gijsen *et al.*, 1997b) was evaluated in backward-facing step flow. The wall shear stress distribution was inferred from the measured displacement of a gelatin layer. This displacement served as an input for a simple, linear elastic, computation of deformation of the gel layer. The wall shear stress was extracted from this computation.

To calibrate the gel layer and to evaluate the proposed method, measurements were performed with a Newtonian fluid. The computed wall shear stress distribution served as a boundary condition for the computation of the deformation of the gelatin layer. The computed displacements were then fitted to the measured displacements, thus

obtaining the modulus of the gel layer. The good agreement between measured and computed displacement indicates that the method can be used to determine wall shear stress downstream a backward-facing step.

The wall shear stress distribution for the red blood cell suspension was determined for three different flow rates. The measured displacement was converted to wall shear stress. The viscometric properties of the red blood cell suspension were modeled with the inelastic Carreau-Yasuda model. This fluid model was applied to compute the wall shear stress distribution. The good agreement between experimental and numerical wall shear stress distribution is indicative of the inelastic behavior of the red blood cell suspension. These results are in agreement with the results of Brookshier and Tarbell (1993) and Gijsen *et al.* (1998). The wall shear stress was predicted accurately using a macroscopic fluid model. In this model, the fluid is assumed to be homogeneous. Therefore, the particulate nature of the red blood cell suspension does not seem to influence flow behavior and wall shear stress distribution.

The results for the non-Newtonian fluid model were approximated quite well by a Newtonian model, using a viscosity, based on an average shear rate in the inlet channel (Halmos *et al.*, 1975a). The Newtonian model is bound to overestimate wall shear stress in regions with higher wall shear rates: the scaling procedure should be applied with caution.

The influence of unsteady flow on wall shear stress distribution, induced by a red blood cell suspension, remains to be investigated. Application of the method, presented in this study, to unsteady flow conditions requires dynamic measurement of the displacement of the gelatin layer. The approach, proposed by Reynolds and Toal (1992), enables real-time displacement measurement with speckle interferometry, and could be applied to measure time-dependent displacement of the gelatin layer downstream a backward-facing step.

Acknowledgements

Chapter 8

Discussion and conclusions

8.1 General discussion

Disturbance of wall shear stress distribution in large arteries is believed to be one the key factors in the development of atherosclerosis and failure of vascular grafts. Modeling of the blood flow induced wall shear stress in large and medium sized arteries therefore qualifies as an important research area and is the main topic of this thesis. In modeling wall shear stress, the choice of an appropriate constitutive model for blood is crucial.

Constitutive models for blood

Blood is a concentrated suspension of blood cells in plasma and it exhibits a range of non-Newtonian properties. These properties mainly depend on the aggregation, orientation and deformation of red blood cells. Aggregates are unlikely to occur in large arteries: the build-up time for red blood cell aggregates is rather long and shear rates are high (e.g. Sharp *et al.*, 1996). Blood in large artery flow can therefore be regarded as a suspension of deformable red blood cells in Newtonian plasma with the characteristic time scale of order 0.1 *s*.

Blood can be modeled by a range of constitutive models, the simplest being a Newtonian fluid model, the more complex microscopic models describing the behavior of individual red blood cells. However, since the concentration distribution of red blood cells in large arteries can be assumed to be homogeneous, a macroscopic model for blood can be adopted. The class of constitutive models is then limited to Newtonian, inelastic shear thinning and viscoelastic models. The influence of viscoelasticity on the flow phenomena is determined by the Deborah number (*De*: a measure for unsteady viscoelasticity) and the Weissenberg number (*We*: a measure for convective viscoelasticity). Another dimensionless parameter, the shear rate number, gives an estimate of the importance of shear thinning. Using these dimensionless parameters, combining characteristic properties of the fluid and flow conditions, it can be

concluded that both shear thinning and viscoelasticity should be included in a constitutive model for blood.

Flow of a red blood cell suspension

A red blood cell suspension was used to investigate steady flow downstream a backward-facing step: velocity, shear rate and wall shear stress distributions were determined experimentally and numerically. The red blood cell suspension was modeled using the inelastic, shear thinning Carreau-Yasuda model.
The velocity and shear rate distribution were measured by means of ultrasound velocimetry. The comparison between numerical and experimental results revealed a good agreement: both the position and the size of the recirculation zone downstream the step, as well as recovery to a near parabolic velocity distribution were predicted accurately. Since an inelastic model was applied to compute the velocity distribution, it can be concluded that the velocity and shear rate distribution in flow of a red blood cell suspension is not significantly influenced by viscoelasticity.
Wall shear stress distribution was measured by employing a new experimental technique. A gel layer, attached to the wall of the flow model downstream the step, served as a sensing element. The gel layer deforms under influence of flow induced wall shear stress. The measured displacement of the gel layer, combined with the properties of the gel, are used to determine wall shear stress. The displacement of the gel layer was measured by means of speckle pattern interferometry, and a resolution of approximately 0.01 *Pa* was achieved in determining wall shear stress.
The wall shear stress distribution for a red blood cell suspension was determined for three different flow rates. The good agreement between experimental and numerical wall shear stress distribution is indicative for the marginal influence of the elastic behavior of the red blood cell suspension in steady flow. Furthermore, the particulate nature of the red blood cell suspension, that could cause an inhomogeneous viscosity due to migration of the red blood cells, does not seem to influence flow behavior and wall shear stress distribution.
From the above, it can be concluded that both velocity and wall shear stress distribution downstream a backward-facing step under steady flow conditions for a red blood cell suspension can be modeled with an inelastic shear thinning fluid model.

Flow of a macroscopic blood analog fluid

The Carreau-Yasuda model was successfully employed to model the behavior of a macroscopic blood analog fluid in various geometries under physiologically relevant flow conditions. A concentrated KSCN solution with 250 *ppm* Xanthan gum served as a macroscopic blood analog fluid. Laser Doppler anemometry was applied to obtain detailed quantitative information on velocity distribution in a model of the carotid bifurcation under steady flow conditions and in a 90° degree curved tube for unsteady flow. An excellent agreement between numerical and experimental data was obtained, although the elastic properties of the blood analog fluid in viscometric flow were similar to *whole* blood.

Despite the relatively large value of *We*, velocity and wall shear stress distribution was modeled accurately by employing the inelastic Carreau-Yasuda model. The results of the unsteady flow experiments in the 90° degree curved tube, combined with the fact that the Weissenberg number is larger than the Deborah number, indicates that the Carreau-Yasuda model is appropriate for modeling blood flow in large arteries. Only non-linear viscoelastic behavior of whole blood or a profound influence of unsteady flow on the concentration distribution of red blood cells could be responsible for a failure of the Carreau-Yasuda model to describe blood flow in large arteries under unsteady flow conditions.

Characteristic viscosity

In the experiments with the macroscopic blood analog fluid, the velocity distribution for the non-Newtonian fluid showed significant differences when compared to a New-tonian fluid model, having a a viscosity equal to the high shear viscosity of the blood analog fluid ($\eta = \eta_\infty$). However, the non-Newtonian results were approximated quite accurately by a Newtonian model based on a *characteristic* viscosity. The character-istic viscosity was obtained by evaluating viscosity of the non-Newtonian fluid at a characteristic shear rate. The characteristic shear rate was based on an average shear rate (e.g. Thurston, 1973; Pak *et al.*, 1990; Baaijens *et al.*, 1993), rather than on wall shear rate (e.g. Mann and Tarbell, 1990; Cho and Kensey, 1991).
The numerical investigation of Perktold *et al.* (1991) showed only a minor influence of shear thinning on the flow features in the carotid bifurcation. The characteristic shear rate in their study was higher, the characteristic viscosity therefore lower, and the influence of the shear thinning properties on the velocity distribution can be ex-pected to be less dominant. This indicates that blood flow in large arteries is sensitive to the characteristic shear rate. Although speculative, the sensitivity to the character-istic shear rate might also help to explain the differences between the flow fields in younger and older individuals (Reneman *et al.*, 1985). Since the characteristic shear rate in the older individuals is lower, the characteristic viscosity is higher, and a more viscous behavior of blood is expected. Using these arguments, the absence of flow reversal in the internal carotid artery in the older individuals could be explained.
The characteristic viscosity cannot be used to predict wall shear stress. Since the velocity distribution is approximated accurately, the Newtonian model, based on the characteristic viscosity, underestimates wall shear stresses in low wall shear rate re-gions and overestimates wall shear stress in regions with high wall shear rates. Fur-thermore, application of the characteristic viscosity cannot be generalized to all ge-ometries and flow conditions. The merit of this linearization procedure lies in the description of the character of the flow: the characteristic viscosity should be used to determine the dimensionless parameters in blood flow in large arteries.

Wall shear stress in a 90° degree curved tube

Wall shear stress in a 90° curved tube serves as an illustration for the discussion above. In figure 8.1, axial wall shear stresses in the plane of symmetry along the

inner bend and outer bend are presented. The results for the Carreau-Yasuda model
and for two Newtonian models ($\eta = \eta_\infty$ and $\eta = \eta_c$) are shown at the three time
steps used in chapter 4. The non-Newtonian fluid model predicts an increasing wall

wall shear stress along the outer bend

wall shear stress along the inner bend

plane [degree]

o——o : non-Newtonian   *- -* : Newt. ($\eta = \eta_c$)   +— + : Newt. ($\eta = \eta_\infty$)
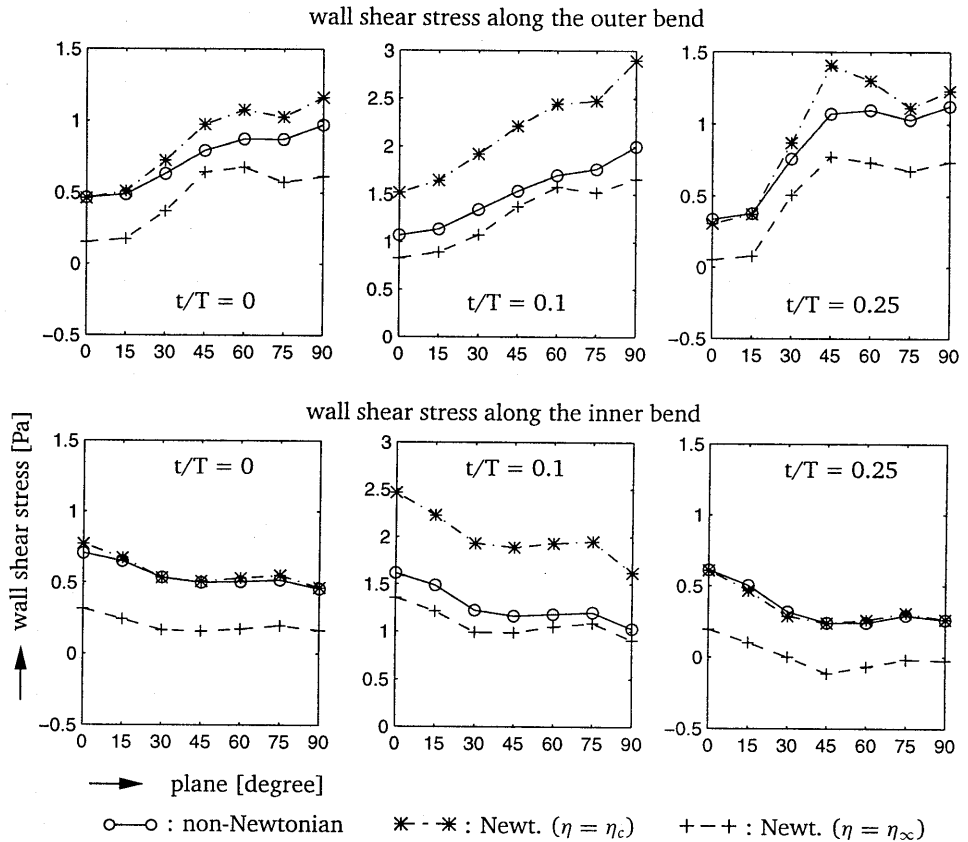
Figure 8.1: *Axial wall shear stress in a bend. The time steps and the planes are
identical to the ones used in chapter 4.*

shear stress along the outer bend for increasing angle at every time step. Peak wall
shear stresses are observed during systole ($t/T = 0.1$): a maximum value of 2 *Pa* is
attained. Along the inner bend, wall shear stress decreases with increasing angle. The
Newtonian model ($\eta = \eta_\infty$) underestimates wall shear stress along the outer bend.
The differences between Newtonian and non-Newtonian fluid models is even bigger
along the inner bend: flow reversal, present for the Newtonian fluid at begin diastole
($t/T = 0.25$), is absent for the non-Newtonian fluid model. The Newtonian model,
based on the characteristic viscosity, overestimates wall shear stress along the outer
bend. Especially during peak systole, wall shear stresses are too high. Along the inner
bend, a good approximation is found for begin and end diastole.

Final conclusions

Keeping some reservations of the validity of the Carreau-Yasuda model for unsteady flow conditions in mind, the following set of final conclusions can be formulated:

- Velocity distribution and wall shear stress of blood flow in large arteries can be modeled with an inelastic Carreau-Yasuda model.

- The particulate nature of blood appears to be unimportant for prediction of blood flow induced wall shear stress.

- A viscosity, based on a characteristic shear rate, should be used to determine dimensionless parameters in blood flow.

8.2   Implications for clinical research

The findings in this thesis may have consequences regarding the research on response of endothelial cells and the failure of vascular grafts. The *in-vitro* research on the response of cultured endothelial cells to wall shear stress should preferably mimic the *in-vivo* loading conditions. Basically, two different approaches can be followed to obtain these *in-vivo* loading conditions of the endothelial cells: ultrasound and magnetic resonance imaging (MRI).

Ultrasound velocimetry is a widely spread non-invasive measuring technique. Ultrasound studies can be used to obtain detailed information on the geometry of the vascular tree, and velocity measurements can be performed to determine flow rate through and velocity distribution in arteries. Geometry and flow rates can then be used to compute wall shear stress distribution *in-vivo*. The measured velocity distribution can serve as a validation of the numerical procedure. The same observations hold for MRI, and the study of (Steinman and Rutt, 1997) is an example of the potentials of this approach. They obtained a full 3D geometry of the carotid bifurcation and flow rates by means of MRI. These data were used as an input to compute velocity and wall shear stresses. The computations of the *in-vivo* loading conditions of the endothelial cell require a constitutive equation for blood. Steinman and Rutt (1997) used a Newtonian fluid model for blood. The results in this thesis indicate that application of an inelastic shear thinning model is more appropriate. The parameters for these models depend strongly on concentration and properties of the constituents of blood. These parameters have to be determined for each individual separately: viscometry seems to be the most accurate way of determining these parameters. However, since velocity profiles can be measured, both with ultrasound and MRI, some effort on finding these parameters on the bases of the measured velocity profiles seems justified.

Following the procedure, described above, the *in-vivo* blood flow induced wall shear stresses, acting on the endothelial cells, can be determined, and hemodynamical variables, such as wall shear stress, can be correlated to vascular diseases in a non-invasive manner. For the *in-vitro* research on the response of endothelial cells, this information is vital. The imposed wall shear stresses in the experimental setups, as

used by (e.g. Truskey *et al.*, 1995), can be adjusted to mimic the *in-vivo* wall shear stress distribution.

Velocity profiles measured with ultrasound are often used to assess wall shear rates. In the central part of arteries, this clinical procedure provides a good approximation. At near wall sites, the experimentally determined shear rates tend to underestimate true shear rates (see chapter 5). Extrapolation of estimated shear rate in the central part of the artery to obtain wall shear rate is feasible: information of the geometry and flow rates suffices to compute wall shear rates, thus providing a direct and simple procedure to evaluate an important hemodynamic variable.

In the design of vascular grafts, a smooth transition of wall shear stress at the anastomoses seems to be essential in the functioning of the grafts. A numerical procedure, modeling blood as a inelastic shear thinning fluid, could be applied to predict wall shear stress distribution at anastomoses. The diameter and angle of the graft can be varied to minimize wall shear stress gradients.

Palmen *et al.* (1997) investigated the influence of a mild stenosis on velocity distribution in a carotid artery model to promote early detection of atherosclerosis *in-vivo*. Only minor disturbances of the velocity field were detected, shear layer disturbances being the most promising detection parameter. These shear layer disturbances are more pronounced at higher *Re*. In the definition of *Re*, $\eta = \eta_\infty$ was used. This research has shown that a characteristic viscosity should be used, leading to a significant decrease of *Re*. Early detection of stenosis, using velocity measurements, is therefore even less feasible than concluded by Palmen *et al.* (1997).

In the discussion above, the development of atherosclerosis and functioning of vascular grafts was discussed in the light of blood flow induced wall shear stresses. In these observations, elasticity of the vessel wall was not included. The elasticity of the vessel wall is important for two reasons: its influence on deformation of endothelial cells and on blood flow. The endothelium is subjected to blood flow induced wall shear stresses *and* to strains, caused by the deforming vessel wall. The deformation of the vessel wall triggers various processes in the endothelium (e.g. Zhao *et al.*, 1995), and atherosclerosis is probably caused by a combination of disturbed wall shear stress distributions and non-uniform vessel wall deformations. In the study of Rutten (1998), the loading of the endothelium due to deforming vessel wall is described. Secondly, the deformation and global movement of the vessel might influence the velocity distribution in the vessel (Rutten, 1998). So both in studies on the development of atherosclerosis and in the design of vascular grafts, the non-Newtonian properties of blood should be included in combination with deformation of the artery.

To further investigate the relative importance of the wall shear stress versus vessel deformation, an extension of the study of Zhao *et al.* (1995) is required. They studied the influence of cyclic deformation of the vessel wall and of wall shear stress on the morphology of and the F-actin organization in endothelial cells in a straight tube. These investigations should be conducted in a geometry where atherosclerosis typically develops: an elastic curved tube, lined with endothelial cells, seems to be an appropriate model. The response of endothelium can be studied under pressure variations to investigate the influence of non-uniform vessel deformation, and under physiological flow conditions to study the influence of wall shear stress.

Bibliography

Agrawal, Y., Talbot, L., and Gong, K. (1978). Laser anemometer study of flow development in curved circular pipes. *J. Fluid Mech.*, **85**, 497–518.

Alberts, B., Bray, D., Lewis, J., Raff, M., Roberts, K., and Watson, J. D. (1994). *Molecular biology of the cell*. Garland Publishing Inc., 3rd edition.

Armaly, B. F., Durst, F., Pereira, J. C. F., and Schöning, B. (1983). Experimental and theoretical investigation of backward-facing step flow. *J. Fluid Mech.*, **127**, 473–496.

Baaijens, J. P. W., van Steenhoven, A. A., and Janssen, J. D. (1993). Numerical analysis of steady generalized Newtonian flow in a 2D model of the carotid artery bifurcation. *Biorheology*, **30**, 63–74.

Ballyk, P. D., Steinman, D. A., and Ethier, C. R. (1994). Simulation of non-Newtonian blood flow in an end-to-side anastomosis. *Biorheology*, **31**, 565–586.

Berger, S. A., Talbot, L., and Yao, L. S. (1983). Flow in curved pipes. *Annual Review of Fluid Mechanics*, **15**, 461–512.

Bharadvaj, B. K., Mabon, R. F., and Giddens, D. P. (1982a). Steady flow in a model of the human carotid bifurcation. Part I: Flow visualization. *J. Biomechanics*, **15**, 349–362.

Bharadvaj, B. K., Mabon, R. F., and Giddens, D. P. (1982b). Steady flow in a model of the human carotid bifurcation. Part II: Laser-Doppler measurements. *J. Biomechanics*, **15**, 363–378.

Bird, R. B., Armstrong, R. C., and Hassager, O. (1987). *Dynamics of polymer liquids*, volume 1. John Wiley and Sons, 2nd edition.

Bovendeerd, P. H. M., van Steenhoven, A. A., van de Vosse, F. N., and Vossers, G. (1987). Steady entry flow in a curved pipe. *J. Fluid Mech.*, **177**, 223–246.

Bowen, P. J., Davies, A. R., and Walters, K. (1991). On viscoelastic effects in swirling flows. *Journal of non-Newtonian fluid mechanics*, **38**, 113–126.

Brands, P. J., Hoeks, A. P. G., Hofstra, L., and Reneman, R. S. (1995). A noninvasive method to estimate wall shear rate using ultrasound. *Ultrasound in Medicine and Biology*, **21**, 171–185.

Brands, P. J., Hoeks, A. P. G., Ledoux, L. A. F., and Reneman, R. S. (1997). A radio

frequency domain complex cross-correlation model to estimate blood flow velocity and tissue motion by means of ultrasound. *Ultrasound in Medicine and Biology*, **23**(6), 911–920.

Brookshier, K. A. and Tarbell, J. M. (1993). Evaluation of a transparent blood analog fluid: Aqueous Xanthan gum/glycerin. *Biorheology*, **30**, 107–116.

Brookshier, K. K. and Tarbell, J. M. (1992). Effect of hematorcrit on wall shear rate in oscillatory flow: Do the elastic properties of blood play a role? *Biorheology*, **28**, 569–587.

Bugliarello, G. and Sevilla, J. (1970). Velocity distribution and other characteristics of steady and pulsatile blood flow in fine glass tubes. *Biorheology*, **7**, 85–107.

Caro, C. G., Fitzgerald, J. M., and Schroter, R. C. (1971). Atheroma and arterial wall shear: Observation, correlation and proposal of a shear dependent mass transfer mechanism for atherogenesis. *Proc. Roy. Soc. London, B*, **177**, 109–159.

Caro, C. G., Pedley, T. J., and Schroter, R. C. (1978). *Mechanics of the Circulation*. Oxford University Press.

Chandran, K. B. and Yearwood, T. L. (1981). Experimental study of physiological pulsatile flow in a curved tube. *J. Fluid Mech.*, **111**, 59–85.

Chien, S., Usami, S., Dellenback, R. J., and Gregersen, M. I. (1970). Shear-dependent deformation of erythrocytes in rheology of human blood. *American Journal of Physiology*, **219**, 136–142.

Cho, Y. I. and Kensey, R. (1991). Effects of the non-Newtonian viscosity of blood flows in a diseased arterial vessel. Part 1: Steady flows. *Biorheology*, **28**, 241–262.

Clegg, D. B. and Power, G. (1963). Flow of a Bingham fluid in a slightly curved tube. *Appl. sci. Res. A*, **12**, 199–212.

Cloud, G. (1995). *Optical methods of engineering analysis*. Cambridge University Press.

Cokelet, G. R. (1972). The rheology of human blood. In Y. C. Fung and M. Anliker, editors, *Biomechanics: its foundations and objectives*, chapter 4. Prentice Hall.

Cokelet, G. R. and Meiselman, H. J. (1968). Rheological comparison of hemoglobin solutions and erythrocyte suspensions. *Science*, **162**, 275–277.

Creath, K. (1985). Phase-shifting speckle interferometry. *Applied Optics*, **24**, 3053–3058.

Cuvelier, C., Segal, A., and van Steenhoven, A. A. (1986). *Finite element methods and Navier-Stokes equations*. D. Reidel Publishing Comp., Dordrecht.

Das, B. (1992). Flow of a Bingham fluid in a slighlty curved tube. *Int. J. Engng. Sci.*, **30**, 1193–1207.

Davies, P. F. (1995). Flow-mediated endothelial mechanotransduction. *Physiological Reviews*, **75**(3), 519–560.

Davies, P. F. and Tripathi, S. C. (1993). Mechanical stress mechanisms and the cell:

an endothelial paradigm. *Circulation Research*, **72**, 239–245.

Dean, W. R. (1927). Note on the motion of fluid in a curved pip. *Phil. Mag.*, **4**(20), 208–223.

Dean, W. R. (1928). The stream-line motion of fluid in a curved pipe. *Phil. Mag.*, **5**(30), 673–695.

Fårhæus, R. and Lindquist, T. (1931). The viscosity of the blood in narrow capillary tubes. *American Journal of Physiology*, **96**, 562–568.

Friedman, M. H., Peters, O. J., Bargero, C. B., Hutchins, G. M., and Mark, F. F. (1981). Correlation between intimal thickness and fluid shear in human arteries. *Atherosclerosis*, **39**, 425–436.

Fung, Y. C. (1993). *Biomechanics: mechanical properties of living tissues.* Springer-Verlag, 2nd edition.

Giddens, G. P., Zarins, C. K., and Glagov, S. (1990). Response of arteries to near-wall fluid dynamic behavior. *Applied Mechanical Review*, **43**, S98–S102.

Gijsen, F. J. H., van de Vosse, F. N., and Janssen, J. (1997a). Analysis of non-Newtonian entrance flow in a 90° curved tube. In K. B. Chandran, R. V. jr., and M. Hefzy, editors, *Proceedings of the 1997 bioengineering conference*, ASME, BED-vol. 35, pages 11–12.

Gijsen, F. J. H., Goijaerts, A., van de Vosse, F. N., and Janssen, J. D. (1997b). A new method to determine wall shear stress distribution. *J. of Rheology*, **41**(5), 995–1006.

Gijsen, F. J. H., Brands, P. J., van de Vosse, F. N., and Janssen, J. D. J. (1998). Flow downstream of a backward-facing step: evaluation of a constitutive model for blood. *submitted to Journal of Vascular Investigation.*

Glagov, S., Bassiouy, H. S., Giddens, D. P., and Zarins, C. K. (1995). Intimal thickening: morphogenesis, functional significance and detection. *Journal of Vascular Investigation*, **1**(1), 2–15.

Goldsmith, H. L. (1993). Poiseuille medal award lecture: From papermaking fibers to human blood cells. *Biorheology*, **30**, 165–190.

Goldsmith, H. L. and Marlow, J. C. (1979). Flow behaviour of erythrocytes. II: Particle motions in concentrated suspensions of ghost cells. *J. of Colloid and Interface Science*, **71**, 383–407.

Halmos, A. L., Boger, D. V., and Cabelli, A. (1975a). The behavior of a power-law fluid flowing through a sudden expansion. Part I. A numerical solution. *AIChE Journal*, **21**(3), 540–549.

Halmos, A. L., Boger, D. V., and Cabelli, A. (1975b). The behavior of a power-law fluid flowing through a sudden expansion. Part II. Experimental verification. *AIChE Journal*, **21**(3), 549–553.

Hanratty, T. J. and Campbell, J. A. (1983). Measurement of wall shear stress. In R. J. Goldstein, editor, *Fluid Mechanics Measurements*, chapter 11. Hemisphere Publish-

ing Company, New York.

Hoeks, A. P. G., Arts, T. G. J., Brands, P., and Reneman, R. (1993). Comparison of the preformance of the RF cross correlation and Doppler autocorrelation technique to estimate the mean velocity of simulated ultrasound signals. *Ultrasound Med. Biol.*, **19**(9), 727–740.

Hoeks, A. P. G., Samijo, S. K., Brands, P. J., and Reneman, R. S. (1995). Assesment of wall shear rates in humans: and ultrasound study. *Journal of Vascular Investigation*, **1**(3), 108–117.

Hofstra, L. (1995). *Intimal hyperplasia in human vascular grafts*. Ph.D. thesis, Universiteit Maastricht.

James, P. W. (1975). Unsteady elastico-viscous flow in a curved pipe. *Rheol. Acta*, **14**, 679–687.

Jones, J. R. (1960). Flow of a non-Newtonian liquid in a curved pipe. *Quart. Journ. Mech. and Applied Math.*, **13**(4), 428–443.

Jones, R. and Wykes, C., editors (1989). *Holographic and Speckle Interferometry*. Cambridge University Press.

Karnis, A., Goldsmith, H. L., and Mason, S. G. (1966). The kinetics of flowing dispersions. I: concentrated suspensions of rigid particles. *J. of Colloid and Interface Science*, **22**, 531–553.

Koh, C. J., Hookham, P., and Leal, L. G. (1994). An experimental investigation of concentrated suspension flows in a rectangular channel. *J. of Fluid Mech.*, **266**, 1–32.

Krieger, I. M. and Dougherty, T. J. (1959). A mechanism for non-Newtonian flow in suspensions of spheres. *Trans. Soc. Rheology*, **3**, 137–152.

Ku, D. N. and Allen, R. C. (1995). Vascular grafts. In J. D. Bronzino, editor, *The biomedical engineering handbook*, chapter 124, pages 1871–1878. CRC Press.

Ku, D. N. and Giddens, D. P. (1987). Laser Doppler measurements of pulsatile flow in a model carotid bifurcation. *J. Biomechanics*, **20**, 407–421.

Ku, D. N. and Liepsch, D. (1986). The effect of non-Newtonian viscoelasticity and wall elasticity on flow at a 90 degree bifurcation. *Biorheology*, **23**, 359–370.

Liepsch, D. and Moravec, S. (1984). Pulsatile flow of non-Newtonian fluid in distensible models of human arteries. *Biorheology*, **21**, 571–586.

Lou, Z. and Yang, W. (1993). A computer simulation of the non-Newtonian blood flow at the aortic bifurcation. *J. of Biomechanics*, **26**, 37–49.

Macosko, C. W. (1994). *Rheology: principles, measurements and applications*. Weinheim.

Mann, D. E. and Tarbell, J. M. (1990). Flow of non-Newtonian blood analog fluids in rigid curved and straight artery models. *Biorheology*, **27**, 711–733.

McMillan, D. E., Strigberger, J., and Utterback, N. G. (1987). Rapidly recovered

transient flow resistance: a newly discovered property of blood. *American Journal of Physiology*, **253**, 919–926.

Merrill, E. W. (1969). Rheology of blood. *Physiological Reviews*, **49**, 863–888.

Mullin, T. and Greated, C. A. (1980). Oscillatory flow in curved pipes. Part I: The developing-flow case. *J. Fluid Mech.*, **98**, 383–395.

Naruse, T. and Tanishita, K. (1996). Large curvature effect on pulsatile flow in a curved tube: model experiment simulating blood flow in an aortic arch. *J. of Biomechanical Engineering*, **118**, 180–186.

Nerem, R. M. (1992). Vascular fluid mechanics, the arterial wall, and atherosclerosis. *J. of Biomechanical Engineering*, **114**, 274–282.

Nerem, R. M. (1993). Hemodynamics and the vascular endothelium. *J. of Biomechanical Engineering*, **115**, 510–514.

Nott, P. R. and Brady, J. F. (1994). Pressure-driven flow of suspensions: simulation and theory. *J. Fluid Mech.*, **275**, 157–199.

Olson, D. E. and Snyder, B. (1985). The upstream scale of flow development in curved circular pipes. *J. Fluid Mech.*, **150**, 139–158.

Pak, B., Young, Y. I., and Choi, S. U. S. (1990). Separation and reattachment of non-Newtonian fluid flows in a sudden expansion pipe. *Journal of Non-Newtonian Fluid Mechanics*, **37**, 175–199.

Palmen, D. E. M., Gijsen, F. J. H., van de Vosse, F. N., and Janssen, J. D. (1997). Diagnosing minor stenoses in carotid artery bifurcation models using the disturbed velocity field. *Journal of Vascular Investigation*, **3**(1), 26–41.

Parmar, D. S. (1991). A novel technique for response function determination of shear sensitive cholesteric crystals for boundary layer investigations. *Rev. Sci. Instrum.*, **62**(6).

Pedley, T. J. (1980). *The fluid mechanics of large blood vessels*. Cambridge University Press.

Perktold, K. and Hilbert, D. (1986). Numerical simulation of pulsatile flow in a carotid bifurcation model. *J. Biomed. Eng.*, **8**, 193–199.

Perktold, K., Peter, R. O., Resch, M., and Langs, G. (1991). Pulsatile non-Newtonian flow in three-dimensional carotid bifurcation models: a numerical study of flow phenomena under different bifurcation angles. *J. Biomed. Eng.*, **13**, 507–515.

Phan-Thien, N. and Fang, Z. (1996). Entrance length and pulsatile flows of a model concentrated suspension. *J. Rheology*, **40**, 521–529.

Phibbs, R. H. (1968). Orientation and distribution of erythrocytes in blood flowing in medium-sized arteries. In A. L. Copley, editor, *Hemorheology*, pages 617–630. Pergamon Press, Oxford.

Philips, R. J., Armstrong, R. C., Brown, R. A., Graham, A. L., and Abbott, J. R. (1992). A constitutive equation for concentrated suspensions that accounts for shear-induced particle migration. *Phys. Fluids*, **4**, 30–40.

Quemada, D. (1978). Rheology of concentrated disperse systems. II. a model for non-Newtonian shear viscosity in steady flows. *Rheol. Acta*, **17**, 632–642.

Quemada, D. (1984). Towards a unified model of elasto-thixotropy of biofluids. *Biorheology*, **21**, 423–436.

Quemada, D. (1993). A non-linear Maxwell model of biofluids: application to normal blood. *Biorheology*, **30**, 253–265.

Quemada, D. and Droz, R. (1983). Blood viscoelasticity and thixotropy from stress formation and relaxation measurements. *Biorheology*, **20**, 635–651.

Reneman, R. S., van Merode, T., Hick, P., and Hoeks, A. P. G. (1985). Flow velocity patterns in and distensibility of the carotid artery bulb in subjects of various ages. *Circulation*, **71**(3), 500–509.

Reynolds, M. and Toal, V. (1992). An interferometric linear in-plane position transducer. *Optics and Laser Technology*, **24**, 59–65.

Rindt, C. C. M. (1989). *Analysis of the three-dimensional flow field in the carotid artery bifurcation*. Ph.D. thesis, Eindhoven University of Technology.

Rindt, C. C. M. and van Steenhoven, A. A. (1996). Unsteady flow in a rigid 3-D model of the carotid artery bifurcation. *J. of Biomechanical Engineering*, **118**, 90–96.

Rindt, C. C. M., van Steenhoven, A. A., Janssen, J. D., Reneman, R. S., and Segal, A. (1990). A numerical analysis of steady flow in a three-dimensional model of the carotid artery bifurcation. *J. Biomechanics*, **23**, 461–473.

Rindt, C. C. M., van Steenhoven, A. A., Janssen, J. D., and Vossers, G. (1991). Unsteady entrance flow in a 90° curved tube. *J. Fluid Mech.*, **226**, 445–474.

Robertson, A. M. and Muller, S. J. (1996). Flow of Oldroyd-B fluids in curved pipes of circular and annular cross-section. *Int. J. Non-Linear Mechanics*, **31**(1), 1–20.

Rodkiewicz, C. M., Sinha, P., and Kennedy, J. S. (1990). On the application of a constitutive equation for whole human blood. *J. of Biomechanical Engineering*, **112**, 198–206.

Ross, R. and Glomset, J. A. (1976). The pathogenesis of atherosclerosis. *New England Journal of Medicine*, **295**(7), 369–377.

Rutten, M. C. M. (1998). *Fluid-solid interaction in large arteries*. Ph.D. thesis, Eindhoven University of Technology.

Salam, T. A., Lumsden, A. B., Suggs, W. D., and Ku, D. N. (1996). Low shear stress promotes intimal hyperplasia thickening. *Journal of Vascular Investigation*, **2**(1), 12–23.

Samijo, S. K., Willigers, J. M., Brands, P. J., Barkhuysen, R., Reneman, R. S., Kitslaar, P. J. E. H. M., and Hoeks, A. P. G. (1997). Reproducability of shear rate and shear stress assessment by means of ultrasound in the common carotid artery of young human males and females. *Ultrasound in Medicine and Biology*, **23**(4), 583–590.

Sato, M. and Oshima, N. (1994). Flow-induced changes in shape and cytoskeletal structure of vascular endothelial cells. *Biorheology*, **31**(2), 143–153.

Schmid-Schönbein, H., Wells, R. E., and Goldstone, J. (1971). Fluid drop-like behavior of erythrocytes- disturbance in pathology and its quantification. *Biorheology*, 7, 227–234.

Segal, A. (1984). *Sepran user manual and programmers guide*. Ingenieursbureau Sepra, Leidschendam.

Segal, G. and Vuik, K. (1995). A simple iterative linear solver for the 3D incompressible Navier-Stokes equations discretized by the finite elment method. Technical Report 95-64, Delft University of Technology.

Sharp, M. K., Thurston, G. B., and Moore, Jr, J. E. (1996). The effect of blood viscoelasticity on pulsatile flow in stationary and axially moving tubes. *Biorheology*, 33, 185–208.

Singh, M. P. (1974). Entry flow in a curved pipe. *J. Fluid Mech.*, 65, 517–539.

Singh, R. P. and Mishra, P. (1980). Friction factor for Newtonian and non-Newtonian fluid flow in curved pipes. *Journal of Chemical Engineering of Japan*, 13(4), 275–280.

Soh, W. Y. and Berger, S. A. (1984). Laminar entrance flow in a curved pipe. *J. Fluid Mech.*, 148, 109–135.

Steinman, D. A. and Rutt, B. K. (1997). Computed hemodynamics of an imaged human carotid artery bifurcation. In K. B. Chandran, R. V. jr., and M. Hefzy, editors, *Proceedings of the 1997 bioengineering conference*, ASME, BED-vol. 35, pages 341–342.

Takami, T., Sudou, K., and Tomita, Y. (1990). Flow of non-Newtonian fluids in curved pipes. *JSME International Journal*, 33(1), 26–32.

Talbot, L. and Chong, K. O. (1983). Pulsatile entrance flow in a curved pipe. *J. Fluid Mech.*, 127, 1–25.

Tangelder, G. J., Slaaf, D. W., Muijtjens, A. M. M., Arts, T., oude Egbrink, M. G. A., and Reneman, R. S. (1986). Velocity profiles of blood platelets and red blood cells flowing in arterioles of the rabbit mesentry. *Circulation Research*, 59, 505–514.

Tanner, L. H. and Blows, L. G. (1976). A study of the motion of oil films on surfaces in air flow, with application to the measurement of skin friction. *Journal of Physics E.*, 9, 194–202.

Thurston, G. B. (1973). Frequency and shear rate dependence of viscoelasticity of human blood. *Biorheology*, 10, 375–381.

Thurston, G. B. (1979). Rheological parameters for the viscosity, viscoelasticity and thixotropy of blood. *Biorheology*, 16, 149–162.

Truskey, G. A., Barber, K. M., Robey, T. C., Olivier, L. A., and Combs, M. P. (1995). Characterization on a sudden expansion flow hcamber to study the response of endothelium to flow recirculation. *J. of Biomechanical Engineering*, 117, 203–210.

Uijttewaal, W. S. J. (1993). *On the motion of particles in bounded flows*. Ph.D. thesis, Rijksuniversiteit Utrecht.

van de Vosse, F. N. (1987). *Numerical analysis of carotid artery flow*. Ph.D. thesis, Eindhoven Univerisity of Technology.

van de Vosse, F. N., van Steenhoven, A. A., Segal, A., and Janssen, J. D. (1989). A finite element analysis of steady laminar flow in a 90 degree curved tube. *Int. J. for Numerical Methods in Fluids*, **9**, 275–287.

van Haasteren, A. J. P. (1994). *Real-time phase stepped speckle interferometry*. Ph.D. thesis, Delft University of Technology.

Ward-Smith, A. J. (1980). *Internal fluid flow*. Clarendon Press.

Williams, M. C., Rosenblatt, J. S., and Soane, D. S. (1993). Theory of blood rheology based on a statistical mechanics treatment of rouleaux, and comparison with data. *Intern. J. Polymeric Mater.*, **21**, 57–63.

Winter, K. G. (1977). An outline of the techniques available for the measurement of skin friction. *Prog. Aerosp. Sci.*, **18**, 1–57.

Yao, L. S. and Berger, S. A. (1974). Entry flow in a curved pipe. *J. Fluid Mech.*, **67**, 177–196.

Zarins, C. K., Giddens, D. P., Bharadvaj, B. K., Sottiurai, V., Mabon, R. F., and Glagov, S. (1983). Carotid bifurcation atheroscleroses: quantitative correlation of plaque localization with flow velocity profiles and wall shear stress. *Circulation Research*, **53**, 502–514.

Zhao, S., Suciu, A., Ziegler, T., Moore, Jr, J. E., Bürki, E., Meister, J.-J., and Brunner, H. R. (1995). Synergistic effects of fluid shear stress and cyclic circumferential stretch on vascular endothelial cell morphology and cytoskeleton. *Arteriosclerosis, Thrombosis, and Vascular Biology*, **15**(10), 1781–1786.

Samenvatting

Een verstoorde wandschuifspanningsverdeling in de grote arterieën wordt gezien als een van de belangrijkste factoren in het ontstaan van aderverkalking en het falen van vaat-prothesen. Het modelleren van de wandschuifspanning, veroorzaakt door de stroming van bloed, is daarom een belangrijk onderzoeksgebied en is het onderwerp van dit proefschrift.

Bij het modelleren van wandschuifspanning is de keuze van een goed constitutief model voor bloed van wezenlijk belang. Het bepalen van dit model is niet eenvoudig: bloed is een geconcentreerde suspensie van bloed cellen in plasma en vertoond een scala van niet-Newtonse eigenschappen. Deze eigenschappen worden voornamelijk bepaald door de aggregatie en deformatie van de rode bloed cellen. Behalve de eigenschappen van bloed, spelen ook de stromingscondities in de grote arterieën een belangrijke rol in de keuze voor een constitutief model voor bloed. In de literatuur in het algemeen gemodelleerd als een Newtonse vloeistof met een viscositeit gelijk aan de viscositeit van bloed bij hoge afschuifsnelheden ($\eta = \eta_\infty$).

In het eerste gedeelte van dit proefschrift wordt een macroscopisch model voor bloed geponeerd. Een geconcentreerde KSCN oplossing, met daarin $250 ppm$ Xanthan gum, dient als een macroscopische bloed analoge vloeistof. De viscometrische eigenschappen van deze vloeistof zijn vrijwel gelijk aan die van bloed. De Xanthan gum oplossing is gemodelleerd door middel van een viskeus, afschuifsnelheidsafhankelijk, Carreau-Yasuda model. Laser Doppler anemometrie en eindige elementen berekeningen zijn gebruikt om gedetailleerde informatie te verkrijgen van het snelheidsveld in een model van de carotis vertakking onder stationaire stromingscondities en in een model van een $90°$ bocht onder instationaire stromingscondities. De resultaten voor de Xanthan gum oplossing zijn vergeleken met een Newtonse vloeistof met $\eta = \eta_\infty$.

De experimentele resultaten laten zien dat er significante verschillen aanwezig zijn in de snelheidsvelden voor de niet-Newtonse en de Newtonse vloeistof. Dit is een indicatie dat de niet-Newtonse eigenschappen van de model vloeistof niet verwaarloosd kunnen worden. De niet-Newtonse stroming werd goed voorspeld door de in-elastische niet-Newtonse berekeningen. Dit geeft aan dat het afschuifsnelheidsafhankelijke gedrag van de bloed analoge vloeistof de dominante niet-Newtonse eigenschap is en dat viskoelasticiteit verwaarloosd kan worden voor de voorspelling van het snelheidsveld.

De afschuifsnelheidsafhankelijke eigenschappen van de niet-Newtonse vloeistof kunnen worden benaderd met behulp van een Newtonse vloeistof met een viscositeit, gebaseerd of een karakteristieke afschuifsnelheid. De karakteristieke afschuifsnelheid is niet gebaseerd op de afschuifsnelheid aan de wand, maar op een gemiddelde waarde. Het Reynolds getal voor de niet-Newtonse vloeistof, gebaseerd op de karakteristieke viscositeit, is een factor drie lager dan het Reynolds getal gebaseerd op η_∞. De voorspellende waarde van het model voor de snelheidsverdeling in een suspensie met rode bloed cellen is geëvalueerd in een stroming achter een stap onder stationaire stromingscondities. De snelheidsverdeling is gemeten met ultrageluid. Het vergelijk van experimentele en numerieke data geeft aan dat ook de stroming van een rode bloed cel suspensie voorspeld kan worden met behulp van een in-elastisch Carreau-Yasuda model. De resultaten van dit experiment zijn gebruikt om een klinische methode te testen om de afschuifsnelheid aan de wand te bepalen. De klinische procedure geeft een goede voorspelling in het centrale gedeelte van het stromingskanaal, maar onderschat de afschuifsnelheid aan de wand met ongeveer 25%.

Of het Carreau-Yasuda model ook gebruikt kan worden om de wandschuifspanning te bepalen, vereist een nieuwe meettechniek. Een methode om de wandschuifspanning te bepalen is ontwikkeld voor stroming in een rechthoekig kanaal en getest voor een Newtonse en een niet-Newtonse vloeistof. De wandschuifspanning is bepaald door de deformatie van een gel laag aan de binnenkant van het stromingskanaal te bepalen. De deformatie van de gel laag is gemeten met *speckle interferometrie*, en gecombineerd met de eigenschappen van de gel laag, kan uit de gemeten deformatie de wandschuifspanning afgeleid worden. De gemeten wandschuifspanning vertoonde een uitstekende overeenkomst met de berekende wandschuifspanning, voor zowel de Newtonse als de niet-Newtonse vloeistof. Met deze methode kan de wandschuifspanning bepaald worden zonder dat de eigenschappen van de vloeistof bekend zijn.

De methode om wandschuifspanning te meten is toegepast in de stroming achter een stap met een rode bloed cel suspensie als meetvloeistof. De wandschuifspanning is bepaald onder stationaire stromingscondities. De goede overeenkomst tussen experimentele en numerieke waarden van de wandschuifspanningsverdeling geven aan dat ook de wandschuifspanning kan worden voorspeld met het Carreau-Yasuda model. Viskoelasticiteit en het deeltjes karakter van de vloeistof spelen blijkbaar geen rol in het bepalen van de wandschuifspanning.

Uit de resultaten van dit proefschrift kan worden geconcludeerd dat zowel snelheids- als wandschuifspanningsverdeling van bloed in de grote arterieën kan worden voorspeld met behulp van het viskeuze afschuifsnelheidsafhankelijke Carreau-Yasuda model. Daarmee kunnen *in-vivo* wandschuifspanningsverdelingen bepaald worden, waarmee de invloed van een belangrijke factor in het ontstaan van aderverkalking en het falen van vaat-prothesen nader bestudeerd kan worden.

Dankwoord

Graag wil allen bedanken die een bijdrage geleverd hebben aan dit proefschrift.

Mijn grote dank gaat uit naar Frans van de Vosse. Jouw steun, toewijding, en niet te vergeten, jouw inventiviteit hebben een niet te onderschatten invloed gehad. De zomerljkse retraite in jouw huis was altijd zeer vruchtbaar.

De mannen op de achtergrond: Jan en Rob, bedankt voor de stimulerende gesprekken tijdens de initiële fase van dit onderzoek, en voor het lezen en corrigeren van het manuscript.

Voor de technische ondersteuning, zowel op gebied van software als hardware wil ik eenieder bedanken die mij geholpen heeft. Met name Theo van Duppen heeft veel klusjes voor mij geklaard.

Niet te vergeten zijn de studenten. Jongens en meiden, de samenwerking met jullie was altijd leuk, en soms hebben jullie een niet geringe bijdrage geleverd: Erwan Allanic, Henri Brouwers, Tjits van Campen, Geert Diederen, Ad Goijaerts, Arjen Heres, Patric Machiels, Cynthia Mors, Frank Schepens, Angela Smits, Joris ten Tijen, Kees van Weert, Pieter Wortel en Jasper Zuidervaart, bedankt.

Peter wil ik graag bedanken voor zijn kennis en steun bij het uitvoeren van de ultrasound metingen.

En natuurlijk mijn kamergenoten Marcel en Sander: vanaf het kraken van de 'Watchtower' tot en met de gezamelijke worstelingen onze boekjes af te maken, hebben we veel steun aan elkaar gehad. Niet dan?

En tenslotte, Petra. Bedankt voor het bouwen van ons huis, ik kom nu eindelijk echt bij jou wonen.

Curriculum Vitae

- •: 7-3-1967: Geboren te Herkenbosch

- •: 1978-1985: Gymnasium β, B. C. Schöndeln, Roermond

- •: 1985-1993: Werktuigbouwkunde aan de TU Eindhoven

- •: 1989-1990: Docent Materiaalkunde aan de Univeristy of Zambia

- •: 1992: Stage aan de Ohio State Unversity, USA

- •: 1993-1995: Computational Mechanics, SAI, TU Eindhoven

- •: 1995-1998: Promotie onderzoek aan de TU Eindhoven

Stellingen

behorend bij het proefschrift

Modeling of wall shear stress in large arteries

1. De veronderstelling dat de afschuifsnelheid in de grote slagaderen zo hoog is dat het niet-Newtonse karakter van bloed verwaarloosd kan worden is onjuist.

   - dit proefschrift

2. De invloed van de niet-Newtonse eigenschappen van bloed op de wandschuifspanning kan worden beschreven met een puur viskeus constitutief model voor bloed.

   - dit proefschrift

3. Het afschuifsnelheidsafhankelijke gedrag van bloed kan gelinearizeerd worden met behulp van een karakteristieke viscositeit. Het Reynolds getal, gebaseerd op deze karakteristieke viskositeit, is lager dan algemeen wordt aangenomen. Daardoor zal de opsporing van stenoses in de carotis vertakking aan de hand van gemeten snelheidsprofielen nog moeilijker worden.

   - dit proefschrift
   - D.E.M. Palmen, F.J.H. Gijsen, F.N. van de Vosse, and J.D. Janssen (1997): 'Diagnosing minor stenoses in carotid artery bifurcation models using the disturbed velocity field.' *Journal of Vascular Investigation*, 3(1), 26–41.

4. Een constitutief model dat alleen de afschuifsnelheidsafhankelijke viscositeit modelleert is in het algemeen ontoereikend voor een niet-Newtonse vloeistof. Dat deze modellen toereikend zijn voor bloed in de grote slagaderen komt door de door convectie gedomineerde stroming.

   - dit proefschrift

5. Voordat complexe meetapparatuur wordt aangeschaft is een grondige kennis van het meetprincipe vereist. Het vooraf ervaring opdoen met de relevante meetprincipes voorkomt teleurstellingen.

6. Aandacht voor productontwikkeling in biomechanisch wetenschappelijk onderzoek zal financiering en onderzoeksevaluatie vergemakkelijken en hoeft het karakter van het onderzoek niet negatief te beïnvloeden.

7. De mate waarin gerefereerd wordt naar proefschriften kan geen rechtvaardiging zijn voor de hoeveelheid tijd die wordt besteed aan het schrijven daarvan.

8. In de biologische evolutie staat het model van Lamarck, dat vooruitgang impliceert, lijnrecht tegenover het - correcte - model van Darwin. In de culturele evolutie zou vooruitgang kunnen worden bereikt door kennisoverdracht van de ene generatie op de andere. De massale vernietiging van cultuur en milieu lijkt erop te wijzen dat Darwin's model ook geldt voor de culturele evolutie.

- S.J. Gould (1996): 'The mismeasure of man'.

9. Illegalisering van cafeïne zou van veel universiteitsmedewerkers criminelen maken.

10. Kok is ook maar een betaalde baan.

11. Stellingen kenmerken zich vaker door gebrek aan nuances dan door de kracht van het gestelde.

12. Het belang van gezamenlijk eten en drinken kan nauwelijks overschat worden.

Frank Gijsen,
Eindhoven, 7 mei, 1998